WIND EXCITED VIBRATION OF SQUARE SECTION BEAM AND SUSPENDED CABLE

Vivekananda Mukhopadhyay

Massachusetts Institute of Technology

Prepared for:

Air Force Office of Scientific Research

May 1972

AFOSR TR

ASRL TR 159-3

WIND EXCITED VIBRATION OF SQUARE SECTION BEAM AND SUSPENDED CABLE

Vivekananda Mukhopadhyay

Aeroelastic and Structures Research Laboratory
Department of Aeronautics and Astronautics
Massachusetts Institute of Technology
Cambridge, Massachusetts 02139

May 1972

Prepared for
AIR FORCE OFFICE OF SCIENTIFIC RESEARCH
UNITED STATES AIR FORCE

under

CONTRACT NO. F44620-69-C-0091

Qualified requestors may obtain additional copies from the Defense Documentation Center, all others should apply to the National Technical Information Service.

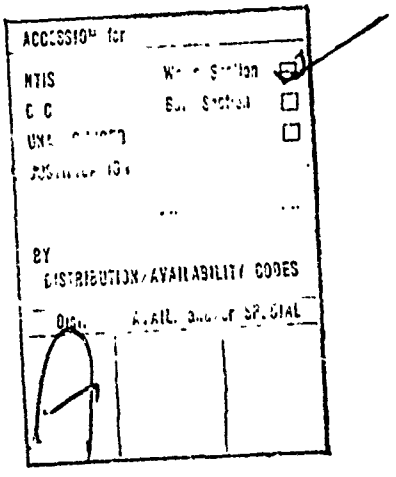

UNCLASSIFIED

Security Classification

DOCUMENT CONTROL DATA - R & D

(Security classification of title, body of abstract and indexing annotation must be entered when the overall report is classified)

1. ORIGINATING ACTIVITY (Corporate author) MASSACHUSETTS INSTITUTE OF TECHNOLOGY AEROELASTIC & STRUCTURES RESEARCH LABORATORY CAMBRIDGE, MASSACHUSETTS 02139	2a. REPORT SECURITY CLASSIFICATION UNCLASSIFIED 2b. GROUP

3. REPORT TITLE

WIND EXCITED VIBRATION OF SQUARE SECTION BEAM AND SUSPENDED CABLE

4. DESCRIPTIVE NOTES (Type of report and inclusive dates)

Scientific Interim

5. AUTHOR(S) (First name, middle initial, last name)

VIVEKANANDA MUKHOPADHYAY

6. REPORT DATE May 1972	7a. TOTAL NO. OF PAGES 128	7b. NO. OF REFS 39
8a. CONTRACT OR GRANT NO F44620-69-C-0091 b. PROJECT NO. 9782-01 c. 61102F d. 681307	9a. ORIGINATOR'S REPORT NUMBER(S) ASRL TR 159-3 9b. OTHER REPORT NO(S) (Any other numbers that may be assigned this report) AFOSR - TR - 72 - 2008	

10. DISTRIBUTION STATEMENT

Approved for public release; distribution unlimited.

11. SUPPLEMENTARY NOTES TECH, OTHER	12. SPONSORING MILITARY ACTIVITY AF Office of Scientific Research (NAM) 1400 Wilson Boulevard Arlington, Virginia 22209

13. ABSTRACT

The self-excited oscillation of a square section vertical cantilever beam and a square section sagging suspended cable in a uniform wind stream was investigated theoretically and experimentally. Experimental quasi-static representation of aerodynamic forces was used to determine the responses theoretically. The excitation is due to negative damping type aerodynamic forces and the amplitude is limited as the forces become nonlinear. The governing equations were reduced to ordinary differential equations by Galerkin's method and steady state solutions were determined by harmonic balance technique. For the cantilever beam, the solutions agree qualitatively with the experimental results but failed to predict some peculiar amplitude drop-off behavior observed in the experiment. In these cases the response was found to be very sensitive to small changes in initial angle of attack. For the suspended cable, both structural nonlinearity due to tension and aerodynamic nonlinearity had to be considered. The agreement between theory and experiment was good for the frequency response but only qualitative for the amplitude response.

DD FORM 1 NOV 1473

IA

UNCLASSIFIED

Security Classification

14 KEY WORDS	LINK A		LINK B		LINK C	
	ROLE	WT	ROLE	WT	ROLE	WT
WIND EXCITED VIBRATION						
VIBRATION OF SQUARE BEAM						
VIBRATION OF SQUARE SECTION SUSPENDED CABLE						
CABLE VIBRATION						
SELF-VIBRATION OF SUSPENDED CABLE						

Ib

AFOSR TR

ASRL TR 159-3

WIND EXCITED VIBRATION OF SQUARE SECTION BEAM AND SUSPENDED CABLE

Vivekananda Mukhopadhyay

AEROELASTIC AND STRUCTURES RESEARCH LABORATORY
DEPARTMENT OF AERONAUTICS AND ASTRONAUTICS
MASSACHUSETTS INSTITUTE OF TECHNOLOGY
CAMBRIDGE, MASSACHUSETTS 02139

May 1972

Prepared for

AIR FORCE OFFICE OF SCIENTIFIC RESEARCH
UNITED STATES AIR FORCE

Under

CONTRACT NO. F44620-69-C-0091

ACKNOWLEDGEMENTS

The author wishes to express his sincere gratitude to Professor John Dugundji for his invaluable advice and guidance throughout this study and for continuous help in the experiment. Helpful criticisms and suggestions provided by Professors M. Finston , P. Tong , T. H. H. Pian , E. A. Witmer and Mr. F. H. Durgin are also gratefully acknowledged. Thanks are also due to Messrs. A. R. Shaw , F. Merlis for their help in the experiment.

This work was supported by the U. S. Air Force Office of Scientific Research under the Contract No. F44620-69-C-0091 administered by Dr. Jacob Pomerantz.

ABSTRACT

The self-excited oscillation of a square section vertical cantilever beam and a square section sagging suspended cable in a uniform wind stream was investigated theoretically and experimentally.

Experimental quasi-static representation of aerodynamic forces was used to determine the responses theoretically. The excitation is due to negative damping type aerodynamic forces and the amplitude is limited as the forces become nonlinear. The governing equations were reduced to ordinary differential equations by Galerkin's method and steady state solutions were determined by harmonic balance technique.

For the cantilever beam, the solutions agreed qualitatively with the experimental results but failed to predict some peculiar amplitude drop-off behavior observed in the experiment. In these cases the response was found to be very sensitive to small changes in initial angle of attack.

For the suspended cable, both structural nonlinearity due to tension and aerodynamic nonlinearity had to be considered. The agreement between theory and experiment was good for the frequency response but only qualitative for the amplitude response.

CONTENTS

CONTENTS CONCLUDED

LIST OF SYMBOLS

CANTILEVER BEAM

a	Dimensionless amplitude W_T/b
$\bar{a}$	Defined in Eq. 3.11
$\bar{a}_1$	Defined in Eq. 3.46
a_1, a_2, b_1, b_2	Coefficients of assumed solution (Eq. 3.33)
a_{11}, a_{12}	Defined in Eq. 3.41
a_{21}, a_{22}	
A_n, $A_{m\&n}$	Constants defined in Appendix A
b	Side of square section
c	Structural damping coefficient
C_L, C_D	Lift and drag coefficients
C_N, C_C	Defined in Eq. 2.4
C_Y, C_Z	Force coefficients along Y and Z directions
D	Drag force
D_1	Defined in Appendix A
EI	Bending rigidity
$f_1(\xi)$	Assumed first bending mode shape
f_{s1}, f_{c1}, f_{s2}, f_{c2}	Harmonic balance coefficient equations defined in Eq. 3.34
F_Y, F_Z	Aerodynamic forces in Y and Z directions
$F(a)$	Defined in Eq. 3.16
g_1	Defined in Eq. 3.6
g_{11}, g_{12}	Defined in Eq. 3.25
g_{21}, g_{22}	

G_n	Defined in Eq. 3.5
$\tilde{G}_n$	Defined in Eq. 3.9
ℓ	Length of Cantilever beam
L	Lift force
m	Mass per unit length
N_{mn}	Coefficients of binomial expansion (Eq. 3.23)
P	Defined in Eq. 3.27
P_n, Q_n	Coefficients of polynomial fit of C_N, C_C (Eq. 5.25)
$\tilde{P}_n$, $\tilde{Q}_n$	Defined in Eq. 2.12
q_1, q_2	Dimensionless generalized coordinate (Eq. 3.19)
t	time
u	Reduced velocity (Eq. 3.3)
u_c	Critical velocity
$\bar{u}$	Defined in Eq. 3.11
U	Free stream velocity
U_{REL}	Relative velocity (Fig. 2c)
V, W	Displacements in Y and Z directions
$\dot{V}$, $\dot{W}$	Velocities in Y and Z directions
W_T	Tip amplitude of the beam
X, Y, Z	Coordinate system
Z_n, Y_n	Defined in Eq. 2.14
$\tilde{Z}_{mn}$, $\tilde{Y}_{mn}$	Defined in Eq. 3.25
α	Static angle of attack
α_o	Initial angle of attack
β	Induced angle of attack

θ	Defined in Eq. 3.32
ϕ	Integration constant (Eq. 3.7)
γ	Inclination of plane of motion w.r.t. Z direction (Eq. 3.37, Fig. 12a,b)
$\tilde{\gamma}$	Tan γ (Eq. 3.47)
ζ_1	Critical damping ratio
ζ_{EQ}	Equivalent damping ratio (Eq. 4.2)
ρ	Air density
$\tilde{\rho}$	Mass ratio (Eq. 3.3)
σ	Defined in Eq. 3.28
τ	Dimensionless time ($= \omega_1 t$)
ω_1	First mode natural frequency
ξ	Dimensionless length x/ℓ
$\xi(\tau)$ $\eta(\tau)$	Defined in Eq. 3.14
$(\dot{})$	$\partial(\ )/\partial t$
$(\overset{\circ}{})$	$d(\ )/d\tau$

SUSPENDED CABLE

a_o, a_1, b_1, a_2, b_2	Coefficients of assumed solution (Eq. 5.23)
$\tilde{a}_o, \tilde{a}_1, \tilde{b}_1, \tilde{a}_2, \tilde{b}_2$	
A_{mn}, A'_{mn}	Constants defined in Appendix D
ΛE	Extensional rigidity
b	Side of square section
B_{mn}	Constants defined in Appendix D
$c_1, \tilde{c}_1, c_2, \tilde{c}_2$	Damping coefficients (Eq. 5.16)

C_N, C_C	Defined in Eq. 2.4
d	Mid-span sag
D_1, D_2	Constants defined in Appendix D
D_o	Static drag
e	Defined in Eq. 5.10
EI	Bending rigidity
$f_{oo}(\xi)$	Initial static position W_{oo}/d
$f_o(\xi)$, $\tilde{f}_o(\xi)$	Static deflection positions
$f_1(\xi)$, $\tilde{f}_1(\xi)$	Assumed mode shapes (Eq. 5.14)
$f_2(\xi)$, $\tilde{f}_2(\xi)$	
F_Y, F_Z	Aerodynamic forces in Y and Z directions
g	Acceleration due to gravity
$g_1, \tilde{g}_1, g_2, \tilde{g}_2$	Defined in Eq. 5.17
ℓ	Span
m	Mass per unit length
P_n, Q_n	Coefficients of Polynominal fit of C_N, C_C (Eq.5.14)
$q_o, \tilde{q}_o$	Defined in Appendix D
$q_1, \dot{q}_1, q_2, \tilde{q}_2$	Dimensionless generalized coordinate (Eq. 5.14)
r_1, r_2	Defined in Eq. 5.15
t	Time
T_{oo}	Initial tension due to self weight
T_o	Static tension
T(t)	Dynamic tension (Eq. 5.4)
T_t	Total tension (Eq. 5.4)
$\bar{T}$	Dimensionless T(t) (Eq. 5.15)

u	Dimensionless velocity (Eq. 5.15)
u_c	Critical velocity
U	Free stream velocity
V_o, W_o	Static deflection position in Y and Z directions
V, W	Dynamic displacement in Y and Z directions
V_t, W_t	Total deflection position in Y and Z directions
W_{oo}	Initial static position
W_M	Mid-span amplitude (Fig. 24a)
X, Y, Z	Coordinate system
α_1, α_2	Constants defined in Eq. 5.15
β	Induced angle of attack
β_r	Constant defined in Appendix D
θ	Cable inclination (Fig. 20)
$\varepsilon_o, \varepsilon_{oo}$	Defined in Eq. 5.10
$\zeta_1, \tilde{\zeta}_1, \zeta_2, \tilde{\zeta}_2$	Damping ratios (Eq. 5.16)
ρ	Air density
$\tilde{\rho}$	Defined in Eq. 5.15
τ	Dimensionless time ($=\omega_R t$)
ω	Nondimensional frequency w.r.t. ω_{o1}
ω_R	Reference frequency
ω_F	Flutter frequency
ω_{o1}	First mode natural frequency at U=0 (Eq. 5.22)
ω_1, ω_2	First and second mode oscillation frequency
$\Omega_1, \tilde{\Omega}_1$	Defined in Eq. 5.17

Λ	Defined in Eq. 5.17
ξ	Dimensionless length x/ℓ
$(\dot{})$	$\partial(\ )/\partial t$
$(\overset{\circ}{})$	$d(\ )/d\tau$

SECTION 1

INTRODUCTION

Among the study of wind effects on non-streamlined structures (Refs. 1, 2, 3, 4), the self-excited oscillation of square section, cylinder-like bodies has been a subject of research for many years. The two basic exciting forces which act on the body are due to

(a) The Karman-Vortex shed alternately from either side which exert periodic forces on the body

(b) The aerodynamic lift and drag forces due to asymmetric flow, including the effect of wake, flow separation, reattachment, etc.

The vortex shedding is responsible for high frequency, low amplitude oscillations often called Aeolian vibrations and has been observed in bluff bodies with or without sharp edges such as stretched cables, tall towers such as rockets in launching pad, smoke stacks, etc. The oscillations usually occur when the natural frequency of the flexible body is close to the vortex shedding frequency (Ref. 5). Since the Strouhal number is usually known (Ref. 6, 7, 8), this kind of resonance vibration takes place at a known wind velocity and can easily be avoided.

The self-excitation due to the aerodynamic lift and drag forces usually occurs in bluff bodies with sharp edges and is commonly known as galloping. It has been observed in a space shuttle on a launching pad (Ref. 9), tall buildings (Ref. 2) and overhead power transmission lines during a sleet storm (Refs. 10-13). This kind of self-excitation can take place over a wide range of wind velocity independent of the natural frequency of the body and is the main subject of study in the present report, using a square section vertical cantilever beam and a suspended sagging

cable in a uniform wind stream free from turbulence.

The aerodynamic properties of bluff bodies exhibiting galloping oscillation are such that at a certain initial angle of attack the aerodynamic lift force induced by a small transverse motion of the body, acts in the direction of the motion. This results in a negative damping type exciting force. The explanation was first given by Den Hartog (Refs. 14, 15). Parkinson and associates (Refs. 16-21) have analyzed the one degree of freedom transverse oscillation of square section prism suspended by linear spring, using quasi-static representation of aerodynamic forces. The resulting nonlinear equation is solved by Krylov Bogoliubov's asymptotic method. A good theory to experiment agreement is observed except when the structural damping is very small. Novak applied the quasi-static theory using energy balance to a two-dimensional body in form of a rigid square section prism pivoted at the base (Refs. 22, 23) and obtained qualitative agreement with the experiment and did not get the hysteresis in the experiment originally observed by Parkinson. Working with rectangular prismatic pivoted cantilever, Novak again obtained qualitative agreement with the experiment but observed some interesting response characteristics (Refs. 24, 25). In all the above studies the specimen was constrained to move only in transverse direction and were initially kept at zero angle of attack.

In the present report, a square section cantilever beam is considered which is free to move in any direction without twisting. Quasi-static representation of aerodynamic forces is used to determine the response at various initial angles of attack, theoretically. Experiment is conducted to examine the applicability of such a theory for large 3D displacement. The system is governed by a pair of nonlinear partial differential equations. The nonlinearity arises from nonlinear aerodynamic forces. They are reduced to ordinary differential equations by Galerkin's method and solved by harmonic balance technique to determine

steady-state limit cycle amplitude. Qualitative agreement with experiment is observed at low amplitudes, but as the wind velocity is increased peculiar response is observed in certain cases which cannot be explained by quasi-static theory. The static forces are found to be quite sensitive to slight imperfections, sharpness of the edges and Reynold's number. It is believed that the forces are even more sensitive to these factors when the body is in motion and the averaged static force measurements are not sufficient to explain them. The quasi-static representation is explained in Section 2. Sections 3 and 4 contain the cantilever analysis and experimental results.

The galloping of power transmission cables have been studied by Hogg (Refs. 11-12), Richards (Ref. 13), and many other authors. Richardson and Martuccelli (Refs. 26-29) worked out two-dimensional, three degrees of freedom dynamics of a D section with linear spring and piecewise linear quasi-static aerodynamics. They also measured aerodynamic properties of two-dimensional sections of various shapes. None of these studies consider the aerodynamic excitation of the power transmission line as a three-dimensional catenary in writing the elastic part of the equations In this case the tension in the cable along with the non-linear aerodynamic forces are responsible for limiting the amplitude. Thus structural nonlinearity arising from the tension terms is also important in this case.

In the present report, galloping of a sagging cable of square cross section has been obtained experimentally in a wind tunnel. The motion is governed by two non-linear partial differential equations which are reduced to non-linear ordinary differential equations in time using Galerkin's approximation and are solved by harmonic balance method using only two equations. Good agreement is obtained in the frequency of oscillations but the amplitudes are in qualitative agreement only for two particular sags. From the experimental results it is observed that the

aerodynamic lift forces do not reach the values given by the quasi-static theory due to the lack of spanwise correlation. The cable analysis and experiment are described in Sections 5 and 6.

SECTION 2

AERODYNAMIC FORCES ON SQUARE SECTION BODY

2.1 Introduction

In this section the various aspects of flow aroung a fixed or movable square section body and the nature of the resulting forces has been discussed. Attention is restricted to uniform subsonic flow. The flow around bluff bodies with sharp edges have some different characteristics in comparison to the flow around a cylinders. These are pointed out in Section 2.2. The quasi-static representation of aerodynamic forces on a translating square section body is explained in Section 2.3 and is used in subsequent sections.

2.2 Aerodynamic Forces

Many experimental investigations of flow around a circular section body have been done in the past but available experimental results for a square section body are relatively few even though the flow around bluff bodies with sharp edges have some interesting characteristics. The basic differences between the two flow fields are the following:

(a) In a circular body the flow separation can occur at different locations of the body depending on the Reynolds number and the flow condition of the wake. In square body, separation can occur only at sharp edges.

(b) Because of fixed separation point, there is a stronger spanwise correlation of forces on a square cylinder than on a round one (Ref. 33) Thus, on square section cylinders, the overall aerodynamic forces are stronger.

(c) When the flow is at an angle of attack due to the asymmetry of shear layer separation from the edges and presence of the afterbody in the separated flow, the lift forces on the square section are considerably greater than that for the circular cross section (Ref. 33).

(d) Reattachment of separated flow is possible at a certain angle of attack and separation point can shift from front edge 1 to the rear edge 2 at higher angles of attack as shown here in Fig. 3 (Ref. 19). Due to considerable change in wake width, the drag varies considerably with angle of attack reaching minimum value at the angle of attack when reattachment first occurs (Fig. 3c). The lift forces reach a maxima at this angle.

The effect of the Reynolds number on a square section is similar to that of circular section except for the drop in drag at critical Reynolds number 4×10^5 since the separation point is fixed. However, when the edges are slightly rounded, similar drop in drag at Re 6×10^6 (for r/b = 0.176) has been observed by Delany (Ref. 34). The Strouhal number is 0.13 at Re = 3000 and changes very slightly with angle of attack and Reynolds number (Refs. 6, 35).

When the bluff body is flexible and can oscillate transversely, the spanwise correlation of forces increases even with a circular cylinder. The shedded vortex can excite the body if the shedding frequency is near its natural frequency. The oscillating body in turn exerts some control on the shedding phenomena and the shedding frequency locks on to the oscillation frequency over a short range of velocity instead of following the Strouhal number relationship (Refs. 5, 20, 36). Extensive study of wake

behind an oscillating circular cylinder has been done recently by Toebes (Ref. 37) and Griffin (Ref. 38). The vortex shedding frequency of the present specimen is quite high compared to its natural frequency and thus does not affect the response appreciably.

2.3 Quasi-Static Representation

Let us consider a square section body translating in a uniform fluid stream with a velocity $\dot{W}$ along the Z direction as shown in Fig. 2c. The induced angle of attack β due to the velocity is given by $\tan\beta = \dot{W}/U$. In quasi-static representation of aerodynamic forces it is assumed that the forces are the same as if the body were at rest in a uniform stream of velocity U_{REL} at an angle of attack β. Total forces normal to and along the U_{REL} are

$$L = \tfrac{1}{2}\rho U_{REL}^2\, b\, C_L(\beta) \qquad \text{lbs/ft}$$

$$D = \tfrac{1}{2}\rho U_{REL}^2\, b\, C_D(\beta) \qquad " \qquad (2.1)$$

In actual flow the development of forces due to an induced angle of attack may not be instantaneous. It may differ both in magnitude and phase. In quasi-static representation these effects are neglected. Since no theory exists to predict the unsteady aerodynamic forces on a bluff-body with turbulent wake, the unsteady forces can only be determined by carefully conducted dynamic tests. For square section body, no such results seem available.

Resolving the forces along Z and Y direction which are normal to and along the free stream direction and noting that $U_{REL} = U\,\mathrm{Sec}\beta$

$$F_Z = \tfrac{1}{2}\rho U^2 b\, \mathrm{Sec}^2\beta \left[-C_L \mathrm{Cos}\beta - C_D \mathrm{Sin}\beta \right]$$

$$F_Y = \tfrac{1}{2}\rho U^2 b\, \mathrm{Sec}^2\beta \left[C_D \mathrm{Cos}\beta - C_L \mathrm{Sin}\beta \right] \qquad (2.2)$$

F_Z is taken positive in the direction W. To use F_Z, F_Y in equations of motion it is convenient to express them as algebraic functions of $\dot{W}/U$, i.e., as algebraic functions of tanβ. One possible way is to define new force coefficients acting in the direction F_Z and F_Y such that

$$F_Z = \tfrac{1}{2}\rho U^2 b\, C_N(\beta)$$

$$F_Y = \tfrac{1}{2}\rho U^2 b\, C_C(\beta) \qquad (2.3)$$

where C_N, C_C are defined as

$$C_N(\beta) = \sec\beta \left[-C_L(\beta) - C_D \tan\beta \right]$$

$$C_C(\beta) = \sec\beta \left[C_D(\beta) - C_L \tan\beta \right] \qquad (2.4)$$

Considering the zero reference angle of attack to be the position when one of the faces of the square is normal to the free stream direction, C_N, C_C with respect to this origin can now be determined as following. Lift and drag forces on a static body at various angles of attack α (Fig. 2b) can be measured and converted to C_L, C_D by dividing by $\frac{1}{2}\rho U^2 b$. C_N, C_C are then computed using Eq. 2.4 . Here β is taken equal to the static angle of attack α at which the forces were measured. C_N, C_C are now plotted against tanβ and fitted with a polynomial in the form

$$C_N = \sum_{n=0}^{N} P_n (\tan\beta)^n$$

$$C_C = \sum_{n=0}^{N} Q_n (\tan\beta)^n \qquad (2.5)$$

In the equations of motion C_N, C_C are used as force coefficients and tanβ is replaced by $\dot{W}/U$.

Now let the body be initially at an angle of attack α_o with respect to the free stream and translate without rotation with velocity components $\dot{V}$ and $\dot{W}$ along Y and Z directions as shown in Fig. 2d. Expressing F_z, F_Y in terms of induced angle of attack β in the similar manner one obtains

$$F_z = \tfrac{1}{2}\rho U_{REL}^2 b\,[-C_L(\beta-\alpha_o)\cos\beta - C_D(\beta-\alpha_o)\sin\beta]$$

$$F_Y = \tfrac{1}{2}\rho U_{REL}^2 b\,[C_D(\beta-\alpha_o)\cos\beta - C_L(\beta-\alpha_o)\sin\beta] \qquad (2.6)$$

where

α_o = Fixed angle (+Ve in the sense shown in Fig. 2d)

$\tan\beta = \dot{W}/(U-\dot{V})$ (Induced angle of attack)

$U_{REL} = (U-\dot{V})\sec\beta$ $\qquad (\dot{}) = \frac{\partial(\ )}{\partial t}$

Here $C_L(\beta-\alpha_o)$ represents static C_L measured at an angle of attack $(\beta-\alpha_o)$ where zero angle of attack is the position when one of the faces of the square cross section is normal to the free stream direction. Introducing U_{REL}

$$F_z = \tfrac{1}{2}\rho(U-\dot{V})^2 b\,[-C_L(\beta-\alpha_o) - C_D(\beta-\alpha_o)\tan\beta]\sec\beta$$

$$F_Y = \tfrac{1}{2}\rho(U-\dot{V})^2 b\,[C_D(\beta-\alpha_o) - C_L(\beta-\alpha_o)\tan\beta]\sec\beta \qquad (2.7)$$

Now to express the forces in terms of $\dot{W}$ and $\dot{V}$ in a convenient form, it has to be written in a polynomial form in $\tan\beta$. This can be done in two ways:

a) One can plot $[-C_L(\beta-\alpha_o) - C_D(\beta-\alpha_o)\tan\beta]\sec\beta$, and $[C_D(\beta-\alpha_o) - C_L(\beta-\alpha_o)\tan\beta]\sec\beta$, versus $\tan\beta$ at a fixed α_o and fit it with polynomials of $\tan\beta$ to give:

$$F_z = \tfrac{1}{2}\rho U^2 b\left(1-\frac{\dot{V}}{U}\right)^2 \sum_{n=0}^{N} Z_n(\alpha_o)\tan^n\beta$$

$$F_Y = \tfrac{1}{2}\rho U^2 b\left(1-\frac{\dot{V}}{U}\right)^2 \sum_{n=0}^{N} Y_n(\alpha_o)\tan^n\beta \qquad (2.8)$$

The highest order power N can be chosen for a best reasonable fit but must be kept minimum to avoid unnecessary complexity. This procedure is not very convenient since at every α_o, one has to carry out the curve fitting numerically.

b) To avoid this disadvantage, it is desirable to express Eq.2.7 in terms of C_N and C_C whose polynominal fit is already known from Eq. 2.5. To do this one may write

$$\tan\beta = \left(\tan(\beta-\alpha_o)+\tan\alpha_o\right)/\left(1-\tan(\beta-\alpha_o)\tan\alpha_o\right)$$
$$\sec\beta = \left(\sec(\beta-\alpha_o)\sec\alpha_o\right)/\left(1-\tan(\beta-\alpha_o)\tan\alpha_o\right) \qquad (2.9)$$

in Eq. 2.7 and combine the C_L and C_C terms using the definition (2.4) of C_N and C_C to get

$$F_Z = \tfrac{1}{2}\rho U^2 b\left(1-\frac{\dot{V}}{U}\right)^2\left[C_N(\beta-\alpha_o)-C_C(\beta-\alpha_o)\tan\alpha_o\right]\sec\alpha_o/\left(1-\tan(\beta-\alpha_o)\tan\alpha_o\right)^2$$

$$F_Y = \tfrac{1}{2}\rho U^2 b\left(1-\frac{\dot{V}}{U}\right)^2\left[C_C(\beta-\alpha_o)+C_N(\beta-\alpha_o)\tan\alpha_o\right]\sec\alpha_o/\left(1-\tan(\beta-\alpha_o)\tan\alpha_o\right)^2$$

(2.10)

This may be written in the final form as

$$F_Z = \tfrac{1}{2}\rho U^2 b\left(1-\frac{\dot{V}}{U}\right)^2\left[C_N(\beta-\alpha_o)-C_C(\beta-\alpha_o)\tan\alpha_o\right](1+\tan\beta\tan\alpha_o)^2\cos^3\alpha_o$$

$$F_Y = \tfrac{1}{2}\rho U^2 b\left(1-\frac{\dot{V}}{U}\right)^2\left[C_C(\beta-\alpha_o)+C_N(\beta-\alpha_o)\tan\alpha_o\right](1+\tan\beta\tan\alpha_o)^2\cos^3\alpha_o$$

(2.11)

Now introducing Eq. 2.5 in above, one obtains

$$F_z = \tfrac{1}{2}\rho U^2 b\left(1-\frac{\dot V}{U}\right)^2 \cos^3\alpha_o \sum_{n=0}^{N} \tilde P_n \frac{(\tan\beta - \tan\alpha_o)^n}{(1+\tan\beta\tan\alpha_o)^{n-2}}$$

$$F_Y = \tfrac{1}{2}\rho U^2 b\left(1-\frac{\dot V}{U}\right)^2 \cos^3\alpha_o \sum_{n=0}^{N} \tilde Q_n \frac{(\tan\beta - \tan\alpha_o)^n}{(1+\tan\beta\tan\alpha_o)^{n-2}} \qquad (2.12)$$

where $\tilde P_n = P_n - Q_n \tan\alpha_o$

$\tilde Q_n = Q_n + P_n \tan\alpha_o$

Eq. 2.12 can be expressed in the form (2.8) as follows. First, one may write

$$\frac{1}{(1+\tan\beta\tan\alpha_o)^{n-2}} \approx 1-(n-2)\tan\beta\tan\alpha_o + \frac{(n-2)(n-1)}{2}(\tan\beta\tan\alpha_o)^2 - \cdots. \qquad (2.13)$$

For example, for a square section the estimated maximum $|\tan\beta\tan\alpha_o| \lesssim 0.05$. Thus if $N = 6$, just one term in the above approximation needs to be retained with only 3% error. Now using Eq. 2.13 in Eq. 2.12, expanding the numerator terms fully and collecting the coefficients of $\tan\beta$ one obtains

$$F_z = \tfrac{1}{2}\rho U^2 b\left(1-\frac{\dot V}{U}\right)^2 \sum_{n=0}^{N_1} Z_n(\alpha_o)\tan^n\beta$$

$$F_Y = \tfrac{1}{2}\rho U^2 b\left(1-\frac{\dot V}{U}\right)^2 \sum_{n=0}^{N_1} Y_n(\alpha_o)\tan^n\beta \qquad (2.14)$$

Here Z_n, Y_n are known functions of α_o, P_n, Q_n and can be computed for any α_o. $Z_n(\alpha_o)$, $Y_n(\alpha_o)$ for $N = 4$ are given in Appendix C. In the equations of motion $\tan\beta$ is replaced by $\dot W/(U-\dot V)$

SECTION 3

CANTILEVER BEAM

3.1 Introduction

In this section the quasi-static representation of the aerodynamic forces described in Section 2 will be used to formulate the motion of a square-cross section cantilever beam when placed in an uniform wind stream. Such a simple structure is chosen so that the emphasis can be given to the quasi-static representation of the aerodynamic forces and its applicability can be examined thoroughly. The geometric non-linearity due to large deflection of a cantilever beam is very small and the force-deflection relation is linear up to tip deflections of 25% of the span. Thus only the aerodynamic nonlinearity needs to be considered here.

The beam has the same bending rigidity in all directions and is thus free to translate in a two degrees of freedom space. It has high torsional stiffness and does not twist under the existing forces.

Even though the present model is free to move in any direction, the motion is predominantly normal to the wind stream direction when the square section beam is initially at zero degree angle of attack. In Section 3.2 this one degree of freedom motion is considered and solved by harmonic balance method for initial introduction to the problem. The solutions are compared with experimental results in Section 4. This is the only case investigated by most authors. Moreover, their models are constrained to move in lateral direction only. In Section 3.3 the general case of two degrees of freedom motion is considered and solved by harmonic balance method. The essential features are pointed out with a simple example and the justification of using one degree of freedom motion at zero initial angle of attack is discussed. The solutions are

compared with experimental results in Section 4.

3.2 One Degree of Freedom Motion

Let us first consider the case when the beam is initially at zero angle of attack with one of the sides of the square section facing the wind stream and moves normal to the wind direction as shown in Fig. 2c. The simple equation of motion of the uniform beam is given by the well known expression

$$m\frac{\partial^2 W}{\partial t^2} + c\frac{\partial W}{\partial t} + EI\frac{\partial^4 W}{\partial x^4} = \frac{1}{2}\rho U^2 b\, C_N\left(\frac{\partial W}{\partial t}/U\right) \qquad (3.1)$$

Here w(x,t) is the displacement normal to the wind stream, U is the free stream velocity and c is small structural damping coefficient. It is convenient to express this in the form of viscous damping since the vibration frequency is close to the natural frequency. In general, at low subsonic speed, the aerodynamic forces are small compared to the inertia and elastic forces. m is the mass per unit length, ρ is the density of air which is considered incompressible, b is the dimension of the side of the square, and the right-hand side represents aerodynamic forces induced by the motion. Applying Galerkin's approximation to reduce Eq. 3.1 into an ordinary differential equation in time t using only one mode

$$W(\xi,t) = b f_1(\xi) q_{b1}(t) \qquad \xi = x/\ell \qquad (3.2)$$

where $f_1(\xi)$ is the first bending mode shape of a freely vibrating cantilever beam as given in Appendix A, the Eq. 3.1 becomes after nondimensionalization

$$\frac{d^2 q_{b1}}{d\tau^2} + 2\zeta_1\frac{dq_{b1}}{d\tau} + q_{b1} = \frac{1}{2}\tilde{\rho}u^2\frac{1}{A_1}\int_0^1 C_N\left(\frac{f_1(\xi)}{u}\frac{dq_{b1}}{d\tau}\right) f_1(\xi)\, d\xi \qquad (3.3)$$

where

$$\omega_1 t = \tau$$

$$\omega_1^2 = \frac{D_1}{A_1}\frac{EI}{ml^4} \quad \text{(First mode natural frequency)}$$

$$\zeta_1 = c/2\omega_1 m \quad \text{(Damping ratio)}$$

$$\tilde{\rho} = \rho b^2/m \quad \text{(Mass ratio)}$$

$$u = U/\omega_1 b \quad \text{(Reduced velocity)}$$

and A_1 and D_1 are integrals of the mode shape and are defined in Appendix A.

In quasi-static representation of aerodynamic forces the static normal force coefficient C_N versus tanβ curve is represented by a polynomial in tanβ in the form Eq. 2.5

$$C_N = \sum_{n=0}^{N} P_n (\tan\beta)^n = \sum_{n=0}^{N} P_n \left(\frac{\partial W}{\partial t}/U\right)^n \tag{3.4}$$

Introducing Eq. 3.4 into Eq. 3.3 gives

$$\ddot{q}_{b_1} + 2\zeta_1 \dot{q}_{b_1} + q_{b_1} = \frac{1}{2}\tilde{\rho} u^2 \sum_{n=0}^{N} G_n \left(\dot{q}_{b_1}/u\right)^n \tag{3.5}$$

where $G_n = P_n A_n = P_n \frac{1}{A_1}\int_0^1 [f_1(\xi)]^{n+1} d\xi$

$(\dot{}) = \frac{d(\ )}{d\tau}$

The numerical values of A_n are given in Appendix A. Subtracting out the static part from above and using q_1 to denote the dynamic part, Eq. 3.5 becomes

$$\ddot{q}_{\beta_1} + g_1 \dot{q}_{\beta_1} - \tfrac{1}{2}\tilde{\rho} u^2 \sum_{n=2}^{N} G_n \left(\dot{q}_{\beta_1}/u\right)^n + q_{\beta_1} = 0 \qquad (3.6)$$

where

$$g_1 = \left(2\zeta_1 - \tfrac{1}{2}\tilde{\rho} u P_1\right)$$

The terms under summation sign contain all the nonlinear terms. The solution of the linear equation is given by

$$q_{\beta_1} = a\, e^{-\frac{g_1}{2}\tau} \sin\left(\sqrt{1-\left(\tfrac{g_1}{2}\right)^2}\,\tau + \phi\right) \qquad (3.7)$$

a and ϕ are arbitrary constants. When $g_1>0$, the oscillations die out. Beyond the critical velocity $u_c=4\zeta_1/\tilde{\rho}P_1$, when $g_1<0$, the oscillations grow and full nonlinear equation need to be considered. If the amplitude is plotted against time in a semi log paper from an experimental transient record, the initial slope should be linear and equal to the $(\frac{1}{4}\tilde{\rho}uP_1-\zeta_1)$ if the quasi-static theory works. In general $|g_1|<<1$ and the frequency of oscillation is nearly equal to the natural frequency.

The solution of full Eq. 3.6 is discussed in detail by Bogoliubov (Ref. 32), Parkinson (Ref. 18) and many other authors using the Krylov and Bogoliubov's method of slowly varying amplitude and phase. The equations can have stable and unstable limit cycle solutions, depending on the values of G_n. They appear as concentric circles in the phase plane whose origin is an unstable focus. In this report Eq. 3.6 is solved by

harmonic balance method to determine the limit cycle solutions. The stability is checked by slightly perturbing the steady state solution. All these methods involve the assumption that the nonlinearity is small compared to the inertia and elasticity terms and the oscillations are close to the sinusoidal motion near the natural frequency. For a square section body in low subsonic flow, these are realistic assumptions.

Let the steady state solution be given by

$$q_1 = a_1 \sin\tau + b_1 \cos\tau \tag{3.8}$$

Substituting Eq. 3.8 in Eq. 3.6, collecting the coefficients of sinτ and cosτ and setting them to zero one obtains

Sinτ:

$$-q_1 b_1 + \frac{1}{2}\tilde{\rho} u^2 \sum_{n=3,5,..} \frac{\tilde{G}_n}{u^n} b_1 \left(a_1^2 + b_1^2\right)^{\frac{n-1}{2}} = 0$$

Cosτ: (3.9)

$$q_1 a_1 - \frac{1}{2}\tilde{\rho} u^2 \sum_{n=3,5,..} \frac{\tilde{G}_n}{u^n} a_1 \left(a_1^2 + b_1^2\right)^{\frac{n-1}{2}} = 0$$

where

$$\tilde{G}_n = G_n 2 \frac{n(n-2)(n-4)\cdots\cdots(3)(1)}{(n+1)(n-1)(n-3)\qquad\qquad(4)(2)}$$

Setting $a = \sqrt{a_1^2 + b_1^2}$, Eq. 3.9 reduces to,

$$q_1 a - \frac{1}{2}\tilde{\rho} u^2 \sum_{n=3,5,..} \tilde{G}_n (a/u)^n = 0 \tag{3.10}$$

This nonlinear algebraic equation in a can now be solved to give

the limit cycle amplitude at a given u and ζ_1. Eq. 3.10 can be expressed in another nondimensional form

$$\frac{1}{\bar{u}}\left(\frac{\bar{a}}{\bar{u}}\right) - \sum_{n=1,3,5..} \tilde{G}_n \left(\frac{\bar{a}}{\bar{u}}\right)^n = 0 \qquad (3.11)$$

where

$$\bar{a} = a\,(\tilde{\rho}/4\zeta_1)$$

$$\bar{u} = u\,(\tilde{\rho}/4\zeta_1)$$

For a given $(\bar{a}/\bar{u})$, one can calculate $\bar{u}$ without solving Eq. 3.11 for $\bar{a}$. The resultant plot of $\bar{a}$ vs. $\bar{u}$ serves as a master plot for a particular C_N vs. tanβ data (3.4). This was suggested by Novak (Ref. 23). It may be noted that $(a/u)=(\bar{a}/\bar{u})$ and the induced angle of attack β at the tip of the beam is given by $\tan\beta=2(a/u)$ for our chosen mode shape. Thus the steady state solution is given by

$$\frac{W}{b} = f_1(\xi)\, a \,\sin\tau \qquad (3.12)$$

at a reduced velocity $u \equiv U/\omega_1 b$. For example, for a fifth degree polynomial fit in Eq. 3.4, Eq. 3.11 takes the form

$$\frac{1}{\bar{u}}\left(\frac{\bar{a}}{\bar{u}}\right) - \left[P_1\left(\frac{\bar{a}}{\bar{u}}\right) + 1.761\, P_3\left(\frac{\bar{a}}{\bar{u}}\right)^3 + 4.17\, P_5\left(\frac{\bar{a}}{\bar{u}}\right)^5\right] = 0$$

Eq. 3.10 gives both stable and unstable limit cycle solutions so each of the solutions must be tested for stability Giving a small perturbation to the steady state solution, q_{b1} is written in the form

$$q_{b_1} = \left(a_s + \xi(\tau)\right) \sin\tau \qquad (3.13)$$

Here a_s is a steady state solution satisfying Eq. 3.10 and $\xi(\tau)$ is a small perturbation from the steady state solution. It is also assumed to be a slowly varying function which means that the increase of such a function during one period is small compared to the average value for that period

$$\left|\frac{\dot{\xi}(\tau)\, 2\pi}{\xi(\tau)}\right| \ll 1 \qquad \left|\frac{\ddot{\xi}(\tau)\, 2\pi}{\dot{\xi}(\tau)}\right| \ll 1 \tag{3.14}$$

According to this assumption

$$\begin{aligned} \dot{q}_{b1} &\approx \left[a_s + \xi(\tau)\right] \cos\tau \\ \ddot{q}_{b1} &\approx -\left[a_s + \xi(\tau)\right] \sin\tau + 2\dot{\xi}(\tau) \cos\tau \end{aligned} \tag{3.15}$$

Substituting this in Eq. 3.6 coefficients of $\sin\tau$ get cancelled. Setting coefficients of $\cos\tau$ to zero, cancelling out the steady state solution and keeping only the linear terms in $\xi(\tau)$, one obtains

$$2\dot{\xi}(\tau) + \frac{dF(a_s)}{da_s}\,\xi(\tau) = 0 \tag{3.16}$$

where

$$F(a) = 2\zeta_1 a - \tfrac{1}{2}\tilde{\rho}u^2 \sum_{n=1,3,5..} \tilde{G}_n\,(a/u)^n$$

It may be noted that $F(a_s)=0$ gives the steady state solution. Thus in order that the steady state solution be stable, one must have $\frac{dF(a)}{da}$ positive at $F(a)=0$.

A graphical representation of the steady state solution and stability is explained below. Using the nondimensional nòtation of (3.11)

$$F(a) = \tfrac{1}{2}\tilde{\rho}u^2\left[\frac{1}{\bar{u}}\left(\frac{\bar{a}}{\bar{u}}\right) - \sum_{n=1,3,5,\cdots}\tilde{G}_n\left(\frac{\bar{a}}{\bar{u}}\right)^n\right]$$

$$\frac{dF(a)}{da} = \tfrac{1}{2}\tilde{\rho}u\left[\frac{1}{\bar{u}} - \frac{d}{d(\bar{a}/\bar{u})}\left\{\sum_{n=1,3,5,\cdots}\tilde{G}_n\left(\frac{\bar{a}}{\bar{u}}\right)^n\right\}\right] \quad (3.17)$$

Plotting $\sum\tilde{G}_n(\bar{a}/\bar{u})^n$ versus $(\bar{a}/\bar{u})$, steady state solutions at a given $\bar{u}$ are obtained from the intersection with a straight line from origin and with slope $1/\bar{u}$. The solution is stable if the slope of the straight line is greater than the slope of the curve at the point of intersection.

Thus if the $\sum\tilde{G}_n(\bar{a}/\bar{u})^n$ plot is as shown in Fig. 16a, B_2 represents unstable limit cycle solution. Fig. 16b shows the nature of steady state amplitude variation with $\bar{u}$. The dotted portion represents unstable limit cycle solution. At large velocity the amplitude is asymptotic to a line of slope D.

If the $\sum\tilde{G}_n(\bar{a}/\bar{u})^n$ plot is as shown in Fig. 16c all the steady state solutions are stable. If this is as shown in Figs. 16e and 16g, A_2 represents the unstable solution. These different forms of amplitude response for bodies of various cross section have been discussed by Novak (Ref. 24) and stability proven by the method of Krylov and Bogoliubov. By the present method, the steady state amplitude and stability can be determined just by looking at the $\sum_{n=1,3,\cdots}\tilde{G}_n(\bar{a}/\bar{u})^n$ plot.

3.3 Two Degrees of Freedom Motion

In Section 3.2, the motion of the vertical cantilever beam at zero initial angle of attack is assumed to be in a plane normal to the free stream direction. This is found to be a reasonable assumption experimentally for this cantilever beam which has no directional preference of motion structurally.

However, when the beam is initially at an angle of attack, (see Fig. 2d), the motion is generally in a plane slightly inclined to the z direction. This inclination is presumably decided by the aerodynamic forces alone. Assuming that the beam can vibrate freely in all directions with the same natural frequency and does not undergo any torsional motion under the existing forces, the equation of motion can be written in the same form as Eq. 3.1, namely,

$$m\frac{\partial^2 W}{\partial t^2} + c\frac{\partial W}{\partial t} + EI\frac{\partial^4 W}{\partial x^4} = \frac{1}{2}\rho U^2 b C_z\left(\frac{\partial W}{\partial t}/U, \frac{\partial V}{\partial t}/U, \alpha_o\right)$$

$$m\frac{\partial^2 V}{\partial t^2} + c\frac{\partial V}{\partial t} + EI\frac{\partial^4 V}{\partial x^4} = \frac{1}{2}\rho U^2 b C_Y\left(\frac{\partial W}{\partial t}/U, \frac{\partial V}{\partial t}/U, \alpha_o\right) \qquad (3.18)$$

Here w(x,t) is the displacement normal to the wind direction; v(x,t) is the displacement along the wind direction; c is the structural damping coefficient expressed in the form of viscous damping; α_o is the initial angle of attack and the right hand terms represent aerodynamic forces induced by the motion. Again, applying Galerkin's approximation to reduce Eq. 3.18 to ordinary differential equation in time t using only one mode for w and v

$$W(\xi,t) = b f_1(\xi) q_1(t)$$
$$V(\xi,t) = b f_1(\xi) q_2(t) \qquad \xi = x/\ell \qquad (3.19)$$

where $f_1(\xi)$ is the first bending mode shape as in Eq. 3.2, the Eq. 3.18 becomes after some nondimensionalization

$$\ddot{q}_1 + 2\zeta_1\dot{q}_1 + q_1 = \frac{1}{2}\tilde{\rho}u^2\frac{1}{A_1}\int_0^1 C_z\left(\frac{f_1(\xi)}{u}\dot{q}_1, \frac{f_1(\xi)}{u}\dot{q}_2, \alpha_o\right) f_1(\xi)\,d\xi$$
$$\ddot{q}_2 + 2\zeta_1\dot{q}_2 + q_2 = \frac{1}{2}\tilde{\rho}u^2\frac{1}{A_1}\int_0^1 C_Y\left(\frac{f_1(\xi)}{u}\dot{q}_1, \frac{f_1(\xi)}{u}\dot{q}_2, \alpha_o\right) f_1(\xi)\,d\xi \qquad (3.20)$$

where $\omega_1 t = \tau$

$\zeta_1 = c/2m\omega_1$

$(^{\circ}) = d(\,)/d\tau$

Other notations are the same as in Eq. 3.3. In Section 2.3 a quasi-static representation of the motion induced aerodynamic forces on a body translating with velocity $\dot{W}$ and $\dot{V}$ without rotation has been derived. Using the Eq. 2.14, C_Z and C_Y can be expressed in the form

$$C_Z = \left(1-\frac{\dot{V}}{U}\right)^2 \sum_{m=0}^{M} Z_m(\alpha_0)\,(\tan\beta)^m$$
$$C_Y = \left(1-\frac{\dot{V}}{U}\right)^2 \sum_{m=0}^{M} Y_m(\alpha_0)\,(\tan\beta)^m \qquad (3.21)$$

for small $|\tan\beta\tan\alpha_0|$. Now

$$\left(1-\frac{\dot{V}}{U}\right)^2(\tan\beta)^m = \left(\frac{\dot{W}}{U}\right)^m\left(1-\frac{\dot{V}}{U}\right)^{-(m-2)} \qquad (3.22)$$

In general, because of presence of damping due to drag, the stream-wise motion is very small, and one may write

$$\left(1-\frac{\dot{V}}{U}\right)^{-(m-2)} \approx 1 + (m-2)\left(\frac{\dot{V}}{U}\right) + \frac{(m-2)(m-1)}{2}\left(\frac{\dot{V}}{U}\right)^2 + \cdots \qquad (3.23)$$

In the present problem $|\dot{V}/U|<0.1$. Thus if M=7, only two terms need to be retained in the above approximation with only 4% error . C_Z, C_Y can now be expressed in the form .

$$C_Z = Z_0\left(1-\frac{\dot{V}}{U}\right)^2 + Z_1\left(\frac{\dot{W}}{U}\right)\left(1-\frac{\dot{V}}{U}\right) + Z_2\left(\frac{\dot{W}}{U}\right)^2 + \sum_{m=3}^{7}\sum_{n=0}^{2} Z_m N_{mn}\left(\frac{\dot{W}}{U}\right)^m\left(\frac{\dot{V}}{U}\right)^n \qquad (3.24)$$

C_Y expression is the same as C_Z except Z_m is replaced by Y_m. In this case $N_{mo}=1$, $N_{m1}=(m-2)$ $N_{m2}=(m-2)(m-1)/2$. Eq. 3.24 expresses C_Z, C_Y in terms of $\frac{\dot{W}}{U}, \frac{\dot{V}}{U}$ in a convenient form which can be converted to ordinary different equation in time using Galerkin's approximation. Introducing Eq. 3.24 in Eq. 3.20, one obtains after subtracting out the static part

$$\ddot{q}_1 + g_{11}\dot{q}_1 + g_{12}\dot{q}_2 - \tfrac{1}{2}\tilde{\rho}u^2\left[A_2\left\{Z_2\left(\frac{\dot{q}_1}{u}\right)^2 - Z_1\left(\frac{\dot{q}_1}{u}\frac{\dot{q}_2}{u}\right) + Z_0\left(\frac{\dot{q}_2}{u}\right)^2\right\} + \sum_{m=3}\sum_{n}\tilde{Z}_{mn}\left(\frac{\dot{q}_1}{u}\right)^m\left(\frac{\dot{q}_2}{u}\right)^n\right] + q_1 = 0$$

$$\ddot{q}_2 + g_{21}\dot{q}_1 + g_{22}\dot{q}_2 - \tfrac{1}{2}\tilde{\rho}u^2\left[A_2\left\{Y_2\left(\frac{\dot{q}_1}{u}\right)^2 - Y_1\left(\frac{\dot{q}_1}{u}\frac{\dot{q}_2}{u}\right) + Y_0\left(\frac{\dot{q}_2}{u}\right)^2\right\} + \sum_{m=3}\sum_{n}\tilde{Y}_{mn}\left(\frac{\dot{q}_1}{u}\right)^m\left(\frac{\dot{q}_2}{u}\right)^n\right] + q_2 = 0$$

where (3.25)

$$\tilde{Z}_{mn} = Z_m N_{mn} A_{m+n}$$

$$\tilde{Y}_{mn} = Y_m N_{mn} A_{m+n}$$

$$A_{m+n} = \frac{1}{A_1}\int_0^1 [f_1(\xi)]^{m+n+1}\, d\xi$$

$$g_{11} = (2\zeta_1 - \tfrac{1}{2}\tilde{\rho}u Z_1)$$

$$g_{12} = (\tilde{\rho}u Z_0)$$

$$g_{21} = (-\tfrac{1}{2}\tilde{\rho}u Y_1)$$

$$g_{22} = (2\zeta_1 + \tilde{\rho}u Y_0)$$

Here q_1, q_2 denote only dynamic terms since static parts have been subtracted out. The terms in the square bracket contain all the nonlinear terms. The mass and stiffness matrix are symmetric and positive definite. Thus the instability can arise only from the damping terms. It should be remembered that the self-excitation is mainly due to negative g_{11} and not because of interaction between q_1 and q_2.

First consider the linear part of the Eq. 3.25.

$$\begin{aligned} \ddot{q}_1 + g_{11}\dot{q}_1 + g_{12}\dot{q}_2 + q_1 &= 0 \\ \ddot{q}_2 + g_{21}\dot{q}_1 + g_{22}\dot{q}_2 + q_2 &= 0 \end{aligned} \tag{3.26}$$

Let the solution be $q_1=a_1e^{p\tau}$, $q_2=a_2e^{p\tau}$. Substituting them in Eq. 3.26 a pair of homogeneous simultaneous equations in a_1 and a_2 are obtained.

$$\begin{bmatrix} (p^2+g_{11}p+1) & g_{12}p \\ g_{21}p & (p^2+g_{22}p+1) \end{bmatrix} \begin{Bmatrix} a_1 \\ a_2 \end{Bmatrix} = 0 \tag{3.27}$$

For non-trivial solution, the determinant of the coefficients must be zero. The variable parameter is the reduced velocity u. It may be noted that for a perfectly symmetric cross section body at $\alpha_o=0$ $g_{12}=0$ $g_{21}=0$ and the linear equations are uncoupled. Since g_{22} is positive, the motion in streamwise direction die down. Thus if g_{11} is negative, the motion normal to the free stream direction is only excited. The equations become coupled if the square section is at an initial angle of attack α_o, or if P_o and Q_1 are not zero . $\alpha_o=0$ (for example, if the section is not perfectly symmetric). From experiment, it is found that the motion for the initial angle cases is not normal to the wind direction but in a plane inclined to it. Setting the determinant of coefficients of Eq. 3.27 to zero a fourth

degree polynomial in p is obtained which can be solved to give

$$p = \sigma \pm i\sqrt{1-\sigma^2}$$

where

$$2\sigma = -\left(\frac{g_{11}+g_{22}}{2}\right) \pm \sqrt{\left(\frac{g_{11}+g_{22}}{2}\right)^2 - \left(g_{11}g_{22} - g_{12}g_{21}\right)} \qquad (3.28)$$

It can be seen that at low velocity when $(g_{11}g_{22}-g_{12}g_{21})>0$ both the values of σ are negative since in general $(g_{11}+g_{22})$ is positive for a square cross section body, at all velocity. The oscillations die down. As u is increased, flutter condition is reached when

$$\left(g_{11}g_{22} - g_{12}g_{21}\right) = 0 \qquad (3.29)$$

which makes $\sigma=0$ and $p=\pm i$. Thus the flutter frequency is the same as the natural frequency ω_1. It should, however, be remembered that the self-excitation occurs because of the negative damping term g_{11} and not due to interaction of q_{b1} and q_{b2}.

The Eq. 3.29 can be solved for u to give the critical velocity u_c

$$\tilde{\rho} u_c = \zeta_1 \left\{ \frac{(2Y_0 - Z_1) + \sqrt{(2Y_0 - Z_1)^2 + 8(Z_1Y_0 - Y_1Z_0)}}{(Z_1Y_0 - Y_1Z_0)} \right\} \qquad (3.30)$$

ignoring the negative value.

At $u>u_c$ one of the values of σ becomes positive and the oscillations grow. The motion corresponding to the negative σ die out. In general, $|\sigma|<<1$ and the frequency of oscillation is close to the natural frequency. Thus

$$p \approx \sigma \pm i \qquad (3.31)$$

Substituting this in Eq. 3.27 and using the assumption $\sigma^2 << 1$

$$\frac{a_2}{a_1} \approx -\frac{g_{21}}{(g_{22}+2\sigma)} e^{\pm i\theta} \qquad \tan\theta \approx -\sigma \quad (3.32)$$

For the specimen used in the experiment, at low subsonic speed σ is of order 0.01 so the phase difference between q_1 and q_2 at low amplitude is small and the initial motion is in an inclined plane. The phase difference between q_1 and q_2 represents an elliptic whirling motion. It should be noticed that at critical velocity u_c, q_1 and q_2 are in phase and the motion is purely planar.

Let us now look for steady state solution of the total Eq. 3.25. Since the elasticity terms are linear, and the linear and nonlinear damping terms are small, the frequency of oscillation beyond the critical velocity are close to the natural frequency of oscillation. Thus a steady state solution to equation (3.25) can be taken as

$$\begin{aligned} q_1 &= a_1 \sin\tau + b_1 \cos\tau \\ q_2 &= a_2 \sin\tau + b_2 \cos\tau \end{aligned} \qquad (3.33)$$

Substituting these into Eq. 3.25, collecting coefficients of sinτ, cosτ and setting them to zero one obtains four algebraic equations coming only from the first derivative terms.

$$\sin\tau: \quad -g_{11}b_1 - g_{12}b_2 - \tfrac{1}{2}\tilde{\rho}u^2 f_{s1}(a_1,b_1,a_2,b_2) = 0$$

$$\cos\tau: \quad g_{11}a_1 + g_{12}a_2 - \tfrac{1}{2}\tilde{\rho}u^2 f_{c1}(a_1,b_1,a_2,b_2) = 0$$

$$\sin\tau: \quad -g_{21}b_1 - g_{22}b_2 - \tfrac{1}{2}\tilde{\rho}u^2 f_{s2}(a_1,b_1,a_2,b_2) = 0$$

$$\cos\tau: \quad g_{21}a_1 + g_{22}a_2 - \tfrac{1}{2}\tilde{\rho}u^2 f_{c2}(a_1,b_1,a_2,b_2) = 0$$

(3.34 a,b,c,d)

Here $f_{s1}(a_1,b_1,a_2,b_2)$ etc. contain all the nonlinear terms in a_1,b_1,c_1,d_1 and are given in Appendix B for a general polynomial fit of aerodynamic data for the case $b_1=0$. In steady state limit cycle solution, the starting point of time is irrelevant and b_1 can be set to zero. Setting also $b_2=0$ Eq. 3.34a,c are automatically satisfied and one is left with two equations (3.34b,d) with two unknowns a_1 and a_2.

$$\begin{aligned} g_{11}\, a_1 + g_{12}\, a_2 - \tfrac{1}{2}\tilde{\rho} u^2 f_{c1}(a_1,a_2) &= 0 \\ g_{21}\, a_1 + g_{22}\, a_2 - \tfrac{1}{2}\tilde{\rho} u^2 f_{c2}(a_1,a_2) &= 0 \end{aligned} \qquad (3.35\ a,b)$$

which can be solved at a given u to obtain the steady state solution.

$$\begin{aligned} \frac{W}{b} &= f_1(\xi)\, a_1 \sin\tau \\ \frac{V}{b} &= f_1(\xi)\, a_2 \sin\tau \end{aligned} \qquad (3.36)$$

The inclination of the plane of the motion with respect tc the z axis is given by

$$\gamma = \tan^{-1}(a_2/a_1) \qquad (3.37)$$

Positive γ has the same sign convention as positive α_o. The total tip amplitude W_T is given by

$$\frac{W_T}{b} = 2a_1/\cos\gamma \qquad (3.38)$$

It may be noted that Eq. 3.35 can be nondimensionalized in the special form of Eq. 3.11.

To examine the stability of the steady state solution, we again assume

$$q_{f_1} = [\, a_{1s} + \xi(\tau)] \sin\tau$$

$$q_{f_2} = [\, a_{2s} + \eta(\tau)] \sin\tau \qquad (3.39)$$

where a_{1s}, a_{2s} are steady state solutions satisfying Eq. 3.35 and $\xi(\tau)$, $\eta(\tau)$ are slowly varying functions as defined in Eq. 3.14. Thus proceeding in the same manner

$$\begin{aligned}
\dot{q}_{f_1} &\approx [\, a_{1s} + \xi(\tau)\,] \cos\tau \\
\dot{q}_{f_2} &\approx [\, a_{2s} + \eta(\tau)\,] \cos\tau \\
\ddot{q}_{f_1} &\approx -[\, a_{1s} + \xi(\tau)\,] \sin\tau + 2\dot{\xi}(\tau) \cos\tau \\
\ddot{q}_{f_2} &\approx -[\, a_{2s} + \eta(\tau)\,] \sin\tau + 2\dot{\eta}(\tau) \cos\tau
\end{aligned} \qquad (3.40)$$

Substituting these in Eq. 3.35, the coefficients of sinτ get cancelled. Setting coefficients of cosτ to zero, cancelling out the steady state solution and keeping only the linear terms in $\xi(\tau)$ and $\eta(\tau)$, one obtains

$$\begin{bmatrix} 1 & 0 \\ 0 & 1 \end{bmatrix} \begin{Bmatrix} \dot{\xi} \\ \dot{\eta} \end{Bmatrix} + \begin{bmatrix} a_{11} & a_{12} \\ a_{21} & a_{22} \end{bmatrix} \begin{Bmatrix} \xi \\ \eta \end{Bmatrix} = 0 \qquad (3.41)$$

where

$$a_{11} = \tfrac{1}{2}\left(q_{11} - \tfrac{1}{2}\tilde{\rho} u^2 \frac{\partial f_{c1}}{\partial a_1} \right)$$

$$a_{12} = \tfrac{1}{2}\left(q_{12} - \tfrac{1}{2}\tilde{\rho} u^2 \frac{\partial f_{c1}}{\partial a_2} \right)$$

$$a_{21} = \tfrac{1}{2}\left(q_{21} - \tfrac{1}{2}\tilde{\rho} u^2 \frac{\partial f_{c2}}{\partial a_1} \right)$$

$$a_{22} = \tfrac{1}{2}\left(q_{22} - \tfrac{1}{2}\tilde{\rho} u^2 \frac{\partial f_{c2}}{\partial a_2} \right) \qquad \text{AT} \quad a_1 = a_{1s},\ a_2 = a_{2s}$$

This gives the familiar eigenvalue problem. For stability, the root of the characteristic equation

$$p^2 + p(a_{11} + a_{22}) + (a_{11}a_{22} - a_{12}a_{21}) = 0 \qquad (3.42)$$

must have -ve real part. The condition is given by

$$\begin{aligned} (a_{11} + a_{22}) &> 0 \\ (a_{11}a_{22} - a_{12}a_{21}) &> 0 \end{aligned} \qquad (3.43)$$

Let us now consider a simple example for which C_N and C_C are given by

$$\begin{aligned} C_N &= P_1 \tan\beta + P_3 \tan^3\beta \\ C_C &= Q_0 + Q_2 \tan^2\beta + Q_4 \tan^4\beta \end{aligned} \qquad (3.44)$$

In order to get a feel for the quantities involved, P_1=0.9, P_3=-8, Q_0=1.24, Q_2=-3, Q_4=30 roughly fits the experimental data shown in Figs. 7a, 8a up to $\tan\beta$=0.45 if one ignores the small off-symmetries. In one degree of freedom case this form of C_N has the response characteristic as shown in Fig. 16c in Section 3.2. There is one stable limit cycle solution and the limit cycle amplitude increases monotonically with u. With the limitation $|\tan\beta\tan\alpha_0|<0.1$, $|\dot{V}/U|<0.1$ the harmonic balance equations (3.35) are

$$\begin{aligned} q_{11}a_1 + q_{12}a_2 - \tfrac{1}{2}\tilde{\rho}u^2\Big[1.761\, Z_3\Big(\frac{a_1}{u}\Big)^3 + 8.34\, Z_4\Big(\frac{a_1}{u}\Big)^4\Big(\frac{a_2}{u}\Big) \\ + 4.17\, Z_5\Big(\frac{a_1}{u}\Big)^5\Big] = 0 \\ q_{21}a_1 + q_{22}a_2 - \tfrac{1}{2}\tilde{\rho}u^2\Big[1.761\, Y_3\Big(\frac{a_1}{u}\Big)^3 + 8.34\, Y_4\Big(\frac{a_1}{u}\Big)^4\Big(\frac{a_2}{u}\Big) \\ + 4.17\, Z_5\Big(\frac{a_1}{u}\Big)^5\Big] = 0 \end{aligned} \qquad (3.45)$$

with the approximate quasi-static representation. Adopting the nondimensional form of (3.11), Eq. 3.45 become after division by (a_1/u_1)

$$\left(\frac{1}{\bar{u}} - Z_1\right) + 2Z_0\tilde{\gamma} - \left[1.761\, Z_3\left(\frac{\bar{a}_1}{\bar{u}}\right)^2 + 8.34\, Z_4\left(\frac{\bar{a}_1}{\bar{u}}\right)^4\tilde{\gamma} + 4.17\, Z_5\left(\frac{\bar{a}_1}{\bar{u}}\right)^4\right] = 0 \qquad (3.46\ a,b)$$

$$-Y_1 + \left(\frac{1}{\bar{u}} + 2Y_0\right)\tilde{\gamma} - \left[1.761\, Y_3\left(\frac{\bar{a}_1}{\bar{u}}\right)^2 + 8.34\, Y_4\left(\frac{\bar{a}_1}{\bar{u}}\right)^4\tilde{\gamma} + 4.17\, Y_5\left(\frac{\bar{a}_1}{\bar{u}}\right)^4\right] = 0$$

where

$$\bar{u} = u(\tilde{\rho}/4\zeta_1)$$

$$\bar{a}_1 = a_1(\tilde{\rho}/4\zeta_1)$$

$$\frac{a_2}{a_1} = \tan\gamma = \tilde{\gamma}$$

Here $Z_0..Z_5$, $Y_0..Y_5$ are functions of P_0, P_1, P_3, Q_0, Q_2, Q_4 and α_0 and are given in Appendix C. Since C_N is cubic, the second and third terms in square bracket of Eq. 3.46a are very small compared to the first term and can be neglected. From Eq. 3.46b

$$\tan\gamma \equiv \tilde{\gamma} = \frac{Y_1 + 1.761\, Y_3\left(\frac{\bar{a}_1}{\bar{u}}\right)^2 + 4.17\, Y_5\left(\frac{\bar{a}_1}{\bar{u}}\right)^4}{\left(\frac{1}{\bar{u}} + 2Y_0\right) - 8.34\, Y_4\left(\frac{\bar{a}_1}{\bar{u}}\right)^4} \qquad (3.47)$$

In determining $(\bar{a}_1/\bar{u})$ by substituting (3.47) in (3.46a), one may ignore the fourth power terms and get

$$\left(\frac{\bar{a}_1}{\bar{u}}\right) = \sqrt{\frac{\left(\frac{1}{\bar{u}} - Z_1\right) + 2Z_0Y_1/\left(\frac{1}{\bar{u}} + 2Y_0\right)}{1.761\left\{Z_3 - 2Z_0Y_3/\left(\frac{1}{\bar{u}} + 2Y_0\right)\right\}}} \qquad (3.48)$$

The limit cycle solution is possible only if the term under the radical sign is positive. If C_N is antisymmetric and C_C symmetric in β then at $\alpha_o=0$ y_1, y_3, y_5 are zero and the solution is given by

$$\frac{\bar{a}_1}{\bar{u}} = \sqrt{\left(\frac{1}{\bar{u}} - Z_1\right)/1.761 Z_3}$$
$$\tan\gamma = 0 \qquad (3.49)$$

If $Q_4=0$, one may ignore y_3, y_4, y_5. Then $\tan\gamma$ is approximately given by

$$\tan\gamma \approx \frac{Y_1}{\frac{1}{\bar{u}} + 2Y_0} \approx \frac{Y_1}{2Y_0} \approx \left(1 - \frac{Q_2}{Q_0}\right)\tan\alpha_o \qquad (3.50)$$

Thus qualitatively if no drag variation with β is considered then $\gamma\approx\alpha_o$; if the drag increases with β, $Q_2>0$, $\gamma<\alpha_0$; if the drag decreases with β, $Q_2<0$, $\gamma>\alpha_o$. When Q_4 is included the problem is more involved. Numerical examples are considered in Section 4. In general, γ does not affect $\bar{a}_1$ very much. $\bar{a}_1$ is primarily determined by Z_1 and Z_3.

SECTION 4

EXPERIMENT WITH CANTILEVER BEAN

4.1 Introduction

Since no purely theoretical method of predicting the aero dynamic forces on a blunt body with a turbulent wake exists, experimental observations form the basis of the present investigation. The quasi-static representation of the aerodynamic forces constitute one of the means of predicting the response of a self-excited square section body. So experiments have ben conducted with a square section cantilever beam placed in a uniform wind stream. First the static lift and drag forces are determined and are used in quasi-static theory to determine the responses. Then tests are carried out to determine the response experimentally with the specimen at various initial angles of attack. Some interesting response phenomena are observed. They are described in Section 4.3. In Section 4.4 the results obtained by this quasi-static theory using the static test lift and drag data are compared with experiment. Only qualitative agreement has been observed.

A movie of the experiment has been taken, which shows the self-excitation phenomena. The transient motion and the response at various angles of attack can be clearly observed.

4.2 Static Force Measurement

The experiment with the cantilever beam is carried out in a 1 ft. x 1 ft. low speed wind tunnel. The air is blown into the tunnel by a blower and is smoothed out by a series of netting and honeycomb mesh. The velocity is increased by the area contraction ratio of 36:1. The flow is smooth and nearly free from turbulence. The specimen is placed in the open jet 1.5 inches from the end of tunnel as shown in Figs. 1 and 2a. All the velocities mentioned

are the velocities just inside the tunnel and are used as the reference velocity throughout the report. Before the testing the velocity near the specimen position is measured with a pitot tube whose total pressure holes are at 1.5 inches from the end of the tunnel and static pressure holes 1" farther behind. In Fig. 4, this is plotted against the reference velocity. The reduction in velocity at the specimen position due to the open jet effect is found to be less than 2% at all reference speeds up to 80 ft/sec. and can be considered within tolerable experimental error.

The specimen cantilever beam is made of 1/8 inch diameter steel rod and is 13.1 inches long. It is coated with wax and drawn through a square template to give it a square cross section outside. The side of the square is 0.09 inches. The section is not perfectly square but is slightly rounded at the edges. The wax coating is thin and does not change the structural property of the rod appreciably. Thus the rod can be assumed to have the same area moment of inertia in all directions. It is free to deflect in any direction without twisting and with some bending stiffness. This simplifies the theoretical analysis considerably. The 13.1 inches long specimen is clamped in a vertical position and the base is bolted to the top of a turn table which can be rotated through 360°. The orientation of the specimen with respect to the wind stream direction and the chosen coordinate axes are shown in Figs. 2a, 2b. The four sides are identified as side A, B, C, D with respect to a small 120 ohm strain gage which is placed at the root of the beam on side B to record the transient motion. When the side A is facing the wind stream, the general position is termed as position A and so on. The static and dynamic calibration of the strain gage is shown in Fig. 9 at position A, $\alpha_o = 0$ for different tip deflection W_T in Z direction, and is quite linear. There are small variations if the motion is slightly inclined from Z direction.

The clamped end of the specimen is 2 inches below the wind tunnel floor to avoid flow disturbance from the base support fixtures. Since there is little motion at the root, the motion induced forces are negligible and the set up does not affect the response significantly. Tests are first conducted to determine the static lift and drag forces at various angles of attack. This is done by measuring the static tip deflection in Z and Y directions visually, at different angle of attack position α as shown in Fig. 2b, and then calculating the force, assuming uniform load over the span of the beam exposed to the wind, using linear force deflection relation.

$$C_L = 8EI\, W_T \Big/ \tfrac{1}{2}\rho U^2 b \ell^4 \left[1 - \tfrac{8}{6}\left(\tfrac{\Delta\ell}{\ell}\right)^3 + \tfrac{1}{3}\left(\tfrac{\Delta\ell}{\ell}\right)^4 \right]$$

$$C_D = 8EI\, V_T \Big/ \tfrac{1}{2}\rho U^2 b \ell^4 \left[1 - \tfrac{8}{6}\left(\tfrac{\Delta\ell}{\ell}\right)^3 + \tfrac{1}{3}\left(\tfrac{\Delta\ell}{\ell}\right)^4 \right] \qquad (4.1)$$

Here $\Delta\ell$ is the portion of the beam at the root which is outside the wind stream. For $\Delta\ell$ = 2 inches, ℓ = 13.1 inches, the factor $\left[1 - \tfrac{8}{6}\left(\tfrac{\Delta\ell}{\ell}\right)^3 + \tfrac{1}{3}\left(\tfrac{\Delta\ell}{\ell}\right)^4 \right]$ = 0.9955, showing that the effect is very small. C_L, C_D are computed at 37, 44, 56, 65 ft/sec velocity for position A and at 37, 45 ft/sec velocity for position D, and are shown in Figs. 5 and 6. The variation in C_L, C_D from the error in measurement of deflection is less than 5%. It is observed that while C_L remains relatively unaffected by velocity, there appears a Reynolds number effect on C_D. For an increase in Reynolds number from 1800 to 3100, C_D increases from 1.24 to 1.54 at α = 0. The square section C_L is characterized by the negative lift curve slope in the vicinity of zero degree angle of attack. The lift attains peak value near α = 12° where drag reaches a minimum. In this vicinity the flow first reattaches on one side and the wake has minimum width. Beyond this angle the flow is fully attached to both the windward faces but the wake width

increases as the square is rotated farther, and the drag increases simultaneously. Even though the general nature of C_L, C_D variation with α are similar for the position A and D, the differences are noticeable at small angles of attack, signifying that the static forces are quite sensitive to the imperfections and sharpness of the edges.

Using the C_L, C_D data, $C_N(\beta)$, $C_C(\beta)$ as defined in Eq. 2.4 are computed and plotted against $\tan\beta$ in Figs. 7 and 8. An 8th degree polynomial least square fit is shown in solid line. The fit is good only up to $\tan\beta = \pm 0.45$ and does not fit properly near sharp peaks. The coefficients of the polynomials P_n and Q_n are given in Table 2.

4.3 Description of Experimental Result

The first natural bending frequency of the beam is 9.4 cycles/sec. The theoretical estimation with bending rigidity for a 1/8 inch round steel rod gives 9.5 cy/sec showing that the wax coating does not affect the structural stiffness. First the critical damping ratio is obtained from the dynamic decay record by plotting the transient amplitude against time on semi-log paper, and is shown in Fig. 10 along with a typical decay record. The damping ratio is constant at very low amplitude but varies linearly at higher amplitude. The constant value is due to viscous and structural damping. The linear variation is due to the aerodynamic damping as the body moves through still air. If it is assumed that the drag at any point of the harmonically oscillating beam is proportional to the square of the velocity at that point, then it can be shown by equating the work done over a cycle, the equivalent damping ratio is proportional to the amplitude of the cycle.

$$\zeta_{Eq} = \frac{1}{3\pi} \tilde{\rho} \, A_2 C_D \frac{\omega}{\omega_1} \left(\frac{W_T}{b}\right) \qquad (4.2)$$

W_T is the tip amplitude and $\tilde{\rho}$, A_1, A_2, ω_1 are as defined in Eq. 3.3. This is plotted in Fig. 10b from the origin for $C_D = 1.6$ and 2. Since $\zeta_1 << 1$, $\omega/\omega_1 \approx 1$, it can be seen that the slopes of linear ζ_{EQ} variation are much smaller than the experimental plot. For $C_D = 1.6$, the $\zeta_{EQ} = 0.87 \times 10^{-4}(W_T/b)$ whereas the slope of experimental linear variation $\zeta_{EQ} \approx 3.8 \times 10^{-4}(W_T/b)$ which is four times as much. It is not quite clear why this is so but one of the reasons could be that the beam is actually not moving through still air but sets the wind in motion as it moves through it. As it swings back, it meets the incoming turbulent wind which in effect doubles the net velocity and the drag is four times as much. It should be noted that when the beam is oscillating laterally in a wind stream this air damping in that direction is no longer present. Only the structural damping which is obtained from the intercept of the experimental curve on the ζ_1 axis, impedes the motion in this situation. This is estimated to be between .002 and .0025 in terms of critical damping ratio. The value .002 is used for all calculations.

The response at zero degree initial angle of attack is measured for all the four positions A, B, C, D, i.e., with each of the four sides facing the wind stream. The turn table is clamped at the position A at zero degree angle of attack and tunnel is turned on. At a speed below the critical velocity, there is no response. When the beam is disturbed, the oscillations die down. The wind velocity is then increased in small steps. At around 10 ft/sec, the beam begins to oscillate by itself. The amplitude increases slowly and then settles down to a steady state. To record the transient motion at a particular velocity, the beam is brought to rest by touching it at the top and then letting go. The Sanborn recorder which is hooked up to the strain gage is turned on simultaneously. The amplitude grows slowly and then settles down to a steady state limit cycle. The final amplitude is quite steady, signifying absence of large scale turbulence in

the flow. The beam is then given a small kick to see if it comes back to the same steady state value. It is then given a big kick to examine if there are other limit cycle solutions at that velocity. The steady state tip amplitude is measured visually with a scale held on top of the tunnel outside the wind stream. Some of these measurements are compared with static calibration of the strain gage done at the beginning of the experiment for various tip deflections due to an end load, and is given in Fig. 9. They are almost the same if motion is nearly normal to the wind stream direction. The steady state amplitude and transient response are recorded for the position A for velocities up to 65 ft/sec. The velocity is then reduced in steps and the amplitudes are measured. The process is repeated at zero degree angle of attack with sides B, C, D facing the wind stream, but no transient records are taken. The result is plotted in Fig. 11a. W_T is the tip amplitude. It is observed that even for amplitudes as large as $W_T/b = 31$, the frequency is still nearly 9.4 cycles/second as in small amplitude oscillation. The steady state amplitude variation with velocity is more or less the same for all the four sides up to about 25 ft/sec. Beyond this velocity there is a marked departure. In position A, the amplitude levels off and then drops as the velocity is increased to 45 ft/sec but rises again as the velocity is increased farther. Similar response variation is observed for the position B and C but the drop off and rise occurs at different velocities. For position D, however, the amplitude rises monotonically with velocity to a large amplitude of $W_T/b = 31$ at 55 ft/sec. The specimen is not tested beyond this velocity to avoid its destruction. With two dimensional square section body, response behavior of form shown in Figs. 16a, 16c have been observed but this type of behavior is rather unusual. In order to investigate this peculiar amplitude response in position A, B, C, further tests are conducted for the specimen position A and D so that the basic differences can be detected.

Now instead of keeping the specimen at zero initial angle of of attack, it is placed at a small initial angle of attack α_o as shown in Fib. 3b for each of the positions A and D and the steady state amplitudes are measured at various velocities. Now, however, the motion is no longer in the Z direction but generally in a plane slightly inclined to it. The total tip amplitude W_T and the inclination of the plane of the motion with z direction denoted by γ , are plotted in Figs. 12a-f (position A) and 12g,h (position D) for various initial angles of attack position α_o and at different velocities. The sign convention for γ and α_o are as shown in inset diagram of Fig. 12a. They are both positive in the same sense. At position A, for velocities below 25 ft/sec, the steady state amplitudes are nearly symmetric for positive and negative α_o and goes down as α_o is increased (Fig. 12a). It goes down to zero in the vicinity of $\alpha_o = 10°$. At α_o beyond this the oscillations die out. The plane of oscillation is however somewhat irregular. At 17 ft/sec, the γ is in opposite sense to α_o. At 24 ft/sec the inclination γ are nearly zero. However beyond this velocity, there is a marked departure from this pattern as shown in Figs. 12c-f. The responses are no longer symmetric with respect to α_o and there is a large change in amplitude and inclination of plane of motion for a small change in α_o from -2.5° to +2.5°. The peak amplitudes occur in the vicinity of $\alpha_o = \pm 7.5°$ and goes through a minima near $\alpha_o = -2.5°$ (Figs. 12c,d). There is also considerable change in inclination of plane of oscillation γ. At small α_o, γ is in the same sense as α_o but bigger. Beyond $\alpha_o = \pm 7.5°$ as the amplitudes drop off, γ has the tendency of going down to zero again. As velocity is increased the response becomes more sensitive to α_o. At 65 ft/s (Figs. 12e,f) the amplitude has peaks at $\alpha_o = 2.5°$, $\pm 10°$ and drops off in between near $\alpha_o = \pm 5°$. Near $\alpha_o = \pm 10°$, the amplitude and inclination are rather large but drops off quickly as α_o increased a little farther. The same tests are carried out with the specimen in position D, at 37 and 45 ft/sec (Figs. 12g,h). The amplitude in this case shows the

regular trend as in Fig. 12a, with peak at $\alpha_o = 0$, dropping off as α_c is increased. Oscillation ceases near $\alpha_o = \pm 7^\circ$. The inclinations are nearly zero but show trends similar to those of Fig. 12a. Thus it can be observed that the drop off and rise of amplitude at $\alpha_o = 0$ for position A (Fig. 11a) is associated with large sensitivity of the response for small change in α_o in the vicinity $\alpha_o = 0$, whereas in the portion where the amplitude rises monotonically with increase in U, a small change in α_o from $\alpha_o = 0$ does not change the amplitude or inclination considrably. The amplitude drops off quickly as α_o is increased farther.

Fig. 13 shows some sample transient records for position A, $\alpha_o = 0$. They are plotted in sami-log paper on real time scale in Fig. 14. The initial logarithmic increment in amplitude is found to be linear. The experimental values of initial linear log (Slope)/ω_1 at different free stream velocity are plotted in Fig. 15 with a negative sign. According to quasi-static theory this is the experimental value of $g_1/2$, the linear theory - equivalent - damping coeficient as defined in Eq. 3.6.

All the experimental results described here have been found to be quite repeatable.

4.4 Theory and Experiment Comparison

Using the static aerodynamic force measurements it is now possible to calculate the response characteristics using the method described in Section 3, and compare with the experiment. When the beam is initially at zero angle of attack, the steady state amplitude at a given velocity is given by:

$$\frac{1}{\bar{u}}\left(\frac{\bar{a}}{\bar{u}}\right) - \left[P_1\left(\frac{\bar{a}}{\bar{u}}\right) + 1.761\, P_3\left(\frac{\bar{a}}{\bar{u}}\right)^3 + 4.17\, P_5\left(\frac{\bar{a}}{\bar{u}}\right)^5 + 11.32\, P_7\left(\frac{\bar{a}}{\bar{u}}\right)^7\right] = 0 \tag{4.3}$$

for a cantilever beam with the mode shape used and with a 8th degree polynomial fit of C_N versus tanß curve. Using the 8th degree polynomial fit of C_N versus tanß of

a) Fig. 7a, tested at 37 ft/sec in position A

b) Fig. 7b, tested at 37 ft/sec in position D

the steady state amplitudes $\bar{a}$ are plotted against $\bar{u}$ in Fig. 11b, along with the experimental values obtained for the specimen in position A and D at $\alpha_o = 0$. The value $\zeta_1 = .002$ $\tilde{\rho} = 0.35 \times 10^{-3}$ has been used. P_n are given in Table 2. It should be noted that $2(\bar{a}/\bar{u})$ represent the induced angle of attack β at the tip of the beam. Since the curve fitting is only up to $\tan\beta = 0.45$, results only up to $\bar{a}/\bar{u} = 0.225$ are valid. The results plotted are within this range. For a quick conversion from physical units to nondimensional values, the following relations may be used for $\tilde{\rho}/4\zeta_1 = 0.0438$

$$U\,(\text{FT/SEC}) \equiv 0.443\,u = 10.1\,\bar{u}$$

$$\frac{W_T}{b} \equiv 2a = 45.6\,\bar{a} \qquad (4.4)$$

Reasonably good agreement is observed for amplitudes up to $W_T/b = 15$. The experimental amplitude variation in position D shows similar trend but are substantially lower in magnitude. The quasi-static theory fails to predict the drop-off characteristics observed in position A and in general over estimates the steady state amplitude.

Another way of examining the applicability of quasi-static theory is to compare the initial transient growth rate when the amplitudes are small and equations are linear. To do this, the linear theory-equivalent-damping ratio $g_1/2 = \zeta_1 - 0.25\tilde{\rho}u P_1$, as defined in Eq. 3.6 is plotted in Fig. 15 and compared with experimental values. P_1 is the initial slope of C_N curve (Fig. 7a, U = 37F/S, Fig. 7b) and $\zeta_1 = .002$. They are of the same order of magnitude and trend but not close to linear with velocity as given by the theory. It may thus be concluded that the actual aerodynamic forces are more complex than a simple quasi-steady description. The static lift and drag values do not contain all the

information required to describe the dynamic forces induced by the motion. It is probable that as the amplitude increases beyond $W_T/b = 10$, the flow is no longer two dimensional and a break in the flow pattern at a part of the beam causes a flow change in the entire portion.

The amplitude response at different α_o can be compared with the theory in a qualitative basis since in the one degree of freedom case it has been observed that the quasi-steady theory cannot predict accurately the amplitude response when the amplitudes are large, but gives the right trend. So an approximate fit of C_N and C_C data has been chosen for comparison with the experiment (see Figs. 7, 8).

$$\left.\begin{aligned} C_N &= 0.9 \tan\beta - 8.0 \tan^3\beta \\ C_C &= 1.24 - 3.0 \tan^2\beta + 30.0 \tan^4\beta \end{aligned}\right\} \quad (\text{POS. A}, |\tan\beta| < 0.45)$$

$$\left.\begin{aligned} C_N &= 1.2 \tan\beta - 15.0 \tan^3\beta \\ C_C &= 1.1 - 3.0 \tan^2\beta + 30.0 \tan^4\beta \end{aligned}\right\} \quad (\text{POS. D}, |\tan\beta| < 0.4) \qquad (4.5)$$

After a steady state solution has been obtained at a given α_o from Eqs. 3.47, 3.48 one should check that $|\tan\beta|_{MAX} + |\tan\alpha_o|$ is less than the limits of curve fit (4.5), $|\tan\beta \tan\alpha_o|_{MAX} \leq 0.1$, $|\dot{V}/U| < 0.1$ in order that the solution be valid. The C_C curve fit is not very good, but it is observed that the subsequent value of Y does not affect the amplitudes substantially. The value of Y is however quite sensitive to C_C. The theoretical results are plotted in Fig. 12 in broken lines for comparison with experimental values. Results at velocity 17.9 ft/sec is not computed since the C_C data is not known. Amplitudes at velocities 24.5 and 37 ft/sec, position A (Figs. 12b,c) and 37 and 45 ft/sec, position D

(Fig. 12g,h) agree with the experiment qualitatively but the inclinations do not. It seems a simple quadratic C_C of Eq. 3.50 can explain qualitatively the experimental behavior at small α_o since it gives γ values proportional to α_o. At low velocities the dynamic C_C possibly increases with β which makes γ go in opposite sense to α_o. At higher velocity the dynamic C_C possibly goes down with β following the initial static trend (Fig. 8a) making Q_2 negative and γ goes up linearly with α_o for small α_o (Fig. 12c). Same explanation apply to Fig. 12h but not to 12g. Thus, the aerodynamic drag forces acting on the oscillating body seem to be rather complex and do not necessarily follow the static curve.

From these comparison it is observed that in two degrees of freedom, motion the quasi-static theory can give a qualitative description of the steady state amplitude response if it gives the right results in one degree of freedom case. The peculiar response obtained in position A (Fig. 12d, e, f) cannot be explained by introducing the two-dimensional motion.

From the experiment and quasi-static theory comparison it may be concluded that the self-excitation phenomena of a square section beam can be described qualitatively by the theory but usually results in overestimation. Physically the beam cannot achieve the high amplitudes predicted by theory without going into geometric nonlinearity but below the velocity 30 ft/sec ($\bar{u}$ = 3, Fig. 11b) it can. Up to W_T/b = 15 ($\bar{a}$ = 0.3) the flow is fairly two-dimensional and the amplitudes follow the quasi-static results fairly well. As the amplitude increases, the top portion of the beam moves in an arc which could be responsible for different flow patterns and lower amplitudes. On a bluff body with sharp edges where the flow is separated and the wake is turbulent, the aerodynamic forces are apparently quite complex and sensitive to imperfections and sharpness of the edges, and can give rise to unpredictable responses.

SECTION 5

SUSPENDED CABLE

5.1 Introduction

The galloping phenomena of overhead suspended power cables has been a subject of research for many years. The self-excitation is believed to be due to the negative damping characteristic of the cable cross section. However, unlike a cantilever beam the amplitudes can be limited by both

(a) Nonlinear aerodynamic force characteristics of the cross section.

(b) The tension developed in the beam due to large deflections.

To study this, galloping of a sagging cable of square cross section has been obtained experimentally in a wind tunnel and is described in Section 6. Theoretical means of describing the motion using quasi-static aerodynamic theory is discussed here. The motion is governed by two nonlinear partial differential equations which are reduced to nonlinear ordinary differential equations in time using Galerkin's approximation and are solved by harmonic balance method using only two equations. The theory-experiment comparison is discussed in Section 6.

5.2 Equations of Motion

Consider an uniform cable which is suspended between two poles with a particular sag and placed in a wind stream (Figs. 17a, b). With the wind off, the cable is in a catenary shape and the two ends are clamped in that position. The flexible cable is of square cross section and in the suspended position one of the flat sides face the wind stream. It is assumed that the cable can deflect in y and z direction without twisting (Fig. 17c) like the giant wheel riding boxes. Thus only two degrees of freedom need to be considered in the equilibrium

equations. Only small sags up to midspan sag/span ratio d/ℓ of 0.08 are considered. Thus the slopes at a deflected position are small and the simple beam equations are adequate to describe the cable motion. Also, for small sag it can be assumed that the tension in the cable is constant along its whole length and is thus independent of coordinate x. It can be shown using catenary equations that for a simply supported cable without bending rigidity and under constant self weight and drag forces along the span, the tension T_o at the support and at midspan are given by

$$\left(\frac{T_o}{mg\ell}\right)_{END} = \frac{\ell}{8d}\sqrt{1+(D_o/mg)^2}\left[1+4(d/\ell)^2\right]$$
$$\left(\frac{T_o}{mg\ell}\right)_{MID} = \frac{\ell}{8d}\sqrt{1+(D_o/mg)^2}\left[1+4(d/\ell)^2\right] \qquad (5.1)$$

Here m is the mass per unit length, ℓ is the span, d is the sag at midspan. D_o is the drag force per unit length. For d/ℓ<.080, the total variation of tension along the span is less than 5%. For a cable with small bending rigidity it is believed that the assumption of constant tension does not involve error more than this.

When the wind is turned on, at low velocity the cable leans back and takes up a stable static position until the critical velocity is reached. As the wind velocity is increased beyond the critical velocity, the oscillations grow until a stable limit cycle is reached. Thus to analyze the motion it is convenient to subtract out the static part from the overall equation

$$m\frac{\partial^2 W_t}{\partial t^2} - T_t\frac{\partial^2 W_t}{\partial x^2} + EI\frac{\partial^4 W_t}{\partial x^4} = mg + F_z\left(\frac{\partial W_t}{\partial t}, \frac{\partial V_t}{\partial t}, U\right)$$
$$m\frac{\partial^2 V_t}{\partial t^2} - T_t\frac{\partial^2 V_t}{\partial x^2} + EI\frac{\partial^4 V_t}{\partial x^4} = D_o + F_Y\left(\frac{\partial W_t}{\partial t}, \frac{\partial V_t}{\partial t}, U\right) \qquad (5.2)$$

Here F_z , F_Y represent the aerodynamic forces induced by the motion. All the static terms of aerodynamic forces are included in mg and D_o for static analysis. Subtracting the static equations

$$EI\frac{d^4W_o(x)}{dx^4} - T_o\frac{d^2W_o(x)}{dx^2} = mg$$

$$EI\frac{d^4V_o(x)}{dx^4} - T_o\frac{d^2V_o(x)}{dx^2} = D_o \tag{5.3}$$

from Eq. 5.2, one obtains

$$m\frac{\partial^2 W}{\partial t^2} + \left(EI\frac{\partial^4 W}{\partial x^4} - T_o\frac{\partial^2 W}{\partial x^2}\right) - T\frac{\partial^2(W+W_o)}{\partial x^2} = F_z\left(\frac{\partial W}{\partial t}, \frac{\partial V}{\partial t}, U\right)$$

$$m\frac{\partial^2 V}{\partial t^2} + \left(EI\frac{\partial^4 V}{\partial x^4} - T_o\frac{\partial^2 V}{\partial x^2}\right) - T\frac{\partial^2(V+V_o)}{\partial x^2} = F_Y\left(\frac{\partial W}{\partial t}, \frac{\partial V}{\partial t}, U\right) \tag{5.4}$$

where

$$W_t = W_o(x) + W(x,t)$$

$$V_t = V_o(x) + V(x,t)$$

$$T_t = T_o + T(t)$$

The $W_o(x)$, $V_o(x)$ satisfy the static equation (5.3) along with the boundary conditions

$$\text{AT} \quad \left.\begin{array}{l} X = 0 \\ = \end{array}\right\} \quad \begin{array}{l} W_o = 0 \\ \dfrac{dW_o}{dX} = \dfrac{dW_o}{dX} \\ V_o = 0 \\ \dfrac{dV_o}{dX} = 0 \end{array} \tag{5.5}$$

where $W_{oo}(x)$ is the deflection shape with the wind off, i.e.,

D_o=0. The double zero subscript will be used to refer to quantities when the free stream velocity U=0. The W and V satisfy clamped-clamped boundary conditions at both ends. The bending rigidity EI is assumed to be the same for both W and V displacements. The coupling between W and V arises from the aerodynamic and tension terms only. It is assumed that even after U exceeds the critical velocity, the static equations (5.3) are satisfied and give a measure of the mean position, i.e., the position if no motion induced forces were present. Since the tension is assumed to be independent of x, at a fixed time t, the tension T_t can be obtained by calculating the strain in the form

$$T_t = T_{oo} + \frac{AE}{\ell}\int_o^\ell (dS - d\mathcal{S}) \tag{5.6}$$

where

$$dS^2 = dx^2 + dW_t^2 + dV_t^2$$

$$d\mathcal{S}^2 = dx^2 + dW_{oo}^2$$

With the small slope assumption, this becomes

$$T_t = T_o + T(t) \tag{5.7}$$

where

$$T_o = T_{oo} + \frac{AE}{2\ell}\int_o^\ell \left[\left(\frac{dW_o}{dx}\right)^2 + \left(\frac{dV_o}{dx}\right)^2 - \left(\frac{dW_{oo}}{dx}\right)^2\right] dx$$

$$T_t = \frac{AE}{2\ell}\int_o^\ell \left[\left(\frac{\partial W}{\partial x}\right)^2 + \left(\frac{\partial V}{\partial x}\right)^2 + 2\frac{\partial W}{\partial x}\cdot\frac{dW_o}{dx} + 2\frac{\partial V}{\partial x}\cdot\frac{dV_o}{dx}\right] dx$$

This tension term is the source of nonlinearity in the cable vibration equation apart from the aerodynamic nonlinear terms. Both of these are responsible for limiting the amplitudes.

In quasi-static representation of aerodynamic forces it will be assumed that C_N and C_C are in the form

$$C_N = P_1 \tan\beta + P_3 \tan^3\beta$$
$$C_C = Q_0 \tag{5.8}$$

where

$$\tan\beta = \dot{W}/(U-\dot{V}) \qquad (\dot{}) = \frac{\partial(\,)}{\partial t}$$

It is possible to work out the problem with higher order polynomials for better representation of C_N and C_C but it would result in added complexity without adding better insight to the problem. Proceeding in the same manner as in Section 3.3 F_Z and F_Y can be written as

$$F_Z = \tfrac{1}{2}\rho U^2 b\left[P_1 \frac{\dot{W}}{U}\left(1-\underline{\frac{\dot{V}}{U}}\right) + P_3\left(\frac{\dot{W}}{U}\right)^3\left(1+\underline{\frac{\dot{V}}{U}}\right)\right]$$
$$F_Y = \tfrac{1}{2}\rho U^2 b\left[-2\frac{\dot{V}}{U} + \underline{\left(\frac{\dot{V}}{U}\right)^2}\right]Q_0 \tag{5.9}$$

for $|\dot{V}/U|<0.1$. Actual values of $\dot{V}/U$ are still smaller and it is possible to neglect the underlined terms within the present approximation.

5.3 Solution of Static Equations

The static equations (5.3) along with the boundary condition (5.5) can be solved exactly if T_o were known. In order to determine T_o it has to be expressed in terms of the displacements in the form (5.7). This makes Eq. 5.3 nonlinear and can only be solved approximately.

Solving Eq. 5.3 in terms of T_o with the boundary condition (5.5), one obtains

$$\frac{W_o}{d} = \frac{mgl}{2T_o}\frac{l}{d}\left[\xi(1-\xi) - \epsilon_o\left\{\frac{T_o}{T_{oo}}(1-e)-1\right\}\left\{\coth\frac{1}{2\epsilon_o}\left(\cosh\frac{\xi}{\epsilon_o}-1\right) - \sinh\frac{\xi}{\epsilon_o}\right\}\right]$$

$$\frac{V_o}{d} = \frac{D_o l}{2T_o}\frac{l}{d}\left[\xi(1-\xi) + \epsilon_o\left\{\coth\frac{1}{2\epsilon_o}\left(\cosh\frac{\xi}{\epsilon_o}-1\right) - \sinh\frac{\xi}{\epsilon_o}\right\}\right] \tag{5.10}$$

and

$$\frac{W_{oo}}{d} = \frac{mgl}{2T_o}\cdot\frac{l}{d}\left[\xi(1-\xi) + \epsilon_{oo}\, e\left\{\coth\frac{1}{2\epsilon_{oo}}\left(\cosh\frac{\xi}{\epsilon_{oo}} - 1\right) - \sinh\frac{\xi}{\epsilon_{oo}}\right\}\right]$$

where

$$\epsilon_o = \sqrt{EI/T_o l^2} \qquad \epsilon_{oo} = \sqrt{EI/T_{oo} l^2}$$

$$e = 2\epsilon_{oo}\tanh\frac{1}{\epsilon_{oo}} \qquad \xi = x/l$$

The double zero subscript refers to quantities when the wind is off. For these cables, $\epsilon_o < \epsilon_{oo} < 0.1$. Thus Using this approximation Eq. 5.10 simplifies to

$$\frac{W_o}{d} = \frac{mgl}{2T_o}\cdot\frac{l}{d}\left[\xi(1-\xi) - \epsilon_o\left\{\frac{T_o}{T_{oo}}(1-2\epsilon_o) - 1\right\}\left\{e^{-\frac{\xi}{\epsilon_o}} - 1\right\}\right]$$

$$\frac{V_o}{d} = \frac{D_o}{2T_o}\cdot\frac{l}{d}\left[\xi(1-\xi) + \epsilon_o\left\{e^{-\frac{\xi}{\epsilon_o}} - 1\right\}\right]$$

and

$$\frac{W_{oo}}{d} = \frac{mgl}{2T_o}\cdot\frac{l}{d}\left[\xi(1-\xi) + 2\epsilon_{oo}^2\left\{e^{-\frac{\xi}{\epsilon_o}} - 1\right\}\right] \qquad (5.11)$$

The above is valid for $0<\xi<.5$, and the functions are assumed symmetric on the other half of the span. Now initial tension T_{oo} can be determined by setting $W_{oo}=d$ at $\xi=0.5$ and then solving for T_{oo} with the above approximation, to get

$$\frac{T_{oo}}{mgl} = \frac{l}{8d}\left[1 - 64\,\frac{EI}{mgl^3}\cdot\frac{d}{l}\right] \qquad (5.12)$$

The effect of bending rigidity is to reduce the tension from the average 'Catenary analysis' value of $mgl^2/8d$. In the present case $EI/mgl^3=0.01$, so the correction is of the same order as the approximation involved in the analysis. Now the static tension T_o at a particular velocity U can be determined by substituting Eqs. 5.11 in the expression for T_o in Eq. 5.7 and

carrying out the integration. A nonlinear algebraic equation in T_o/T_{oo} is obtained which can be solved by iteration. Substituting them back in Eq. 5.11 would give the static deflection shapes $W_o(\xi)$, $V_o(\xi)$.

The variation of T_o/T_{oo} with wind velocity U is in general as shown in Fig. 19. For a simply-supported cable with no bending rigidity the problem is statically determinate and can be solved exactly using the 'Catenary equations' to give

$$\frac{T_o}{T_{oo}} = \left[1 + (D_o/mg)^2 \right]^{\frac{1}{2}} \tag{5.13}$$

This is compared with the present results in Fig. 19 and is found to give higher values. Using Eq. 5.11 one can obtain the static positions at different velocity. One such plot for $d/\ell=0.059$, $C_D=1.4$ is shown in Fig. 20. For a simply-supported cable the static positions are given by straight lines inclined to the vertical at an angle $\tan^{-1}(D/mg)$. The inclinations are found to be close to the present case but the static positions are not.

5.4 Harmonic balance solution

Using Galerkin's approximation Eq. 5.4 is reduced to ordinary differential equations in time assuming W and V in the form

$$\begin{aligned} W &= d \left\{ f_1(\xi) q_{f_1}(t) + f_2(\xi) q_{f_2}(t) \right\} \\ V &= d \left\{ f_1(\xi) \tilde{q}_{f_1}(t) + f_2(\xi) \tilde{q}_{f_2}(t) \right\} \\ W_o &= d\, f_o(\xi) \\ V_o &= d\, \tilde{f}_o(\xi) \end{aligned} \tag{5.14}$$

Here $f_1(\xi)$, $f_2(\xi)$ are first and second bending mode shape of a freely vibrating clamp-clamped beam and are given in Appendix D. $f_o(\xi)$, $\tilde{f}_o(\xi)$ are static deflection shapes given by Eq. 5.11. It may be noted that $f_1(\xi)$, $f_o(\xi)$, $\tilde{f}_o(\xi)$ are symmetric functions about midspan while $f_2(\xi)$ is an anti-symmetric function. Under the existing forces the four modes are sufficient to describe the motion. Hore (Ref. 31) have analyzed the free vibration of a similar flexible sagging cable using the present mode shapes and have obtained good theory-experiment agreement.

In nondimensional form, the ordinary differential equations can be expressed as

$$\ddot{q}_{b1} + r_1^2 q_{b1} + \alpha_1 \bar{T}(q_{b1} + q_{bo}) = \tfrac{1}{2}\rho u^2 \left[\frac{P_1}{u} \dot{q}_{b1} + \frac{P_3}{u^3}\left(A_{40} \dot{q}_{b1}^3 + 3 A_{22} \dot{q}_{b1} \dot{q}_{b2}^2 \right) \right]$$

$$\ddot{\tilde{q}}_{b1} + r_1^2 \tilde{q}_{b1} + \alpha_1 \bar{T}(\tilde{q}_{b1} + \tilde{q}_{bo}) = \tfrac{1}{2}\rho u^2 \left[-2 \frac{Q_o}{u} \dot{\tilde{q}}_{b1} \right]$$

$$\ddot{q}_{b2} + r_2^2 q_{b2} + \alpha_2 \bar{T} q_{b2} = \tfrac{1}{2}\rho u^2 \left[\frac{P_1}{u} \dot{q}_{b2} + \frac{P_3}{u^3}\left(A_{04}' \dot{q}_{b2}^3 + 3 A_{22}' \dot{q}_{b1}^2 q_{b2} \right) \right]$$

$$\ddot{\tilde{q}}_{b2} + r_2^2 \tilde{q}_{b2} + \alpha_2 \bar{T} \tilde{q}_{b2} = \tfrac{1}{2}\rho u^2 \left[-\frac{2Q_o}{u} \dot{\tilde{q}}_{b2} \right]$$

(5.15a,b,c,d)

where $\omega_R t = \tau$ $\qquad (\dot{}) = \frac{d(\,)}{d\tau}$

$$\bar{T} = \left[q_{b1}^2 + \tilde{q}_{b1}^2 + \beta_r (q_{b2}^2 + \tilde{q}_{b2}^2) + 2 q_{b1} q_{bo} + 2 \tilde{q}_{b1} \tilde{q}_{bo} \right]$$

$$r_1^2 = \left[\frac{EI}{m l^4} D_1 + \frac{T_o}{m l^2} B_1 \right] / A_{20} \omega_R^2$$

$$r_2^2 = \left[\frac{EI}{m l^4} D_2 + \frac{T_o}{m l^2} B_2 \right] / A_{02} \omega_R^2$$

$$\tilde{\rho} = \frac{\rho b^2}{m} \cdot \frac{d}{b}$$

$$u = \frac{U}{b\omega_R} \cdot \frac{b}{d}$$

$$\alpha_1 = \frac{AE}{2ml^2}\left(\frac{d}{l}\right)^2 \cdot \frac{B_{11}^2}{A_{20}} \frac{1}{\omega_R^2}$$

$$\alpha_2 = \alpha_1 \frac{B_{22}}{A_{02}} \cdot \frac{A_{20}}{B_{11}}$$

The time is nondimensional with some reference frequency ω_R. The definition of $\tilde{\rho}$, u are slightly different than those used in Section 3. A_{mn}, B_{11}, B_{22}, D_1, D_2, β_r are constants and are given in Appendix D. q_o, $\tilde{q}_o$ are a measure of static position of the cable. They vary with velocity as shown in Fig. 21. Their definition are also given in Appendix D. It may be noted that r_1, r_2 also vary with velocity.

So far no structural damping terms have been included. There is a certain amount of uncertainty in its actual values. Experimentally with the wind off the cable can be given small tapping in first or second horizontal bending mode and the amplitude decay recorded. The slope of the transient amplitude plotted against time in a semi-log paper is found to be linear. From this viscous damping coefficients $\tilde{c}_1$, $\tilde{c}_2$ can be evaluated. Assuming $c_1=\tilde{c}_1$, $c_2=\tilde{c}_2$ the structural damping can be expressed as a viscous damping for theoretical convenience by adding the terms $(c_1/m\omega_R)\dot{q}_{g1}$, $(\tilde{c}_1/m\omega_R)\dot{\tilde{q}}_{g1}$, $(c_2/m\omega_R)\dot{q}_{g2}$ etc. to Eqs. 5.15. However, with the wind on, the cable will oscillate at a higher frequency and it is not known how much is the actual structural damping then. To overcome this difficulty c_1, $\tilde{c}_1$ etc. can later be set to zero and the resulting change in responses compared since the structural damping are usually

small. Let us denote

$$c_1/m\omega_R = 2\zeta_1 \qquad \tilde{c}_1/m\omega_R = 2\tilde{\zeta}_1$$
$$c_2/m\omega_R = 2\zeta_2 \qquad \tilde{c}_2/m\omega_R = 2\tilde{\zeta}_2 \tag{5.16}$$

Let us first examine the linear equations

$$\begin{aligned}
&\ddot{q}_{b1} + g_1\dot{q}_{b1} + \Omega_1^2 q_{b1} + \Lambda\tilde{q}_{b1} = 0\\
&\ddot{\tilde{q}}_{b1} + \tilde{g}_1\dot{\tilde{q}}_{b1} + \Lambda q_{b1} + \tilde{\Omega}_1^2\tilde{q}_{b1} = 0\\
&\ddot{q}_{b2} + g_2\dot{q}_{b2} + r_2^2 q_{b2} = 0\\
&\ddot{\tilde{q}}_{b2} + \tilde{g}_2\dot{q}_{b2} + r_2^2\tilde{q}_{b2} = 0
\end{aligned} \tag{5.17a,b,c,d}$$

where

$$\Omega_1^2 = r_1^2 + 2\alpha_1 q_{b0}^2 \qquad \tilde{\Omega}_1^2 = r_1^2 + 2\alpha_1\tilde{q}_{b0}^2$$

$$\Lambda = 2\alpha_1 q_{b0}\tilde{q}_{b0}$$

$$g_1 = 2\zeta_1 - \tfrac{1}{2}\tilde{\rho}uP_1 \qquad \tilde{g}_1 = 2\tilde{\zeta}_1 + \tilde{\rho}uQ_0$$

$$g_2 = 2\zeta_2 - \tfrac{1}{2}\tilde{\rho}uP_1 \qquad \tilde{g}_2 = 2\tilde{\zeta}_2 + \tilde{\rho}uQ_0$$

The first and second mode equations decouple. The stiffness matrix of (5.17 a,b) is symmetric and positive definite. So the instability can only arise from negative damping terms g_1 and g_2.

Considering Eq. (5.17 a,b), the critical velocity and the frequency of oscillation at the critical velocity can be

determined in the usual manner by introducing $q_{b_1} = a_1 e^{i\omega\tau}$, $\tilde{q}_{b_1} = \tilde{a}_1 e^{i\omega\tau}$ and setting the condition of condition of existence of non-trivial solution of the resulting homogeneous algebraic equations. This gives

$$\omega_F^2 = \frac{\Omega_1^2 \tilde{g}_1 + \tilde{\Omega}_1^2 g_1}{g_1 + \tilde{g}} \tag{5.19}$$

at a velocity which makes

$$4\alpha_1^2 q_{b_0}^2 \tilde{q}_{b_0}^2 + g_1 \tilde{g}_1 \left[\left(\frac{\Omega_1^2 - \tilde{\Omega}_1^2}{g_1 + \tilde{g}_1} \right)^2 + \frac{\Omega_1^2 \tilde{g}_1 + \tilde{\Omega}_1^2 g_1}{g_1 + \tilde{g}_1} \right] = 0 \tag{5.20}$$

Since Ω_1, $\tilde{\Omega}_1$, q_{b_0}, $\tilde{q}_{b_0}$ are functions of velocity (Fig. 21), no explicit expression for critical velocity can be obtained, and ω_F, u_c has to be determined by plotting (5.20) for various u until it becomes zero. Corresponding ω_F will give the flutter frequency.

The Eq. (5.17 c,d) are uncoupled from each other. The critical velocity for q_{b_2} mode will be given by $g_2=0$. The flutter frequency is r_2. Since $\tilde{g}_2$ is positive at all velocity $\tilde{q}_{b_2}$ will die out.

For the solution of entire non-linear equation let us take only Eqs. 5.15 a,b assuming no second mode is present. The equation has quadratic and cubic nonlinear terms in q_{b_1} and $\tilde{q}_{b_1}$.

$$\begin{aligned}
&\ddot{q}_{b_1} + g_1 \dot{q}_{b_1} - \tfrac{1}{2}\tilde{\rho} u^2 P_3 A_{30} \left(\frac{\dot{q}_{b_1}}{u} \right)^3 + \Omega_1^2 q_{b_1} + \Lambda \tilde{q}_{b_1} \\
&\quad + \alpha_1 \left(3 q_{b_0} q_{b_1}^2 + 2 \tilde{q}_{b_0} q_{b_1} \tilde{q}_{b_1} + q_{b_0} \tilde{q}_{b_1}^2 \right) + \alpha_1 q_{b_1} \left(q_{b_1}^2 + \tilde{q}_{b_1}^2 \right) = 0 \\
&\ddot{\tilde{q}}_{b_1} + \tilde{g}_1 \dot{\tilde{q}}_{b_1} + \Lambda q_{b_1} + \tilde{\Omega}_1^2 \tilde{q}_{b_1} \\
&\quad + \alpha_1 \left(3 \tilde{q}_{b_0} \tilde{q}_{b_1}^2 + 2 q_{b_0} q_{b_1} \tilde{q}_{b_1} + \tilde{q}_{b_0} q_{b_1}^2 \right) + \alpha_1 \tilde{q}_{b_1} \left(q_{b_1}^2 + \tilde{q}_{b_1}^2 \right) = 0
\end{aligned} \tag{5.21}$$

The reference frequency ω_R is chosen equal to the linear first mode natural frequency at u=0, i.e.

$$\omega_R = \omega_{o1} = \left\{ \frac{1}{A_{20}} \left[\frac{EI}{ml^4} D_1 + \frac{T_{oo}}{ml^2} B_{11} \right] \right\}^{1/2} \tag{5.22}$$

So at u=0 r_1=1 in Eq. 5.15.

To get an idea of the nature of the solution of Eq. 5.21 is first integrated numerically using predictor corrector scheme with an error bound 10^{-4}. Some results are shown in Fig. 25. For small initial displacements the amplitudes grow initially then settle down to a steady state amplitude. An estimation of induced angle of attack shows that the induced angle of attack β is well within the linear range of C_N, according to the quasi-static theory. Thus to evaluate the steady state amplitude by harmonic balance it is sufficient to assume (Ref. 39)

$$\begin{aligned} q_1 &= b_o + b_1 \cos\omega\tau + a_1 \sin\omega\tau + b_2 \cos 2\omega\tau + a_2 \sin 2\omega\tau \\ \tilde{q}_{\beta 1} &= \tilde{b}_o + \tilde{b}_1 \cos\omega\tau + \tilde{a}_1 \sin\omega\tau + \tilde{b}_2 \cos 2\omega\tau + \tilde{a}_2 \sin 2\omega\tau \end{aligned} \tag{5.23}$$

ω is the nondimensional frequency with respect to ω_R. Substituting (5.23) in Eq. (5.21), keeping only the $\cos\omega\tau$, $\sin\omega\tau$, $\cos 2\omega\tau$, $\sin 2\omega\tau$ terms and setting their coefficients and the constant terms to zero one obtains 10 nonlinear algebraic equations in 12 unknowns b_o, $b_1 \ldots \tilde{a}_2$ and ω,u. Since in steady state solution absolute phase is unimportant, $\tilde{a}_1$ is set to zero and equations are solved by Newton-Raphson iteration procedure for the 10 unknowns ω, b_o, $b_1 \ldots \tilde{b}_1$, $\tilde{b}_2$, $\tilde{a}_2$ at a given u. The algebraic equations and details of iteration procedure are given in Appendix E. Some of the solutions are shown in Fig. 24 and are discussed in Section 6.3. The solution of the form (5.23) represents large swinging motion of the cable. Since the cable swings way up above the X-Y plane (Fig. 17 b,c),

$\cos 2\omega\tau$ terms come in for representing the motion in the q_1, $\tilde{q}_1$ cartesian coordinate. From the polar coordinate point of view the frequency of oscillation of the physical cable is ω.

Assuming the quasi-static representation of the motion induced lift forces are correct, theoretically the amplitude is limited by the tension together with the $\tilde{g}_2$ damping term which becomes important when the cable moves against the wind stream at the end of the large swinging motion.

SECTION 6

EXPERIMENT WITH SUSPENDED CABLE

6.1 Introduction

To analyze the galloping phenomena of suspended power cable, tests are first conducted with a uniform sagging cable of square cross-section in a wind tunnel. The cable is flexible but with a definite but small bending rigidity. Large and rather violent self-excited oscillations are observed. When a cable of circular cross-section is placed in the wind tunnel no such self-excitation is obtained. Thus the galloping phenomena is found to be due to negative damping type aerodynamic forces typically associated with bluff bodies with sharp edges. The cable begins to oscillate by itself beyond a certain critical velocity but finally settles down to a steady state amplitude. The experiments are conducted with different sag/span ratios of d/ℓ = 0.080, 0.059, 0.043, 0.029, 0.020 and 0.011 and the results are described in Section 6.2. Theoretical solutions using simple quasi-static theory are compared with the experimental results in Section 6.3.

6.2 Description of Experimental Results

The experiment is conducted in a 5 ft x 7 ft closed circuit low-speed wind tunnel. The specimen is made from a 0.045 inch diameter flexible cable. It is coated with wax and drawn through a template with a square hole to give it a 0.09 inch square section outside. Care is taken to avoid twisting of the cable during the drawing process. Because of this construction procedure the uniformity is not perfect and the edges are somewhat rounded. The extension rigidity EA of the bare cable has been measured by Hore (Ref. 31) and is used here assuming that the wax coating does not affect it appreciably. The bending rigidity EI is determined by measuring the tip deflection due to self-weight of a portion of the

cable cantilevered at one end and using the linear force deflection relation $EI = mgl_c^4/8\delta$ where δ is the measured tip deflection. There is certain amount of scatter and the mean value is taken. The numerical values of the cable parameters are given in Table 3.

The cable is suspended in the wind tunnel from two rigid 1.5 feet long 0.75 inch diameter poles fixed to the floor of the tunnel (Fig. 17a). The cable is suspended at a particular sag and is clamped at two ends in such a manner that the cable assumes a natural catenary shape and one of the sides of the square faces the wind stream. Because of flexibility and clamped edge condition the cable can deflect in Y and Z directions (Figs. 17b,c) without any apparent rotation like the riding boxes of a giant wheel. The posts are long enough so that the entire cable is outside the wind tunnel boundary layer. There is some interference at the ends because of the clamps and the posts. At the beginning of a test run at a particular sag, the first horizontal mode natural frequency of the cable is measured by slightly tapping the cable. This frequency gives the experimental value of linear first mode natural frequency at U = 0 as given in Eq. 5.22 and is denoted by ω_{o1}.

At several different sag positions decay records for small horizontal oscillations are obtained using a small strain gage at one end of the cable. The strain gage signals for small mid-span deflections are linear. From the slope of the transient amplitude plotted against time on semi-log paper, the critical damping ratio $\tilde{\zeta}_1 = \tilde{c}_1/2m\omega_{o1}$ can be obtained as a function of amplitude. The $\tilde{\zeta}_1$ is found to be constant for small amplitudes. Some $\tilde{\zeta}_1$ values measured at different d/ℓ are shown in Fig. 18 along with a typical record. At d/ℓ = 0.059 a second mode damping ratio is measured and is found to be $\tilde{\zeta}_2 = 0.018$.

When the wind is turned on, at low velocities, the cable bends back and assumes an inclined static equilibrium position. Any disturbance imparted on it quickly dies down. An eye estimation of the cable inclination is made from outside the wind tunnel using a transparent protractor fixed to one of the clamped ends. This is shown in Fig. 20, for $d/\ell = 0.059$. For other sag ratios the same type of variation is observed with little scatter. The solid lines give the theoretical values calculated from Eq. 5.11 which will be discussed later. The wind velocity is increased in small steps and beyond a certain critical velocity, the cable begins to oscillate by itself. The amplitude increases until a steady state value is reached. The mid-span amplitude is measured by a vertically travelling telescope from outside the tunnel by focussing near the midspan and freezing the motion of the cable by a strobe light which is also used for measuring the frequency. The velocity is increased in small steps to about 100 ft/sec and then decreased. The frequency and midspan amplitudes are estimated at each velocity, and are shown plotted in Fig. 22a,b.

At low velocities, the cable first begins to oscillate in second bending mode with the cable at blown back position. As velocity is increased, it begins to oscillate in first bending mode in a swinging motion. At a higher velocity, the second mode appears again. The cable oscillates primarily in the first mode with small second mode superimposed, giving the appearance of a travelling wave across the span. A brief outline of the response description is given in Table 4. At mode transition points and when both the modes occur together, the second mode has approximately twice the frequency of the first mode.

It is observed that the frequencies measured with velocity increasing and decreasing, follow the same path but the amplitude measurements show a certain amount of hysteresis. The arrows in Fig. 22a show the path with velocity increasing. The first mode

frequencies, nondimensioned by ω_{o1} and the amplitudes nondimensioned by sag d are plotted in Fig. 23. For d/ℓ = 0.080, 0.059, 0.043, 0.059, 0.043, 0.029 the nondimensioned frequencies seem to collapse into a single line and increase almost linearly with velocity. As for the amplitudes there is no general pattern. For d/ℓ = 0.059 the amplitude is quite large and cable swings in an almost 180° arc with a near horizontal mean position. For higher d/ℓ = 0.080 the amplitudes are lower but still quite large. With reappearance of small second mode near 70 ft/sec, the amplitudes tend to go down. For lower d/ℓ = 0.043 the amplitude response is similar. With reappearance of strong second mode near 90 ft/sec the amplitudes go down rapidly. At very low d/ℓ = 0.020, 0.011 the amplitudes are quite large compared to the sag and increase rapidly with velocity.

These are two possible reasons for the irregular amplitude responses at different sag ratios. As seen in Section 4, the aerodynamic forces are quite sensitive to small imperfections at the edges of the cable and since no specific side of the square was chosen to face the wind, two different sides facing the wind at two different sag can give unexpected different results. Secondly, since the cable is not entirely free from small initial twist at the clamped ends, it can affect the amplitudes to a certain extent.

6.3 Theory and Experiment Comparison

The static aerodynamic force data measured for the square section cantilever beam and described in Section 3 can be used for the cable since both are of same cross-section shape and the experiments are in the same Reynolds number range. For numerical calculation an average representation of C_N and C_C has been used.

$$C_N = 1.0 \tan\beta - 10.0 \tan^3\beta$$

$$C_C = 1.4 \qquad (6.1)$$

For different values of P_1 and Q_o in the range obtained in the test, the solutions given by Eq. 5.21 changes slightly but the nature of the solution remains unchanged.

To check the static representation of the cable one can compare the linear first natural frequency at zero velocity given by Eq. 5.22. This is simply the frequency of small horizontal oscillation of the sagging cable.

d/ℓ	ω_{o1} (Theory)	ω_{o1} (Expt.)
0.080	2.5	2.5
0.059	2.86	2.8
0.043	3.3	3.3
0.029	3.9	4.0
0.020	5.2	4.6
0.011	6.1	5.5

They are found to be in good agreement except at small sag ratios.

The static positions at different velocities are computed from Eq. 5.11 and plotted in Fig. 20 for $d/\ell = 0.059$. The top picture shows the side view of the cable position, and these are similar to those observed during the experiment. The inclination of the cable from the vertical is also shown in the lower picture and is found to compare well with the experimental observations. For other d/ℓ ratios the results are found to be similar.

The steady state amplitudes are calculated from Eqs. 5.21 by harmonic balance method, assuming no second bending mode is present. The results for $d/\ell = 0.059$, 0.043 are shown in Figs. 24a,b. An estimation of maximum induced angle of attack from the frequency and amplitude shows that it is well within the linear C_N range. Since the structural damping is not truly represented by the critical damping ratios ζ_1, $\tilde{\zeta}_1$ the solutions with ζ_1, $\tilde{\zeta}_1 = 0$ are also shown in Fig. 24a. Exclusion of structural damping does not change the amplitude substantially except near the critical velocity. The frequencies agree quite well with the experimental values. The amplitudes are only in qualitative agreement for these two sag ratios. Theoretical results for

other sag ratios give frequencies which are close to the experimental values and the amplitudes follow the same theoretical trend as for $d/\ell = 0.059$ and are in disagreement with the experimental values except for the similar trend of large increases in amplitude near the critical velocity. From the experimental results it is observed that the aerodynamic lift forces do not reach the values given by the quasi-static theory due to the lack of spanwise correlation.

SECTION 7

CONCLUSIONS

The present report has investigated the self-excitation characteristics of a square section body in the form of a vertical cantilever beam and a sagging suspended cable when placed in an uniform wind stream. The self-excitation is due to negative damping type aerodynamic forces induced by transverse motion of the body. Unlike the vortex excited oscillation, this kind of self-excitation can take place over a wide range of velocity, independent of the natural frequency of the body.

Since no purely theoretical method of predicting the aerodynamic forces on a bluff body with turbulent wake exists, experimental quasi-static representation of aerodynamic forces was used to determine the responses theoretically. They were compared with experiment to examine their applicability for large three dimensional displacements.

Experiments were conducted with a square-section flexible cantilever beam, free to deflect in any direction without twisting, and placed at various initial angles of attack. The static aerodynamic forces were measured for use in the quasi-static theory. The dynamic responses and transient motions were recorded. The steady state amplitude in general increases monotonically with the wind velocity but in certain cases the amplitude drops off over a range of velocity (Fig. 11a). In these cases the response was found to be very sensitive to small changes in initial angle of attack α_o (Fig. 12). The linear equations give unbounded solution beyond a certain critical velocity and the amplitude of oscillation is limited by nonlinear aerodynamic forces. The theoretical solution for the steady state amplitude agreed only qualitatively with experiment, generally overestimating the values and failing to predict the peculiar amplitude drop-off behavior

(Figs. 11a,b). When the beam was at an initial angle of attack α_o the agreement was again qualitative (Figs. 12b,c,g,h). The discrepancies were probably due to imperfections of the beam, unsteady aerodynamic forces and Reynolds number effects.

Experiments were also conducted with a square section, sagging suspended cable. Large self-excited oscillations were observed and the amplitude and frequency of steady state oscillations were recorded (Fig. 22). The frequency response showed a regular trend but the steady state amplitude values varied widely with different sag of the cable. In the equations of motion, the tension in the cable as well as aerodynamic forces contribute to the nonlinearity and can affect the steady state amplitude. In the first mode oscillations, the motion remained in the linear range of aerodynamic forces and the amplitude was limited by the tension forces together with the damping forces due to the drag. Reasonably good agreement between theory and experiment was obtained for the frequencies, but the steady state amplitudes were in qualitative agreement only for two particular sags (Figs. 24a,b). Again, these discrepancies were probably due to imperfections of the cable, unsteady aerodynamic forces and Reynolds number effects.

Thus, the aerodynamic forces acting on an oscillating bluff body with sharp edges were found to be rather complex and quite sensitive to small imperfections and sharpness of the edges, giving rise to unexpected responses. The actual motion induced forces do not reach the values given by quasi-static theory due to imperfections, lack of spanwise correlation and unsteady aerodynamic effects.

The results obtained here may be of interest in understanding the wind induced oscillations of tall towers, buildings, launch vehicles on the ground and power lines. To understand thoroughly the unsteady aerodynamic forces acting on bluff bodies with sharp edges, more dynamic tests need to be conducted.

APPENDIX A

CANTILEVER MODE SHAPE

The first bending mode shape of the uniform cantilever beam $f_1(\xi)$ of Eqs. 3.2 and 3.19 is chosen so as to satisfy the free vibration equation and all the boundary conditions (Ref. 30).

$$f_n(\xi) = \cosh \varepsilon_n \xi - \cos \varepsilon_n \xi - \alpha_n (\sinh \varepsilon_n \xi - \sin \varepsilon_n \xi)$$

For first mode $\varepsilon_1 = 1.8751$, $\alpha_1 = 0.7341$ & $f_1(1) = 2$

The integral $A_n = \frac{1}{A_1} \int_0^1 \left[f_1(\xi) \right]^{n+1} d\xi$ are evaluated numerically using Waddel's rule of integration.

$$A_1 = \int_0^1 \left[f_1(\xi) \right]^2 d\xi = 1$$

$A_2 = 1.478$

$A_3 = 2.348$

$A_5 = 6.673$

$A_7 = 20.71$

$A_9 = 67.73$

$$B_1 = \int_0^1 \left(\frac{df_1}{d\xi} \right)^2 d\xi = 4.648$$

$$D_1 = \int_0^1 \left(\frac{d^2 f_1}{d\xi^2} \right)^2 d\xi = 12.362$$

APPENDIX B

HARMONIC BALANCE COEFFICIENTS (FOR CANTILEVER BEAM)

The functions $f_{s1}(a_1, b_1, a_2, b_2)$ etc. are obtained from the integrals

$$f_{s1}(a_1, b_1, a_2, b_2) = \frac{1}{\pi}\int_{-\pi}^{\pi} \sum_{m=3} \sum_{n=0} \frac{\tilde{Z}_{mn}}{u^{m+n}} (-b_1 \sin\tau + a_1 \cos\tau)^m \times (-b_2 \sin\tau + a_2 \cos\tau)^n \sin\tau \, d\tau$$

$$f_{c1}(a_1, b_1, a_2, b_2) = \frac{1}{\pi}\int_{-\pi}^{\pi} \sum_{m=3} \sum_{n=0} \frac{\tilde{Z}_{mn}}{u^{m+n}} (-b_1 \sin\tau + a_1 \cos\tau)^m \times (-b_2 \sin\tau + a_2 \cos\tau)^n \cos\tau \, d\tau$$

and similarly for $f_{s2}(a_1, b_1, a_2, b_2)$ and $f_{c2}(a_1, b_1, a_2, b_2)$ by replacing $\tilde{Z}_{mn}$ by $\tilde{Y}_{mn}$.

If $b_1 = 0$ it is possible to get a general expression for these integrals as given below.

Case I $(m + n)$ even

$$f_{s1}(a_1, 0, a_2, b_2) = 0$$

$$f_{c1}(a_1, 0, a_2, b_2) = 0$$

Case II m even, n odd

$$f_{s1}(a_1, 0, a_2, b_2) = \sum_{m=4,6\cdots} \sum_{n=1,3\cdots} \frac{\tilde{Z}_{mn}}{u^{m+n}} (a_1)^m \sum_{r=0,2,4\cdots}^{n-1} {}^nC_r (-b_2)^{n-r} (a_2)^r G_{mnr}$$

$$f_{c1}(a_1, 0, a_2, b_2) = \sum_{m=4,6\cdots} \sum_{n=1,3\cdots} \frac{\tilde{Z}_{mn}}{u^{m+n}} (a_1)^m \sum_{r=0,2,4\cdots}^{n-1} {}^nC_r (a_2)^{n-r} (-b_2)^r H_{mnr}$$

Case III m odd, n even

$$f_{s1}(a_1, 0, a_2, b_2) = \sum_{m=3,5\cdots} \sum_{n=2,4\cdots} \frac{\tilde{Z}_{mn}}{u^{m+n}} (a_1)^m \sum_{r=1,3,5}^{n-1} {}^nC_r (-b_2)^{n-r} (a_2)^r G_{mnr}$$

$$f_{c1}(a_1, 0, a_2, b_2) = \sum_{m=3,5\cdots} \sum_{n=2,4\cdots} \frac{\tilde{Z}_{mn}}{u^{m+n}} (a_1)^m \sum_{r=0,2,4\cdots}^{n} {}^nC_r (a_2)^{n-r} (-b_2)^r H_{mnr}$$

where

$${}^nC_r = {}^nC_{n-r} = \frac{n!}{r!\,(n-r)!}$$

$$G_{mnr} = 2 \cdot \frac{[(m+r-1)(m+r-3)\cdots 3.1][(n-r)(n-r-2)\cdots 3.1]}{[(m+n+1)(m+n-1)(m+n-3)\cdots \cdots 4.2]}$$

$$H_{mnr} = 2.\frac{[k(k-2)(k-4)\cdots 3.1][(r-1)(r-3)\cdots 3.1]}{[(m+n+1)(m+n-1)(m+n-3)\cdots 4.2]}$$

Here $k = m+n-r$

If any factorial or first bracketed term are negative, they are set equal to unity. Also $0! = 1$.

$f_{s2}(a_1, o, a_2, b_2)$, $f_{c2}(a_1, o, a_2, b_2)$ are given by the same expression after replacing $\tilde{Z}_{mn}$ by $\tilde{Y}_{mn}$.

APPENDIX C

FORCE COEFFICIENTS

The quantities $Z_0, Z_1, \cdots Z_5$, $Y_0, Y_1, \cdots Y_5$ used in Eq. 3.46 are defined as below for $|\tan\beta \tan\alpha_0| \leq 0.1$

Let $\tilde{P}_n = (P_n - Q_n \tan\alpha_0) \cos^3\alpha_0$

$\tilde{Q}_n = (Q_n + P_n \tan\alpha_0) \cos^3\alpha_0$

$$Z_0 = [\tilde{P}_0 - \tilde{P}_1 \tan\alpha_0 + \tilde{P}_2 \tan^2\alpha_0 - \tilde{P}_3 \tan^3\alpha_0 + \tilde{P}_4 \tan^4\alpha_0]$$

$$Z_1 = [2(\tilde{P}_0 - \tilde{P}_2)\tan\alpha_0 + \tilde{P}_1(1 - \tan^2\alpha_0) + \tilde{P}_3(3\tan^2\alpha_0 + \tan^4\alpha_0) - \tilde{P}_4(4\tan^3\alpha_0 + 2\tan^5\alpha_0)]$$

$$Z_2 = [\tilde{P}_0 \tan^2\alpha_0 + \tilde{P}_1 \tan\alpha_0 + \tilde{P}_2 - 3\tilde{P}_3(\tan\alpha_0 + \tan^3\alpha_0) + \tilde{P}_4(6\tan^2\alpha_0 + 8\tan^4\alpha_0)]$$

$$Z_3 = [\tilde{P}_3(1 + 3\tan^2\alpha_0) - \tilde{P}_4(4\tan\alpha_0 + 12\tan^3\alpha_0)]$$

$$Z_4 = [-\tilde{P}_3 \tan\alpha_0 + \tilde{P}_4(1 + 8\tan^2\alpha_0)]$$

$$Z_5 = [-\tilde{P}_4(2\tan\alpha_0)]$$

$Y_0, Y_1, \cdots Y_5$ are same as above if $\tilde{P}_0, \tilde{P}_1 \cdots \tilde{P}_4$ are replaced by $\tilde{Q}_0, \tilde{Q}_1, \cdots \tilde{Q}_4$.

APPENDIX D

CABLE MODE SHAPE

The mode shape $f_1(\xi)$, $f_2(\xi)$ used in Eq.(5.14) are the first and second bending mode shapes of a freely vibrating clamped-clamped beam (Ref. 30).

$$f_1(\xi) = \frac{1}{1.588}\left[\cosh\varepsilon_1\xi - \cos\varepsilon_1\xi - \alpha_1(\sinh\varepsilon_1\xi - \sin\varepsilon_1\xi)\right]$$

$$f_2(\xi) = \left[\cosh\varepsilon_2\xi - \cos\varepsilon_2\xi - \alpha_2(\sinh\varepsilon_2\xi - \sin\varepsilon_2\xi)\right]$$

$\varepsilon_1 = 4.73$ $\quad \alpha_1 = 0.9825$ $\quad f_1(0.5) = 1.0$

$\varepsilon_2 = 7.853$ $\quad \alpha_2 = 1.0007$

The A_{mn}, B_{11}, B_{22}, D_1, D_2, β_r are mode shape integrals as defined below.

$$A_{20} = \int_0^1 \left[f_1(\xi)\right]^2 d\xi$$

$$A_{02} = \int_0^1 \left[f_2(\xi)\right]^2 d\xi$$

$$A_{mn} = \frac{1}{A_{20}} \int_0^1 \left[f_1(\xi)\right]^m \left[f_2(\xi)\right]^n d\xi$$

$$A'_{mn} = \frac{1}{A_{02}} \int_0^1 \left[f_1(\xi)\right]^m \left[f_2(\xi)\right]^n d\xi$$

$$B_{mn} = \int_0^1 \frac{df_m(\xi)}{d\xi} \cdot \frac{df_n(\xi)}{d\xi}\, d\xi$$

$$D_n = \int_0^1 f_n^{IV}(\xi)\, f_n(\xi)\, d\xi$$

$$\beta_0 = B_{22}/B_{11}$$

$$q_{10} = \frac{1}{B_{11}} \int_0^1 \frac{df_0(\xi)}{d\xi} \cdot \frac{df_1(\xi)}{d\xi}\, d\xi$$

$$\tilde{q}_{10} = \frac{1}{B_{11}} \int_0^1 \frac{d\tilde{f}_0(\xi)}{d\xi} \cdot \frac{df_1(\xi)}{d\xi}\, d\xi$$

It may be noted that $B_{12} = 0$ has been used in the formulation. B_{11}, D_1, etc. are tabulated in Ref. 30.

$B_{11} = 4.877$ $\qquad$ $D_1 = 198.46$

$B_{22} = 46.05$ $\qquad$ $D_2 = 3803.5$

The A_{mn} are evaluated by numerical integration by using Waddel's rule.

$A_{20} = 0.396$ $\qquad$ $A_{40} = 0.734$ $\qquad$ $A_{22} = 1.11$

$A_{02} = 1.0$ $\qquad$ $A'_{04} = 1.689$ $\qquad$ $A'_{22} = 0.44$

APPENDIX E

HARMONIC BALANCE EQUATIONS

For the harmonic balance solution of Eq. 5.21 , it is convenient to make a change of variable

$$p_1 = q_1 + q_0$$

$$p_2 = \tilde{q}_1 + \tilde{q}_0$$

Eq. 5.21 reduces to simply

$$\ddot{p}_m + \gamma_m \dot{p}_m + \gamma p_m + \alpha_1 p_m (p_1^2 + p_2^2) - \delta_m = 0 \qquad m = 1,2$$

where $\gamma \equiv r_1^2 - \alpha_1 (q_0^2 + \tilde{q}_0^2)$

$$q_2 \equiv \tilde{q}_1$$

$$\delta_1 \equiv r_1^2 q_0 \qquad \delta_2 \equiv r_1^2 \tilde{q}_0$$

For convenience all $\sim$ sign are replaced by a first subscript 2 .

Thus

$$p_1 - q_{10} = b_{10} + b_{11}\cos\omega\tau + a_{11}\sin\omega\tau + b_{12}\cos 2\omega\tau + a_{12}\sin 2\omega\tau$$

$$p_2 - q_{20} = b_{20} + b_{21}\cos\omega\tau + a_{21}\sin\omega\tau + b_{22}\cos 2\omega\tau + a_{22}\sin 2\omega\tau$$

replaces Eq. 5.23 .

The algebraic equations to be solved are

Constants:

$$\alpha_1 \sum_{n=1}^{2} \left\{ b^*_{mo} B_{no} + \frac{1}{2}\left(b_{m1} B_{n1} + a_{m1} A_{n1} + b_{m2} b_{n2} + a_{m2} A_{n2} \right) \right\} + b^*_{mo} \gamma - \delta_m = 0$$

Cos $\omega\tau$:

$$(\gamma - \omega^2) b_{m1} + \omega q_m a_{m1} + \alpha_1 \sum_{n=1}^{2} \left\{ \left(b^*_{mo} B_{n1} + b_{m1} B_{no} \right) + \frac{1}{2}\left(b_{m1} B_{n2} + a_{m1} A_{n2} \; b_{m2} B_{n1} + a_{m2} A_{n1} + b_{m2} B_{n3} + a_{m2} A_{n3} \right) \right\} = 0$$

Sin $\omega\tau$:

$$(\gamma - \omega^2) a_{m1} - \omega q_m b_{m1} + \alpha_1 \sum_{n=1}^{2} \left\{ \left(b^*_{mo} A_{n1} + a_{m1} B_{no} \right) + \frac{1}{2}\left(b_{m1} A_{n2} + a_{m2} B_{n1} - a_{m1} B_{n2} - b_{m2} A_{n1} + b_{m2} A_{n3} - a_{m2} B_{n3} \right) \right\} = 0$$

Cos $2\omega\tau$:

$$(\gamma - 4\omega^2) b_{m2} + \omega q_m a_{m2} + \alpha_1 \sum_{n=1}^{2} \left\{ \left(b^*_{mo} B_{n2} + b_{m2} B_{no} \right) + \frac{1}{2}\left(b_{m1} B_{n1} - a_{m1} A_{n1} + b_{m1} B_{n3} + a_{m1} A_{n3} + b_{m2} B_{n4} + a_{m2} A_{n4} \right) \right\} = 0$$

Sin $2\omega\tau$:

$$(\gamma - 4\omega^2) a_{m2} - \omega q_m b_{m2} + \alpha_1 \sum_{n=1}^{2} \left\{ \left(b^*_{mo} A_{n2} + a_{m2} B_{no} \right) + \frac{1}{2}\left(b_{m1} A_{n1} + a_{m1} B_{n1} + b_{m1} A_{n3} - a_{m1} b_{n3} + b_{m2} A_{n4} - a_{m2} B_{n4} \right) \right\} = 0$$

$$m = 1, 2$$

where

$$b^*_{mo} = b_{mo} + q_{mo}$$

$$B_{no} = b^{*2}_{no} + \frac{1}{2}\left(b_{n1}^2 + a_{n1}^2 + b_{n2}^2 + a_{n2}^2 \right)$$

$$B_{n1} = 2 b^*_{no} b_{n1} + b_{n1} b_{n2} + a_{n1} a_{n2}$$

$$A_{n1} = 2 b^*_{no} a_{n1} + b_{n1} a_{n2} - b_{n2} a_{n1}$$

$$B_{n2} = 2 b^{*}_{no} b_{n2} + \frac{1}{2}(b_{n1}^2 - a_{n1}^2)$$

$$A_{n2} = 2 b^{*}_{no} a_{n2} + b_{n1} a_{n1}$$

$$B_{n3} = b_{n1} b_{n2} - a_{n1} a_{n2}$$

$$A_{n3} = b_{n1} a_{n2} + a_{n1} b_{n2}$$

$$B_{n4} = \frac{1}{2} (b_{n2}^2 - a_{n2}^2)$$

$$A_{n4} = b_{n2} a_{n2}$$

Newton Raphson's iteration scheme for solving a set of algebraic equations.

$$\left\{ f \right\}_{n+1} = 0 = \left\{ f \right\}_n + \left[J \right]_n \left\{ \Delta X \right\}_n \quad \text{WHERE} \quad \left[J \right] = \left[\frac{\partial f}{\partial X} \right]$$

One assumes a trial solution $\left\{ x_j \right\}_n$ and at each step solves the equations

$$\left[J \right]_n \left\{ \Delta X \right\} = - \left\{ f \right\}_n \qquad \left\{ X \right\}_{n+1} = \left\{ X \right\}_n + \left\{ \Delta X \right\}$$

Convergence criteria $|\Delta X_j| \leq 10^{-4}$. X_j is of order 1.

REFERENCES

1. International Conference on Wind Effects on Buildings and Structures, Teddington, England, 1963.

2. Tall Buildings, Proceedings of the Symposium on Tall Buildings, University of Southampton, 1966.

3. International Research Seminar on Wind Effects on Buildings and Structures, Ottawa, Canada, 1967.

4. Symposium on Wind Effects on Buildings and Structures, Loughborough, England, 1968.

5. Blankson, I. and Finston, M., Summary of Experimental Studies on Oscillating Cables, M.I.T. Aerophysics Lab. T.R. 151, April, 1969.

6. Majumdar, A.S., and Douglas, W.J.M., Autocorrelation Measurements in the Nearwake of Square Section Cylinder in Turbulent Free Stream, Physics of Fluids, June, 1970.

7. Roshko, A., On Drag and Shedding Frequencies of Two Dimensional Bluff Bodies, NACA, TN3169, 1953.

8. Hoerner, S.F., Fluid Dynamics Drag, Published by the Author, New Jersey, 1965.

9. Reed, W.H., III, Ground Wind Load Considerations for Space Shuttle Vehicles, Space Transportation System Technology Symposium, Vol. II, Dynamics and Aeroelasticity, 1970, NASA Lewis Research Centre, Cleveland, Ohio, NASA TMX 52876, Vol. II.

10. Davison, A.E., Dancing Conductors, Trans AIEE 49, pp. 1444-1449, 1930.

11. Hogg, A.D., and Edwards, A.T., The Status of Conductor Galloping Problem in Canada, Paper No. 12, Ref. 1, 1963.

12. Hogg, A.D., and Edwards, A.T., Conductor Galloping Studies in Ontario Hydro, Paper No. 8, Ref. 3, 1967.

13. Richards, D.T.W., Aerodynamic Properties of Savern Crossing Conductors, Paper No. 8, Ref. 1, 1963.

14. Den Hartog, J.P., Transmission Line Vibration due to Sleet, Trans AIEE 51, pp. 1074-76, 1932.

15. Den Hartog, J.P., Mechanical Vibrations, McGraw Hill, 1947.

16. Parkinson, G.V., and Brook, N.P.H., On Aeroelastic Instability of Bluff Cylinders, ASME Trans. Journal of Applied Mechanics, June, 1961.

17. Parkinson, G.V., and Smith, J.D., An Aeroelastic Oscillator with Two Stable Limit Cycles, ASME Trans J.A.M., June, 1962.

18. Parkinson, G.V., and Smith, T.D., Square Prism as an Aeroelastic Non-Linear Oscillator, Quarterly of J. of Mechanics and App. Math., Vol. XVII, Part 2, 1964.

19. Parkinson, G.V., Aeroelastic Galloping in One Degree of Freedom, Paper No. 23, Ref. 1, 1963.

20. Parkinson, G.V., and Modi, V.T., Recent Research on Wind Effects on Bluff Two Dimensional Bodies, Paper No. 18, Ref. 3, 1967.

21. Parkinson, G.V. and Santosham, T.V., Cylinders of Rectangular Section as Aeroelastic Non-linear Oscillator, Paper No. 1, ASME-67-Vib-50, ASME Vibration Conference, Boston, March, 1967.

22. Novak, M., Aeroelastic Galloping of Rigid and Elastic Bodies, Research Report, University of Western Ontario, Faculty of Engineering Science, London, Ontario, Canada, March, 1968.

23. Novak, M., Aeroelastic Galloping of Prismatic Bodies, Journal of Engineering Mechanics Division, EM-1, Proc. of ASCE, Feb. 1969.

24. Novak, M., Galloping Oscillation of Prismatic Structures, J. of Eng. Mech. Div., EM-1, Proc. of ASCE, Feb. 1972.

25. Novak, M., and Davenport, A.G., Aeroelastic Instability of Prisms in Turbulent Flow, J. of Eng. Mech. Div., EM-1, Proc. of ASCE, Feb. 1970.

26. Richardson, A.S. and Martuccelli, J.R., Research Study on Galloping of Electric Power Transmission Lines, M.I.T., Aeroelastic and Structures Research Laboratory, Progress Report No. 1-6, 1960-61.

27. Richardson, A.S., and Martuccelli, J.R., An Investigation of Galloping Transmission Line Conductors, IEEE Trans. Paper No. 63-1029, 1963.

28. Richardson, A.S., and Martuccelli, J.R., A Proposed Solution to the Problem of Galloping Conductors, IEEE Conference Paper No. C.P. 64-46, 1964.

29. Richardson, A.S. and Martuccelli, J.R., A Further Investigation of Galloping Transmission Line Conductors, IEEE Conference Paper No. C.P. 64-45, 1964.

30. Young, D., Vibration of Rectangular Plates by Ritz Method, Journal of Applied Mechanics, 17, 4, pp. 448-453, Dec. 1950.

31. Hore, P.S., Vibration of a Suspended Elastic Cable, S.M. Thesis, M.I.T. Aero and Astro. Dept., June, 1970.

32. Bogoliubov, N.N., and Mitropolosky, Y.A., Asymptotic Methods in the Theory of Non-linear Oscillation, Hindustan Publishing Corporation, 1961.

33. Vickery, B.J., Fluctuating Lift and Drag on a Long Cylinder of Square Cross Section in a Smooth and in a Turbulent Stream, J. of Fluid Mech., Vol. 25, Part 3, 1966.

34. Delany, N., and Sorensen, N.E., Low Speed Drag of Cylinders of Various Shapes, NACA TN 3038, 1953.

35. Harlow, H.F., and Fromm, E.J., Dynamics and Heat Transfer in the Von-Karman Wake of a Rectangular Cylinder, The Physics of Fluids, Vol. 7, No. 8, Aug. 1964.

36. Bluff Bodies and Vortex Shedding, A Report on Euromech. 17, Journal of Fluid Mechanics, Vol. 45, Part 2, January, 1971.

37. Toebes, G.H., The Unsteady Flow and the Wake Near an Oscillating Cyliner, ASME, Journal of Basic Engineering, September, 1969.

38. Griffin, O.M., The Unsteady Wake of an Oscillating Cylinder at Low Reynolds Number, ASME, Journal of Applied Mechanics, December, 1971.

39. Dugundji, J., and Hore, P., Brief Handbook for the Sum of Two Harmonics, M.I.T., Aeroelastic and Structures Research Laboratory, ASRL-TR-159-2, November, 1970.

TABLE 1

CANTILEVER BEAM PARAMETER

Length	l	=	13.1 inches
Side of square	b	=	0.09 inches
Mass/length	m	=	0.01233 lb/ft
Young's modulus	E	=	30×10^6 psi (steel)
	EI/mgl^3	=	9.58 (From ω_1)
		=	9.74 (I for round rod)

First bending mode natural frequency

ω_1 = 9.4 CPS (Theory 9.5 CPS with I for round rod)

TABLE 2

POLYNOMIAL COEFFICIENTS

The following table gives the coefficients P_n, Q_n of 8th degree polynomial fit of C_N, C_C vs. Tanβ curve of Fig. 7, 8 respectively.

C_N vs. Tanβ

Position	A	A	D
Velocity	37F/S	65F/S	37F/S
P_o	0.025	0.025	-.007
P_1	0.88	0.62	1.35
P_2	0.25	0.07	-0.7
P_3	4.37	7.67	-14.7
P_4	-10.0	-3.9	-4.3
P_5	-151.8	-181.6	-18.3
P_6	117.2	52.0	83.9
P_7	454.7	526.2	172.8
P_8	-340.0	-144.5	-263.8

$$C_N = \sum_{n=0}^{8} P_n (\tan\beta)^n \qquad |\tan\beta| \leq 0.45$$

TABLE 2 (Continued)

C_C vs. Tanβ

Position	A	A	D
Velocity	37F/S	65F/S	37F/S
Q_o	1.24	1.54	1.07
Q_1	-0.3	-0.47	0.2
Q_2	-9.8	-14.5	-3.1
Q_3	7.9	9.1	1.1
Q_4	200.1	255.1	115.5
Q_5	-66.7	-60.4	-12.4
Q_6	-1208.4	-1471.1	-789.2
Q_7	159.5	123.1	24.9
Q_8	2434.2	2890.0	1699.0

$$C_C = \sum_{n=o}^{8} Q_n (\tan\beta)^n \qquad |\tan\beta| \leq 0.45$$

TABLE 3

CABLE PARAMETER

Span	$l = 3.02$ ft
Square section side	$b = 0.09$ inch
Weight/length	$mg = 0.00675$ lb/ft
Bending rigidity	$EI = 0.0019$ lb-ft^2
Tensile stiffness	$AE = 7090$ lbs
EI/mgl^3	$= 0.01$
AE/mgl	$= 0.3478 \times 10^6$

TABLE 4

CABLE RESPONSE DESCRIPTION

U = Free stream velocity in FT/SEC

ω_1 = 1st mode oscillation frequency in CY/SEC

ω_2 = 2nd mode oscillation frequency in CY/SEC

θ = Inclination in degrees (see Fig. 20)

W_M/d = Midspan single amplitude/span (see Fig. 24)

1BM, 2BM - 1st and 2nd bending mode

$d/\ell = 0.011$

U	ω_1	ω_2	θ	W_M/d	Remarks
0	5.5	-	0°	-	-
20	-	16.3	30°	-	Small 2BM
26	-	17.5	35°	-	"
29	9.5	19.0	40°	0.4	1BM, Small 2BM
39	13.2	-	~65°	0.95	1BM
51	14.8	-	~80°	1.02	1BM, Small 2BM
71	18.6	-	-	1.6	"
61	16.3	-	-	1.3	"
34	11.0	-	~60°	0.7	"
26	-	18.0	40°	-	Small 2BM

TABLE 4 (Continued)

$d/\ell = 0.02$

U	ω_1	ω_2	θ	W_M/d	Remarks
0	4.6	-	0°	-	-
29	-	13.8		-	Small 2BM
36	7.8	1[illegible]	65°	0.16	Small 1BM & 2BM
39	8.2	17.0	70°	0.2	"
47	10.3	-	78°	0.28	1BM, Small 2BM
60	13.5	-	85°	0.57	"
73	16.0	-	-	0.74	"
81	17.8	-	-	0.85	"
59	13.3	-	~80°	0.58	"
45	10.0	20.0	~75°	0.21	"
27	-	13.0	~50°	-	"

TABLE 4 (Continued)

$d/\ell = 0.029$

$\frac{U}{-}$	ω_1	ω_2	θ	W_M/d	Remarks
0	4.0	-	0°	-	-
32	-	-	70°	-	Small 2BM
45	-	-	85°	-	Small 1BM & 2BM
50	8.3	-	-	0.23	1BM
68	11.0	-	-	0.25	1BM, Small 2BM
78	12.5	-	-	0.12	1BM, 2BM
88	14.2	28.4	-	0.06	2BM, Small 1BM
99	15.7	31.3	-	-	"
75	12.2	-	-	0.14	1BM, Small 2BM
56	9.2	-	-	0.24	"
50	8.3	-	-	0.09	Small 1BM
42	-	-	-	-	Small 2BM
36	-	-	78°	-	Quiet

TABLE 4 (Continued)

$d/\ell = 0.043$

U	ω_1	ω_2	θ	W_M/d	Remarks
0	3.3	-	0°	-	-
28	-	8.8	57°	-	Small 2BM
39	-	11.0	72°	-	"
55	7.5	-	~87°	0.0[illegible]	Small 1BM
58	7.8	-	-	0.[illegible]1	1BM
65	8.6	-	-	[illegible].5	1BM, Small 2BM
76	10.0	-	-	0.6	"
88	11.3	-	-	0.65	1BM & 2BM
100	13.8	-	-	0.43	"
94	12.3	-	-	0.53	"
82	10.5	-	-	0.64	"
69	9.2	-	-	0.6	1BM, Small 2BM
54	7.4	-	-	0.49	"
47	-	13.0	~80°	-	Small 2BM

TABLE 4 (Continued)

$d/\ell = 0.059$

U	ω_1	ω_2	θ	W_M/d	Remarks
0	2.8	-	0°	-	-
29	-	-	45°	-	Quiet
41	-	-	70°	-	Quiet
61	-	13.8	-	-	Small 2BM
62	6.9	-	-	0.52	1BM, Small 2BM
73	7.7	-	-	0.66	"
83	9.1	-	-	0.74	"
90	9.8	-	-	0.74	"
73	7.9	-	-	0.74	"
61	6.7	-	-	0.68	"
49	5.5	-	-	0.44	"
46	-	10.5	~75°	-	Small 2BM
36	-	9.3	~60°	-	"

TABLE 4 (Continued)

$d/\ell = 0.08$

U	ω_1	ω_2	θ	W_M/d	Remarks
0	2.5	-	0°	-	-
38	-	7.7	~62°	-	Small 2BM
47	-	9.2	~75°	-	"
50	4.7	-	~78°	0.36	1BM
63	5.8	-	~80°	0.51	"
70	6.5	-	~85°	0.52	1BM, Small 2BM
83	7.8	-	-	0.48	"
99	9.3	-	-	0.31	"
93	8.8	-	-	0.33	"
76	7.1	-	-	0.44	"
54	4.9	-	-	0.34	"
47	-	9.2	~70°	-	Small 2BM
24	-	-	30°	-	"

FIG. 1a OVERALL VIEW OF TEST SET UP

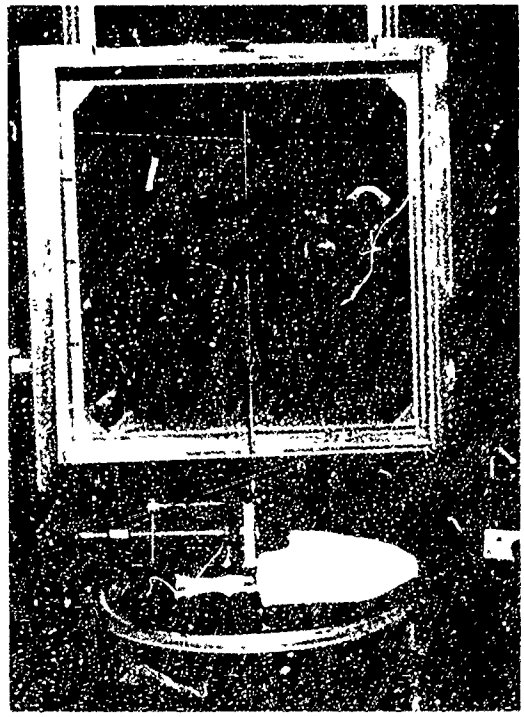

FIG. 1b CLOSEUP VIEW OF SPECIMEN BEAM

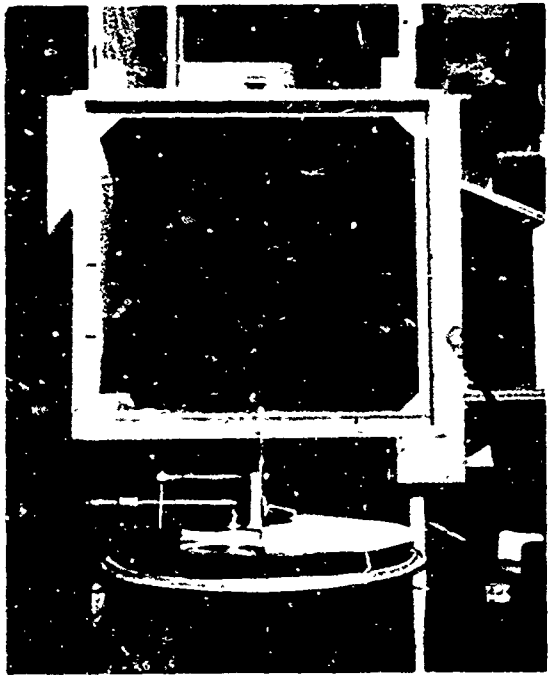

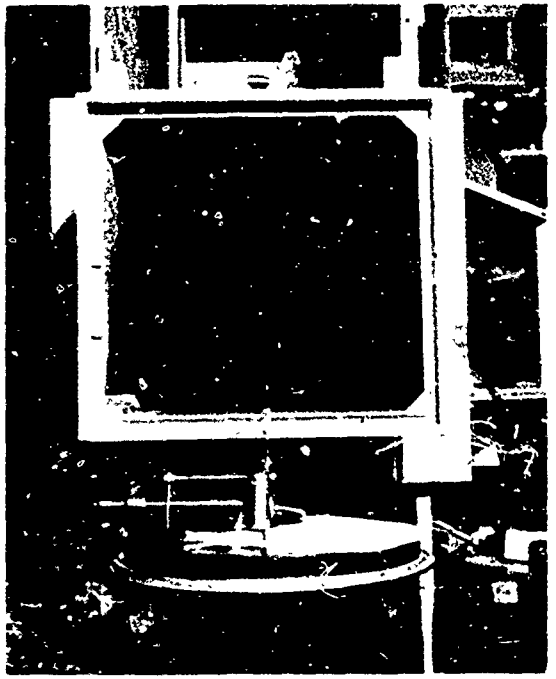

VIEW OF VIBRATING BEAM (POSITION A)

FIG. 1c AT U = 30 FT/SEC, α_o=0°
W_T = 1.65", γ=0°

FIG. 1d U = 66 FT/SEC, α_o=2.5°
WT = 2.1", γ= 15°

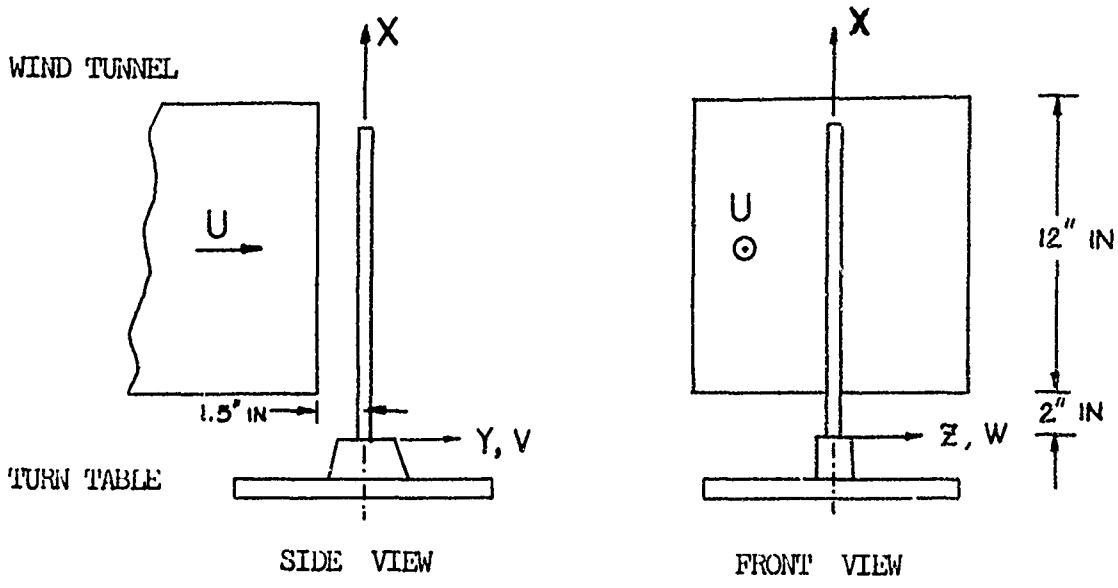

FIG. 2a SCHEMATIC DIAGRAM

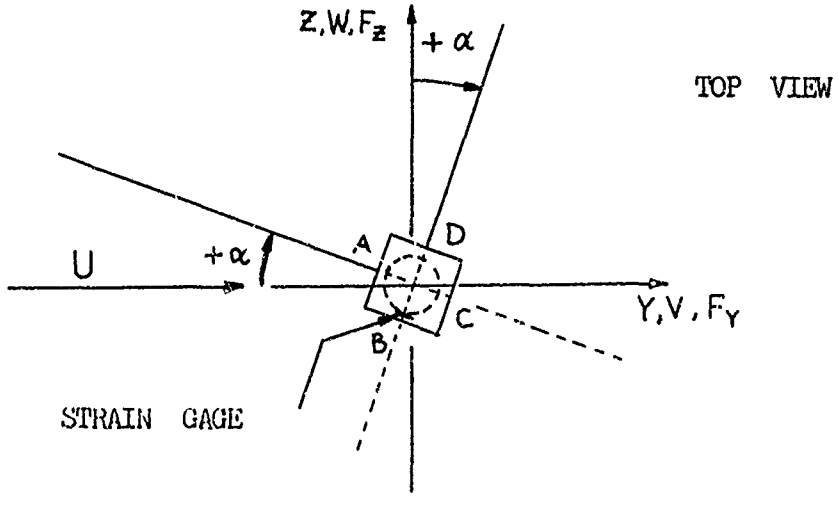

FIG. 2b COORDINATE SYSTEM

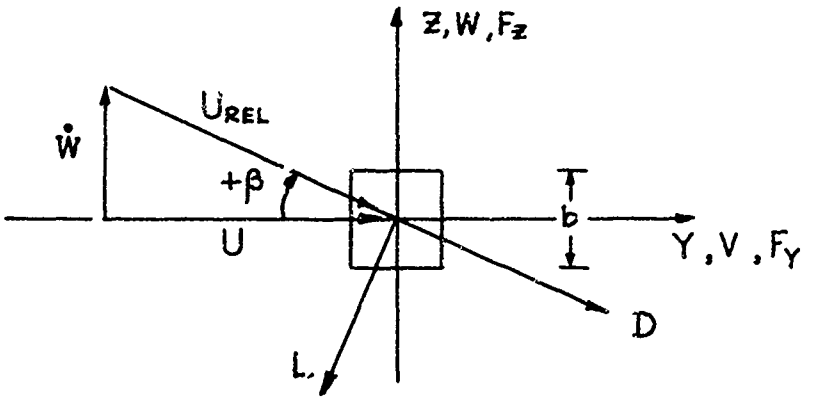

FIG. 2c FORCES ACTING AT $\alpha_o = 0$

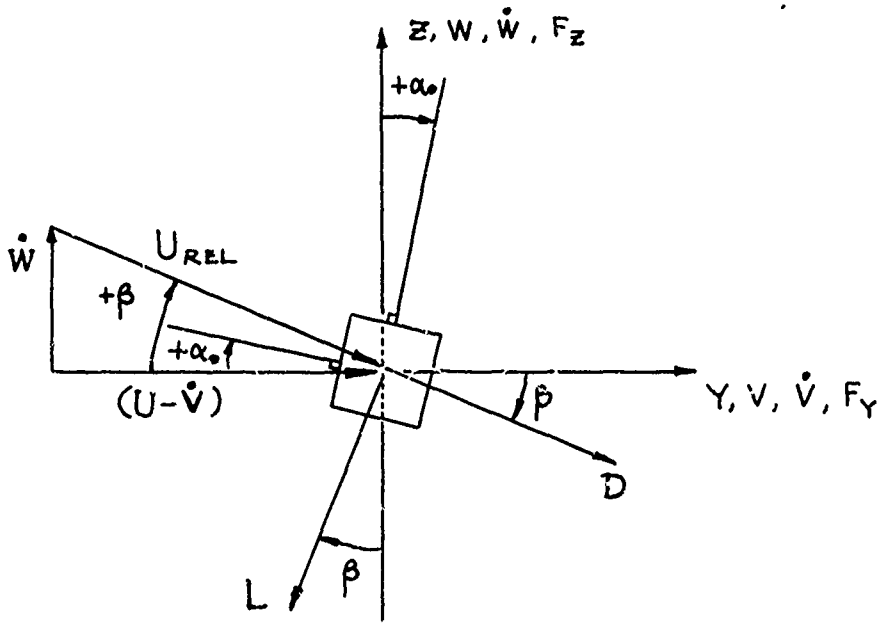

FIG. 2d FORCES ACTING AT INITIAL ANGLE OF ATTACK α_o

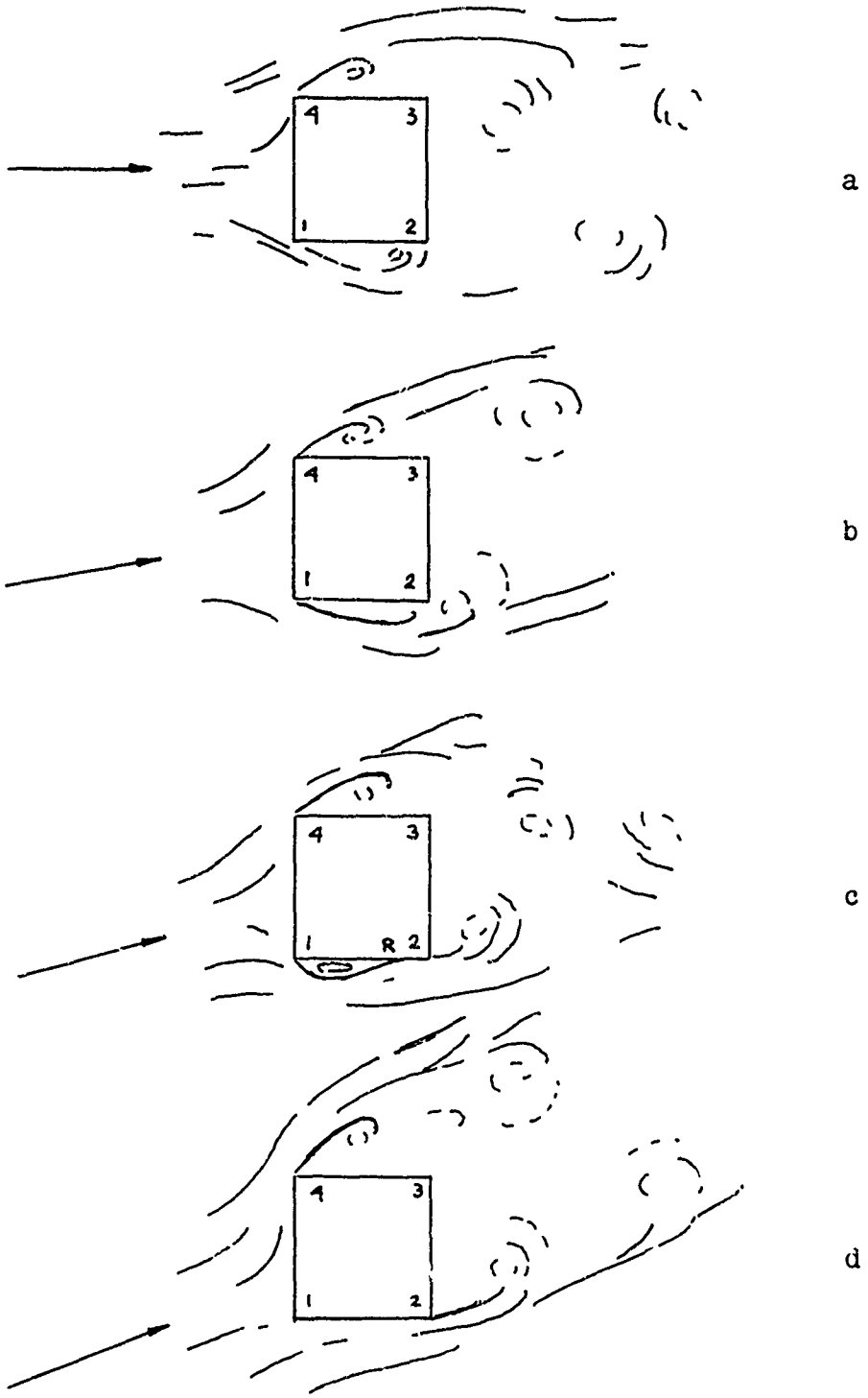

FIG. 3 FLOW AROUND SQUARE SECTION BODY

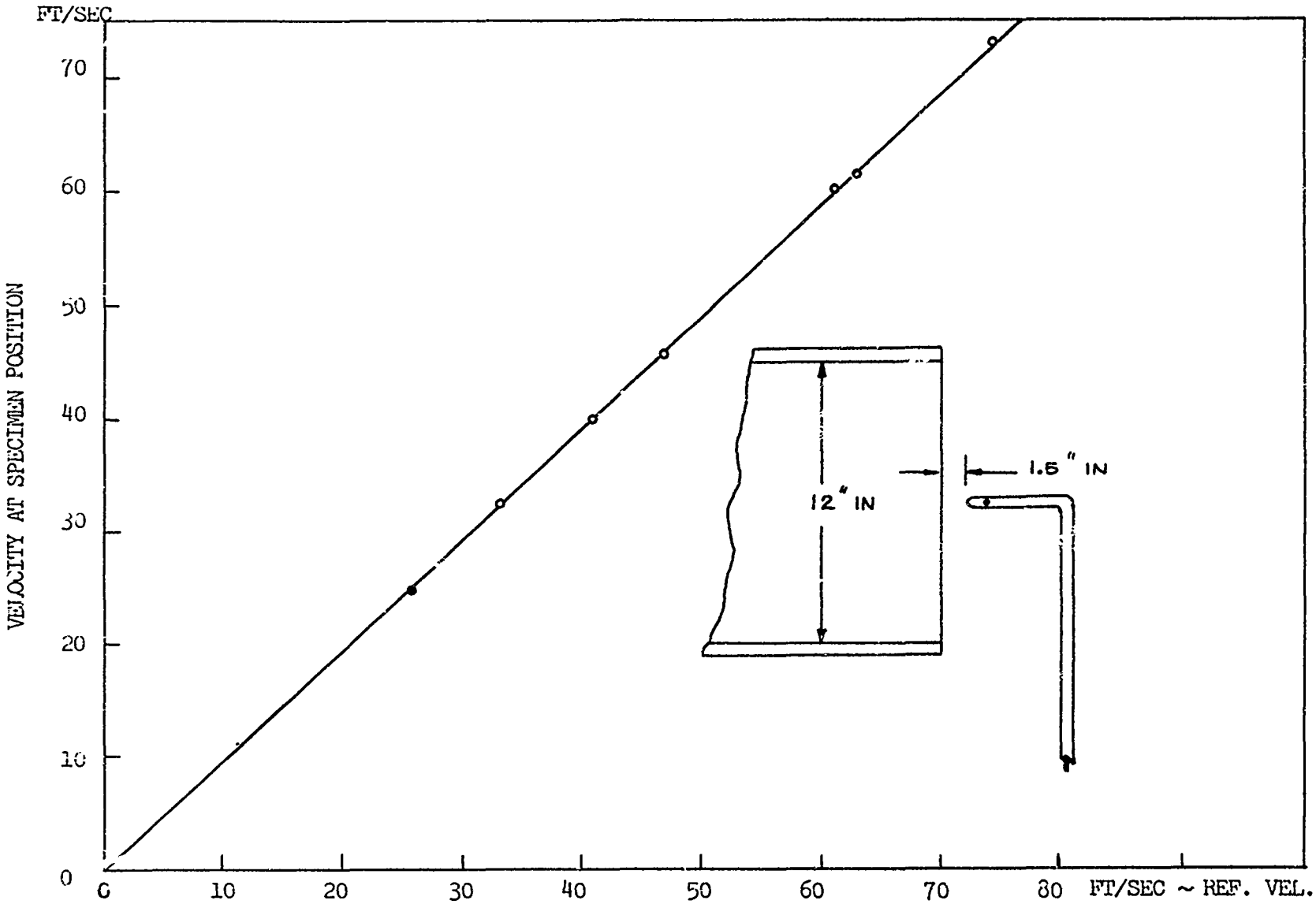

FIG. 4. VELOCITY AT SPECIMEN POSITION VS. REFERENCE VELOCITY

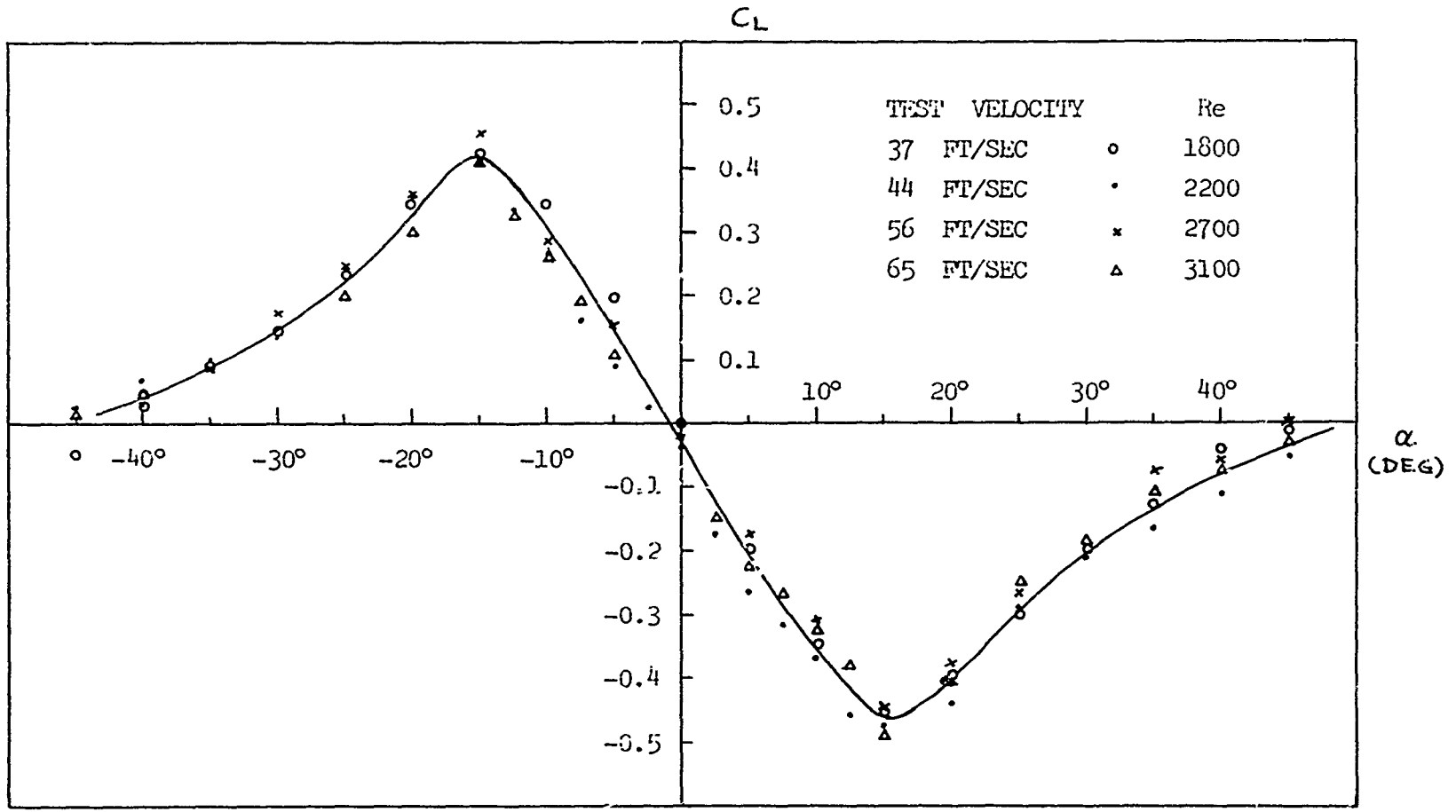

FIG. 5a C_L VARIATION WITH STATIC ANGLE OF ATTACK α (POSITION A)

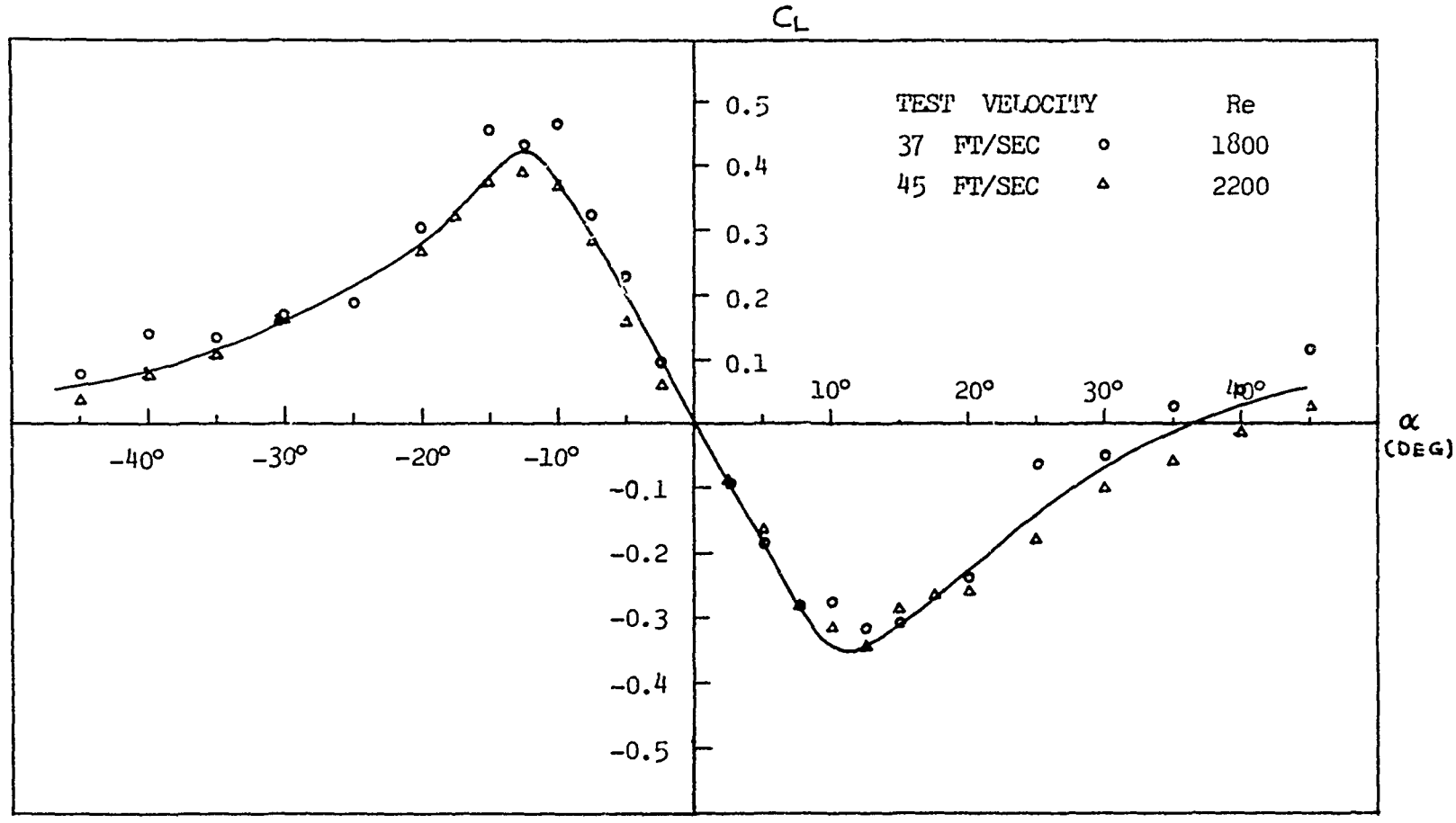

FIG. 5b C_L VARIATION WITH STATIC ANGLE OF ATTACK α (POSITION D)

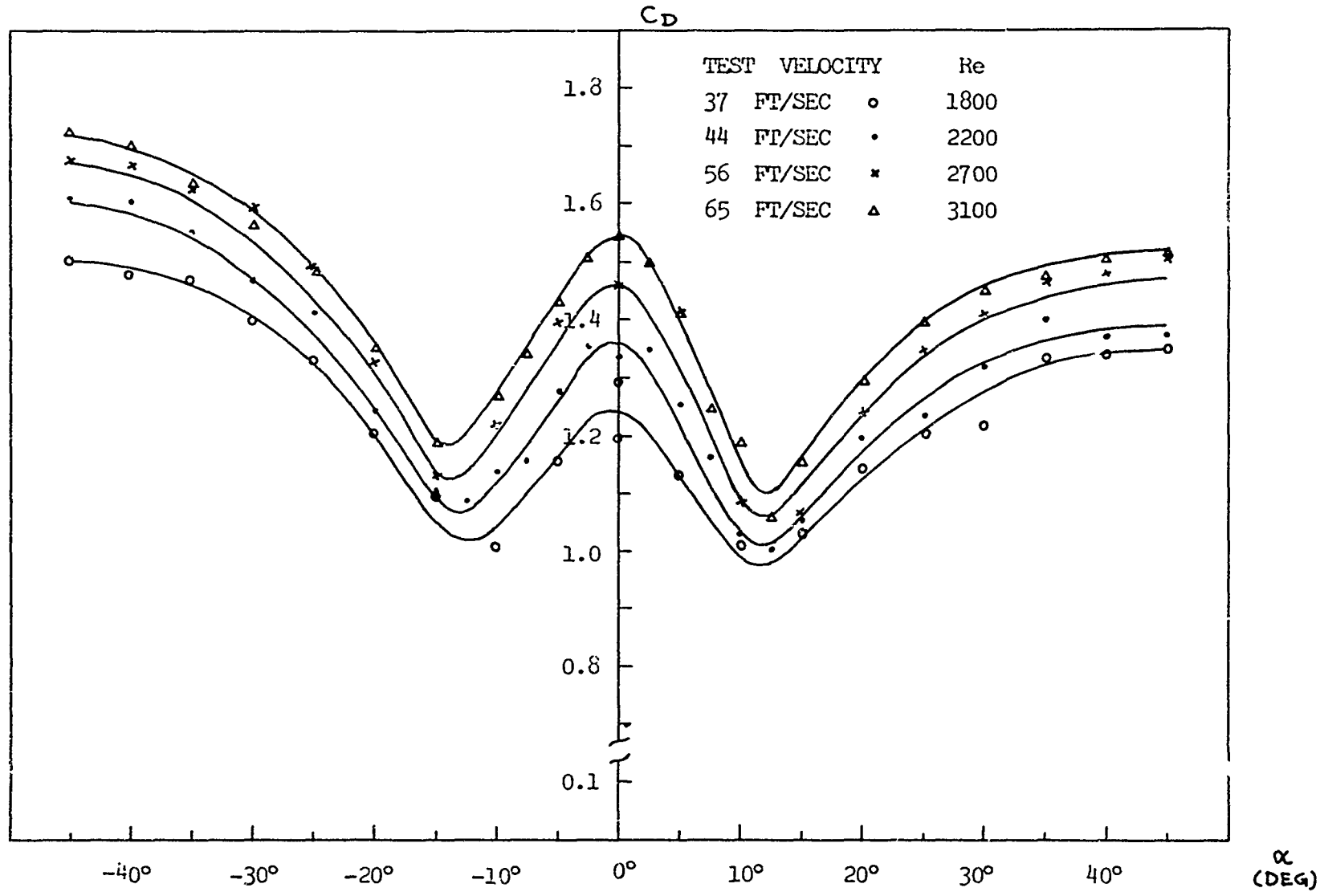

FIG. 6a C_D VARIATION WITH A STATIC ANGLE OF ATTACK α (POSITION A)

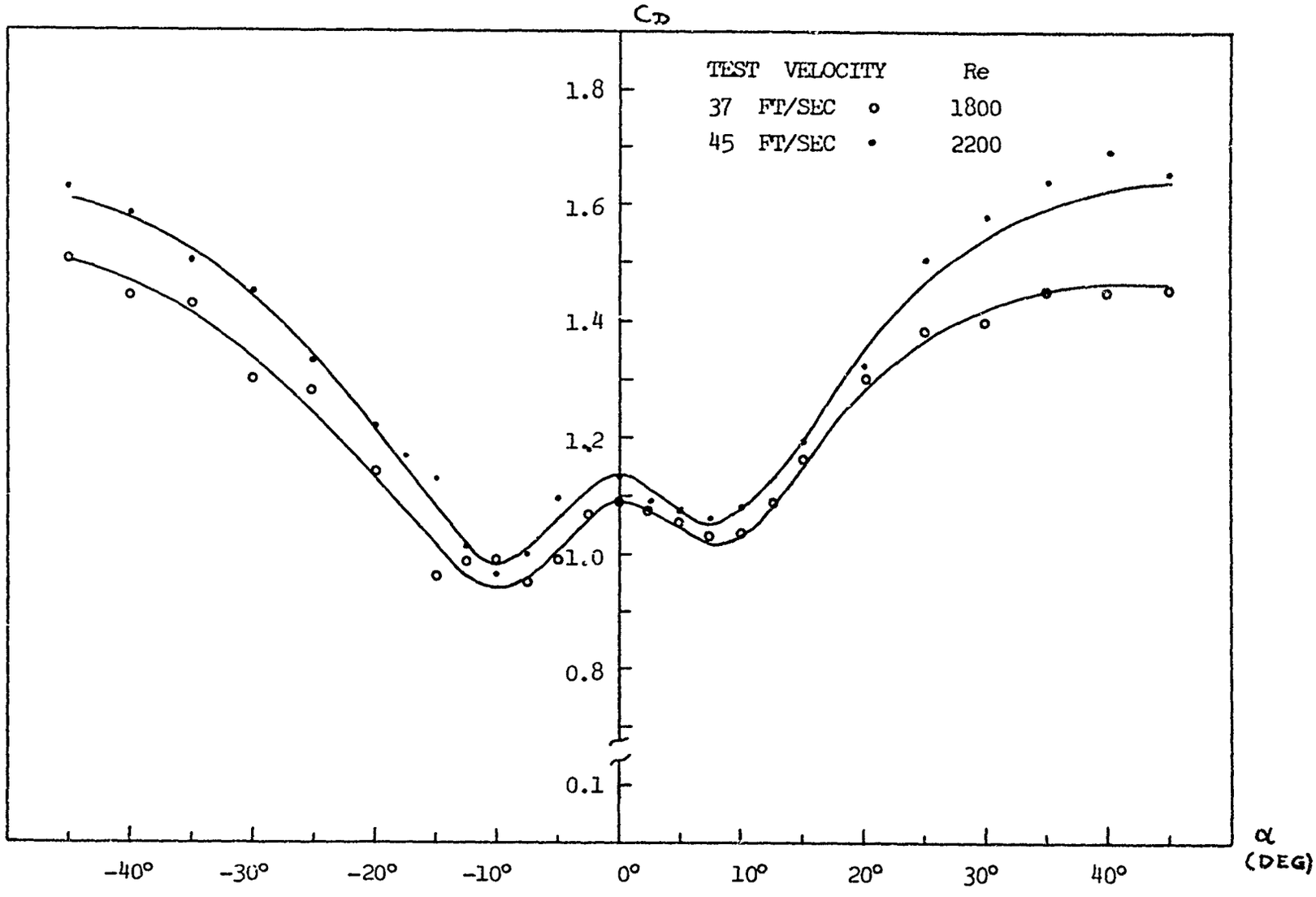

FIG. 6b C_D VARIATION WITH STATIC ANGLE OF ATTACK α (POSITION D)

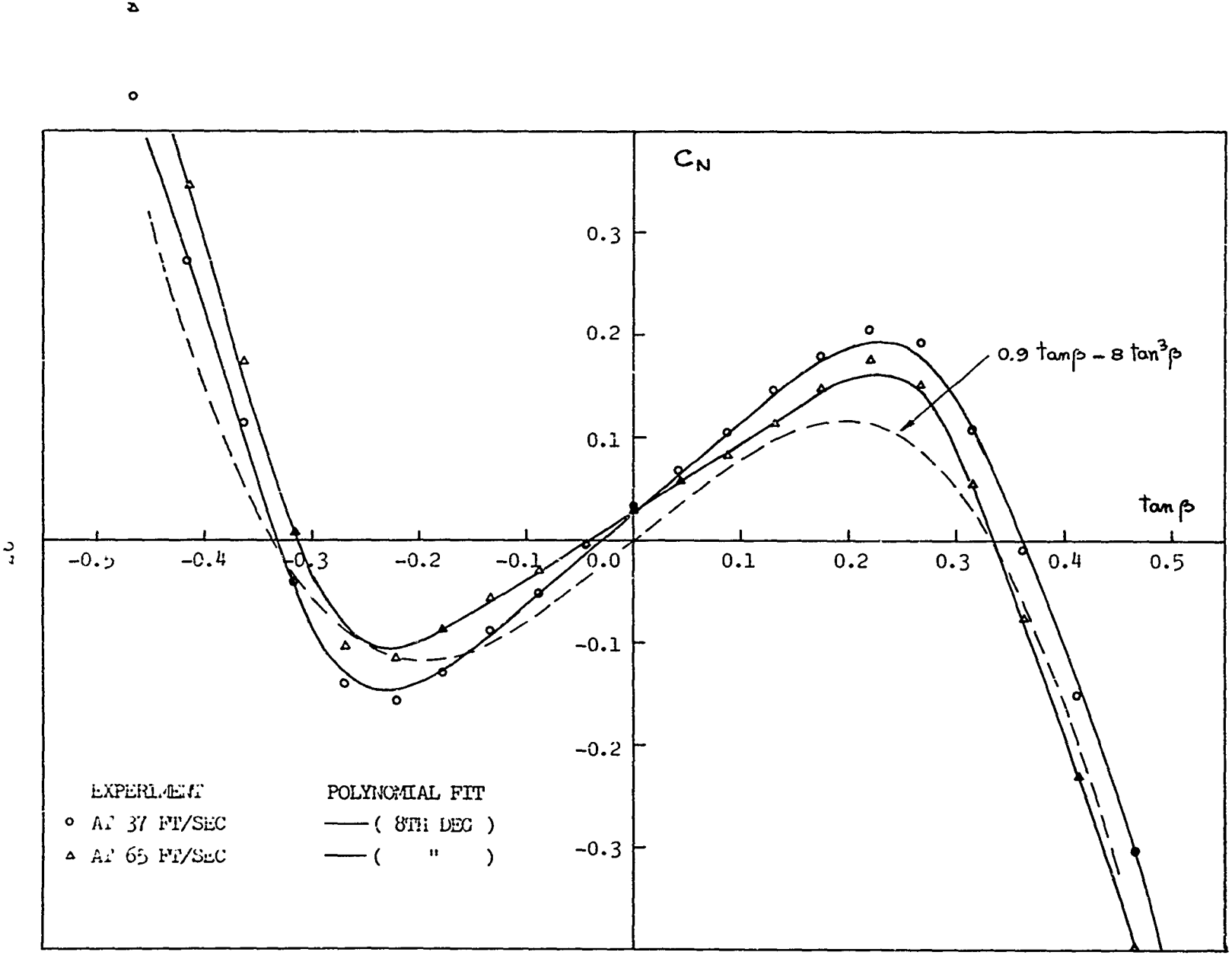

FIG. 7a C_N VS. tanß (POSITION A)

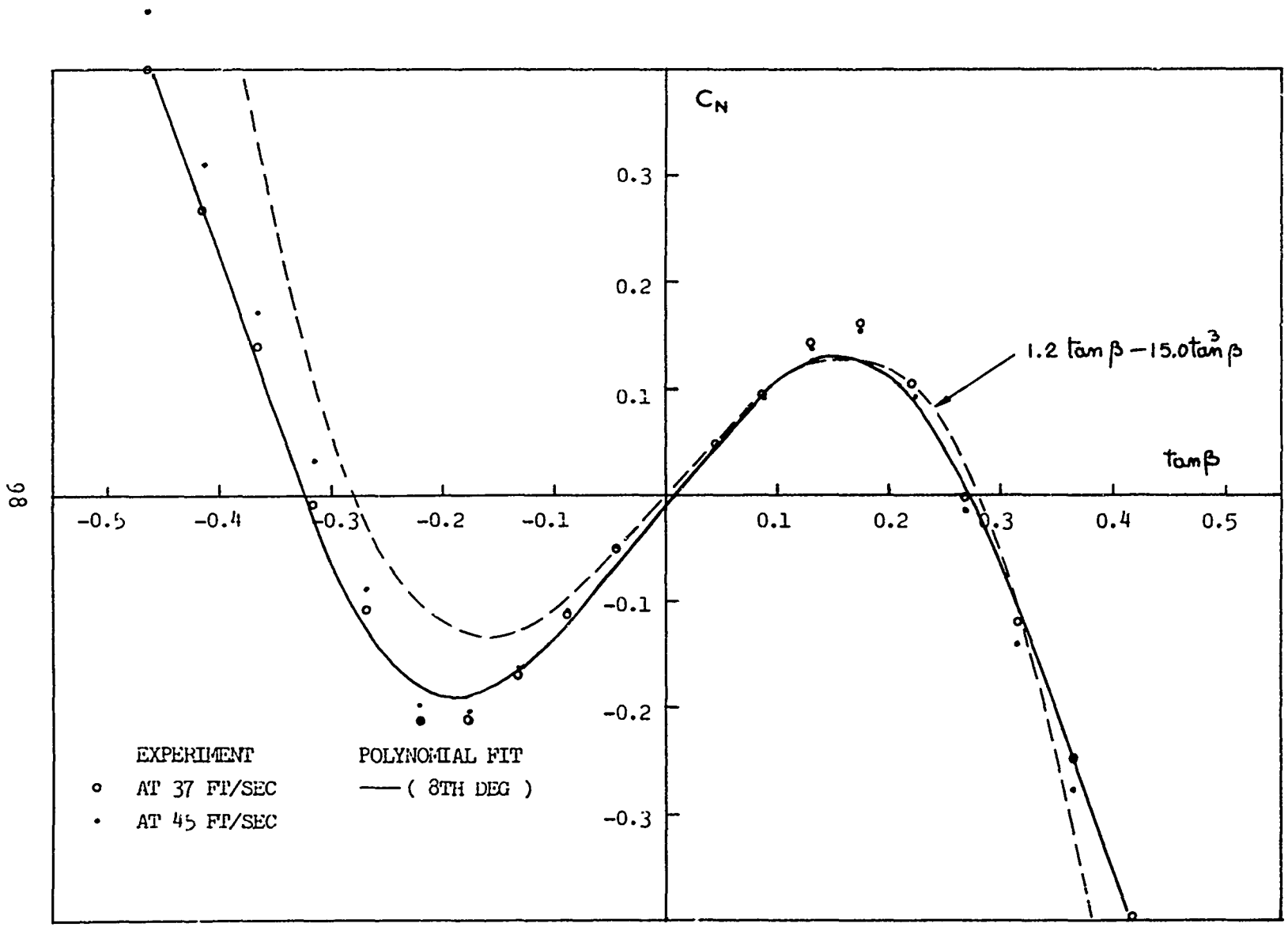

FIG. 7b C_N VS. tanß (POSITION D)

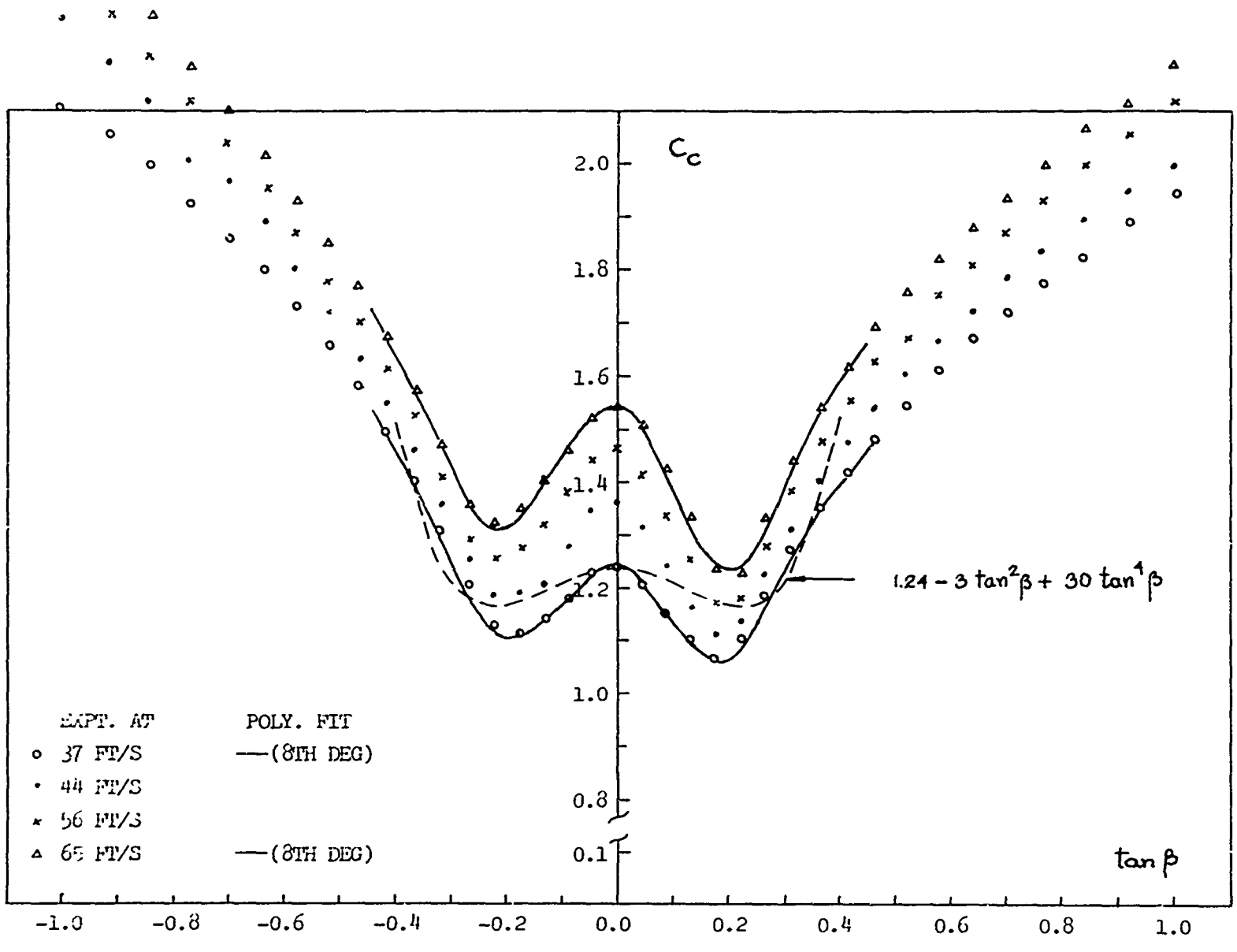

FIG. 8a C_C VS. tanβ (POSITION 1)

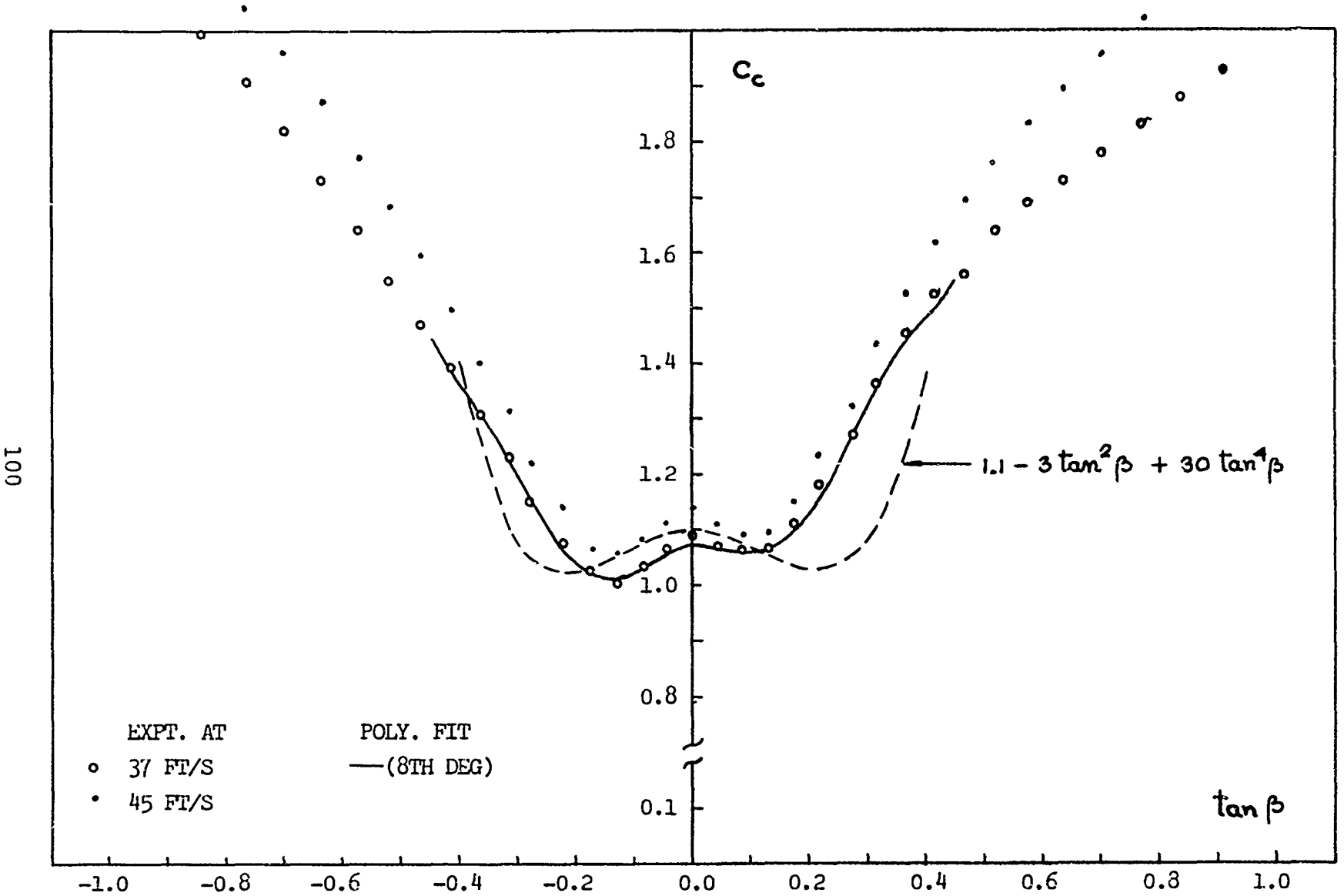

FIG. 8b C_C VS. tanβ (POSITION D)

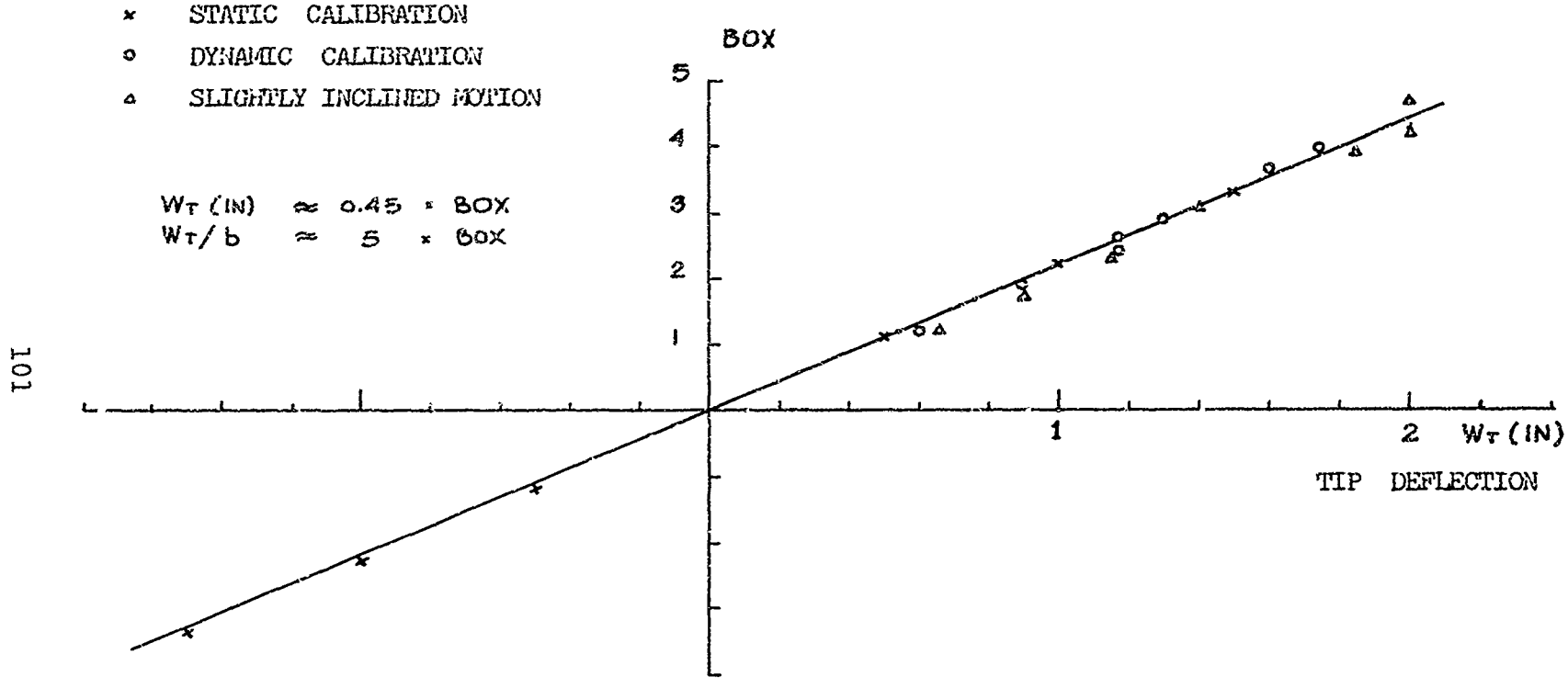

FIG. 9 STRAIN GAGE CALIBRATION CHART

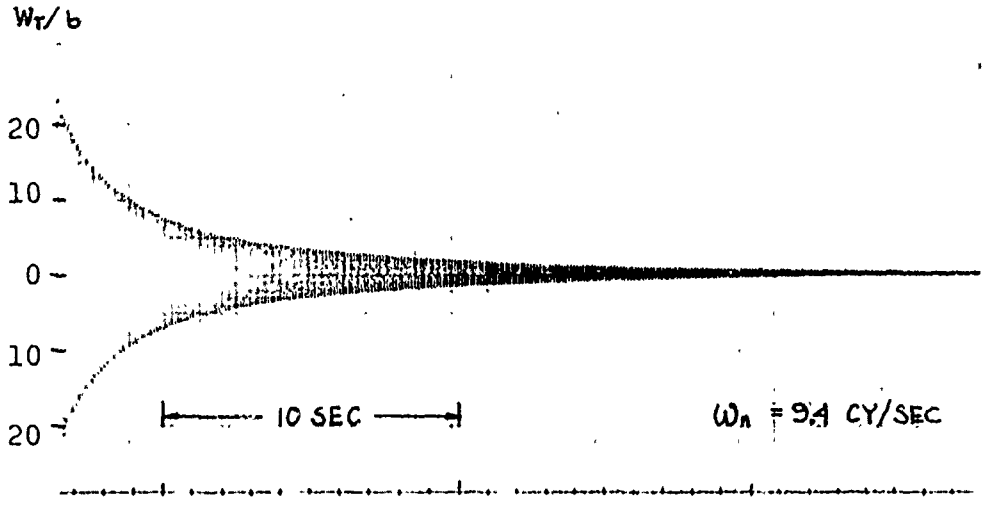

FIG. 10a SAMPLE FIRST BENDING DECAY RECORD

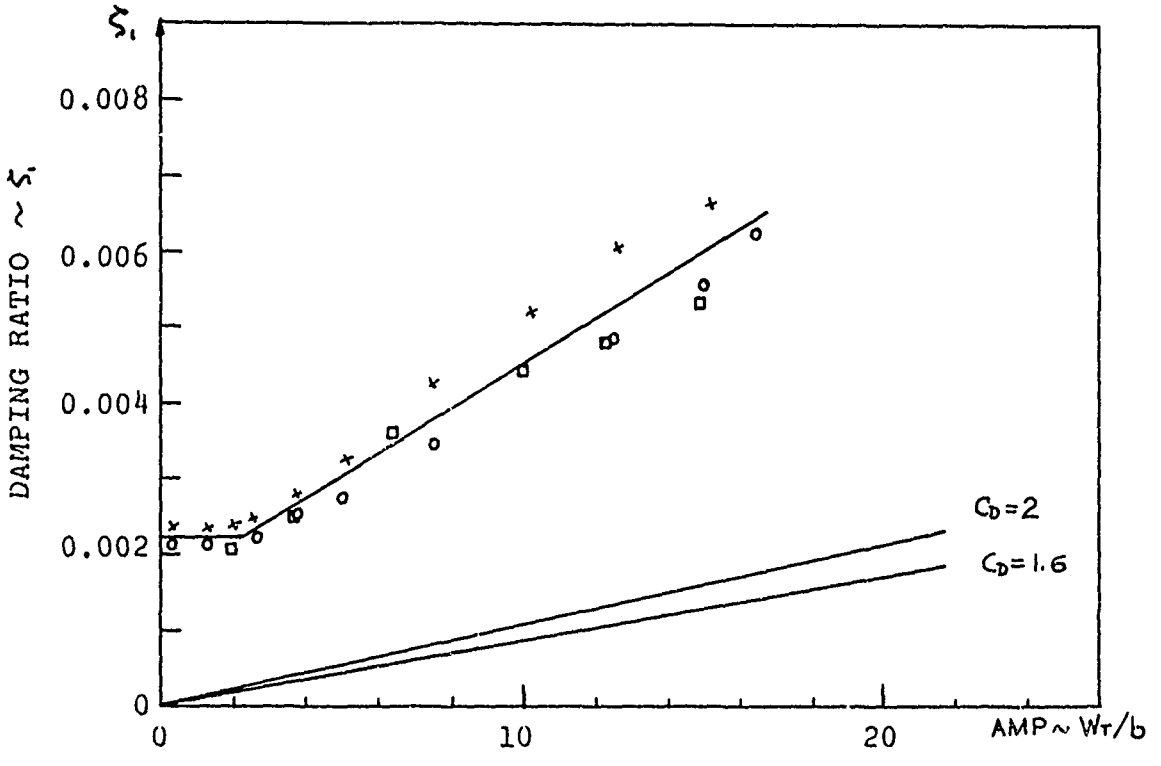

FIG. 10b DAMPING RATIO VARIATION WITH AMPLITUDE IN STILL AIR

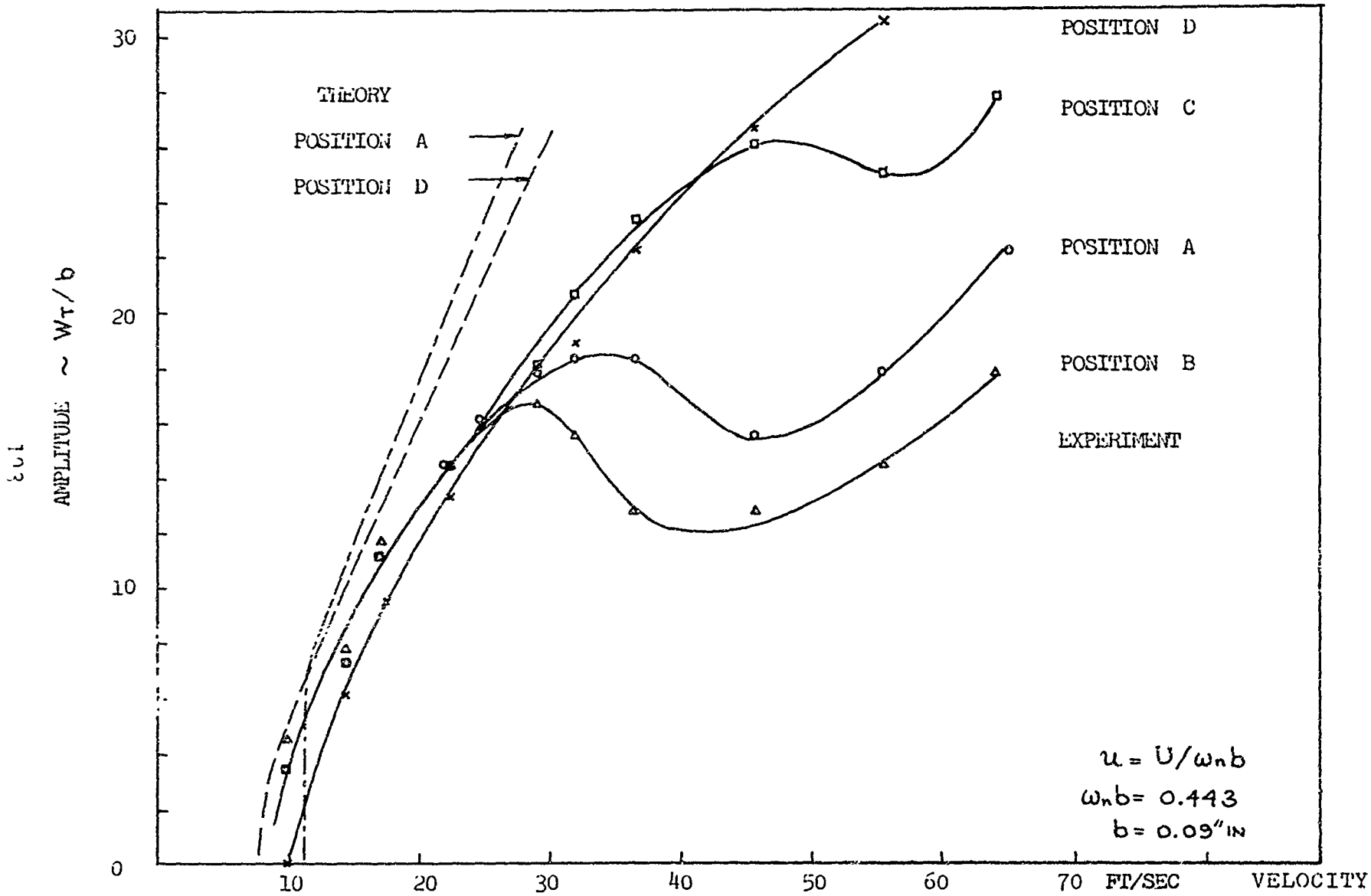

FIG. 11a STEADY STATE AMPLITUDE RESPONSE

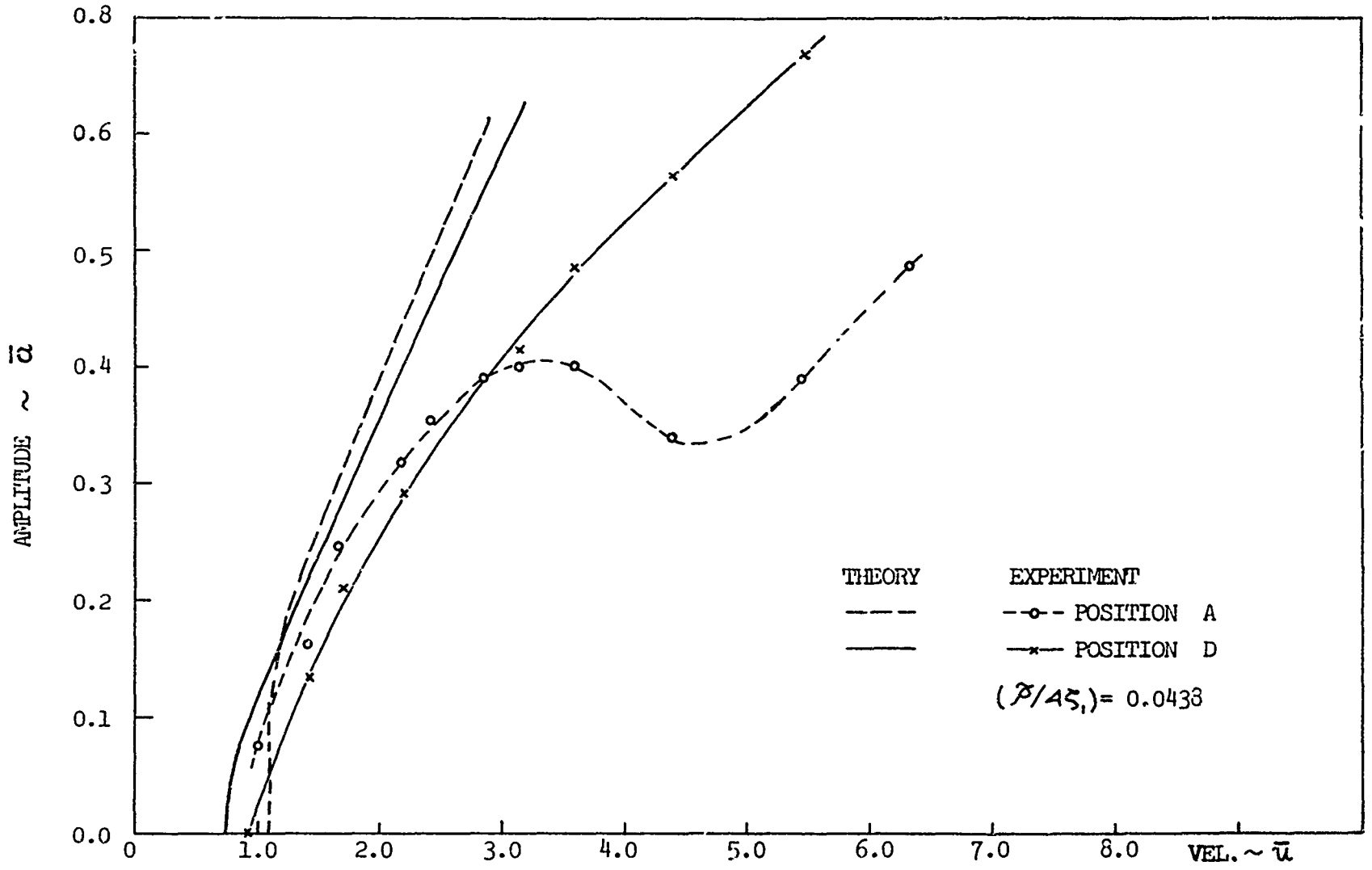

FIG. 11b STEADY STATE AMPLITUDE RESPONSE (THEORY & EXPT.)

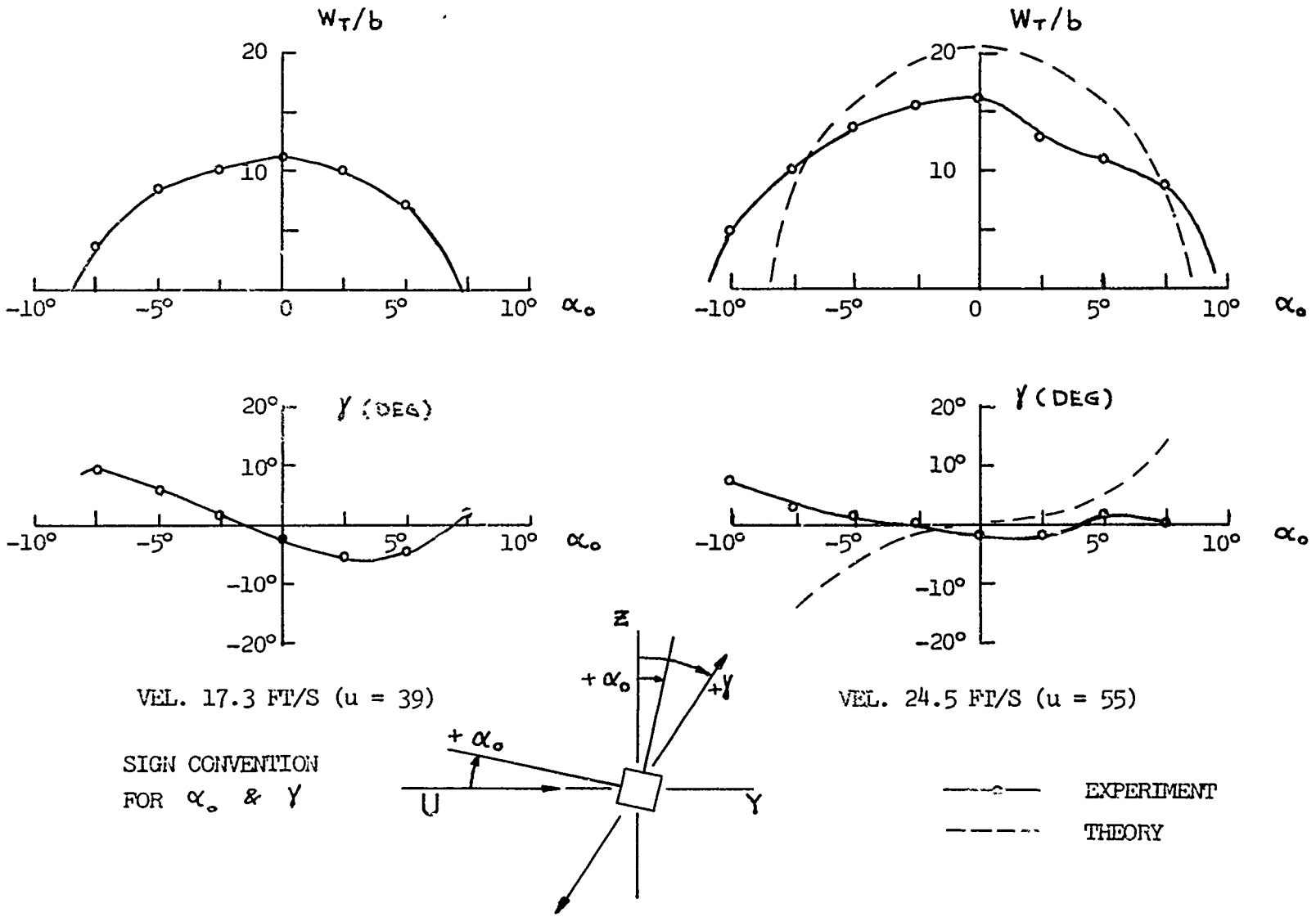

FIG. 12a,b STEADY STATE AMPLITUDE AND INCLINATION AT INITIAL ANGLE α_o (POSITION A)

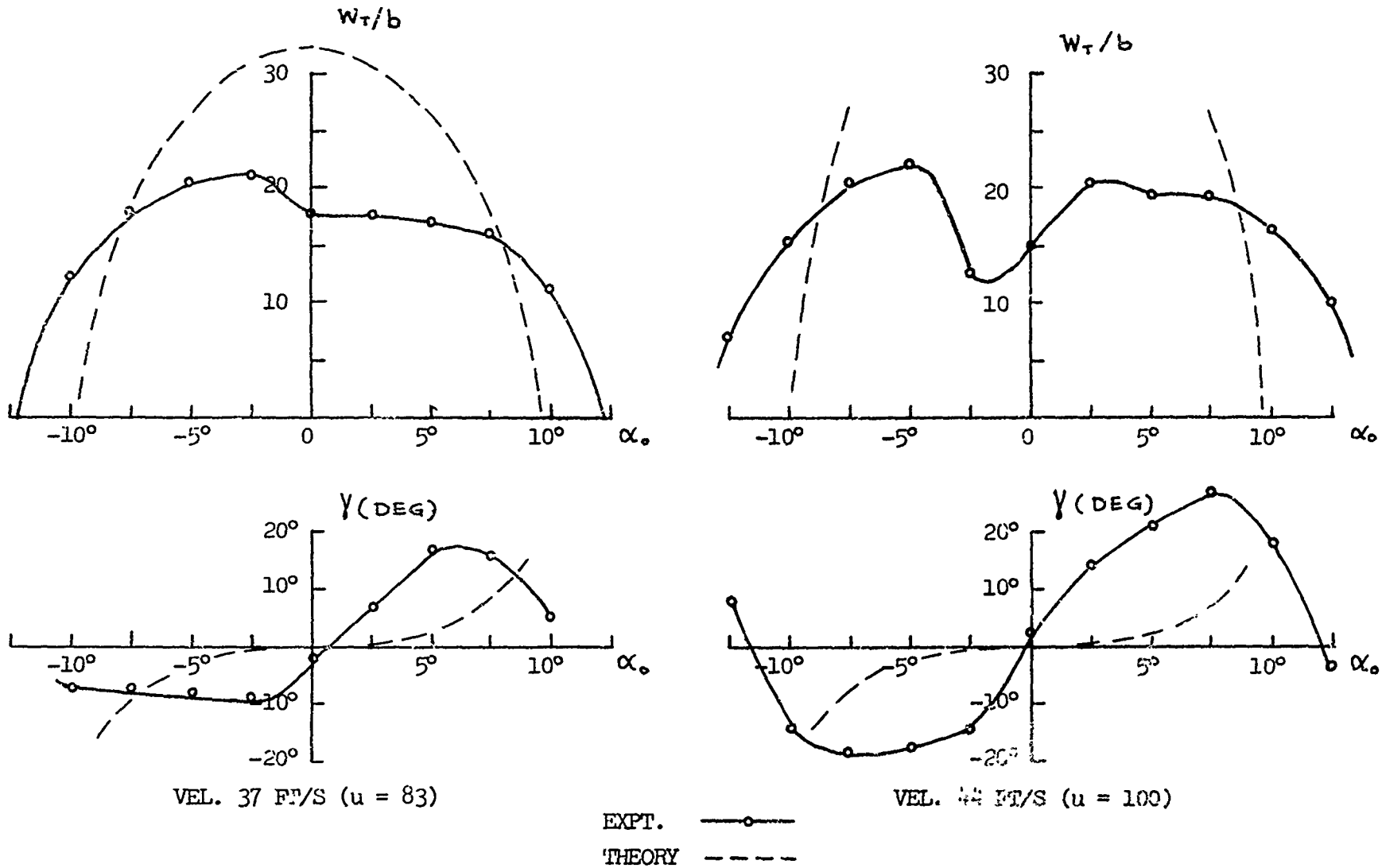

FIG. 12c,d STEADY STATE AMP. TUDE AND INCLINATION AT INITIAL ANGLE α_o (POSITION A)

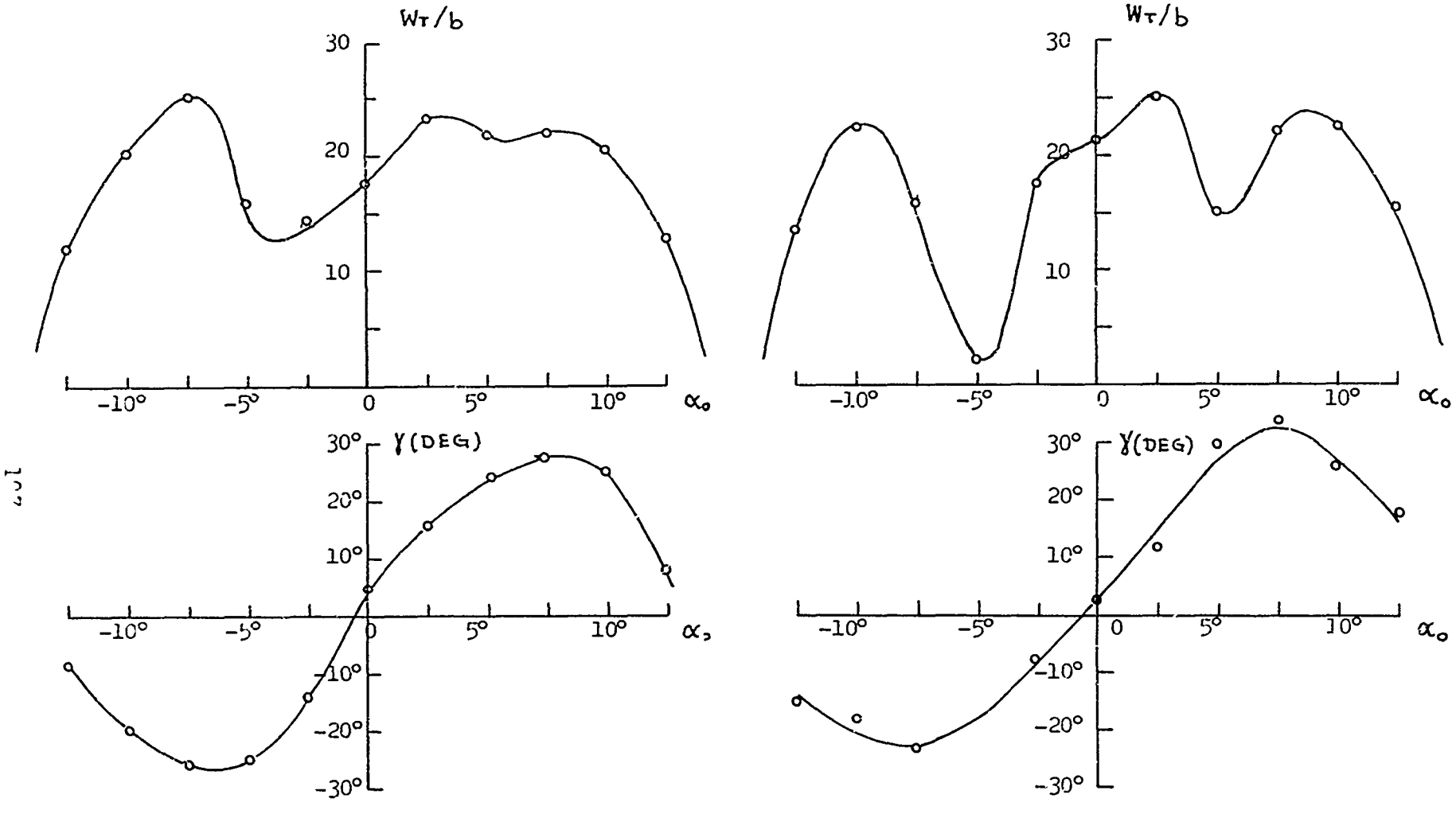

VEL. 56 FT/S (u = 126) EXPT. —o— VEL. 65 FT/S (u = 147)

FIG. 12e,f STEADY STATE AMPLITUDE AND INCLINATION AT INITIAL ANGLE α_o (POSITION A)

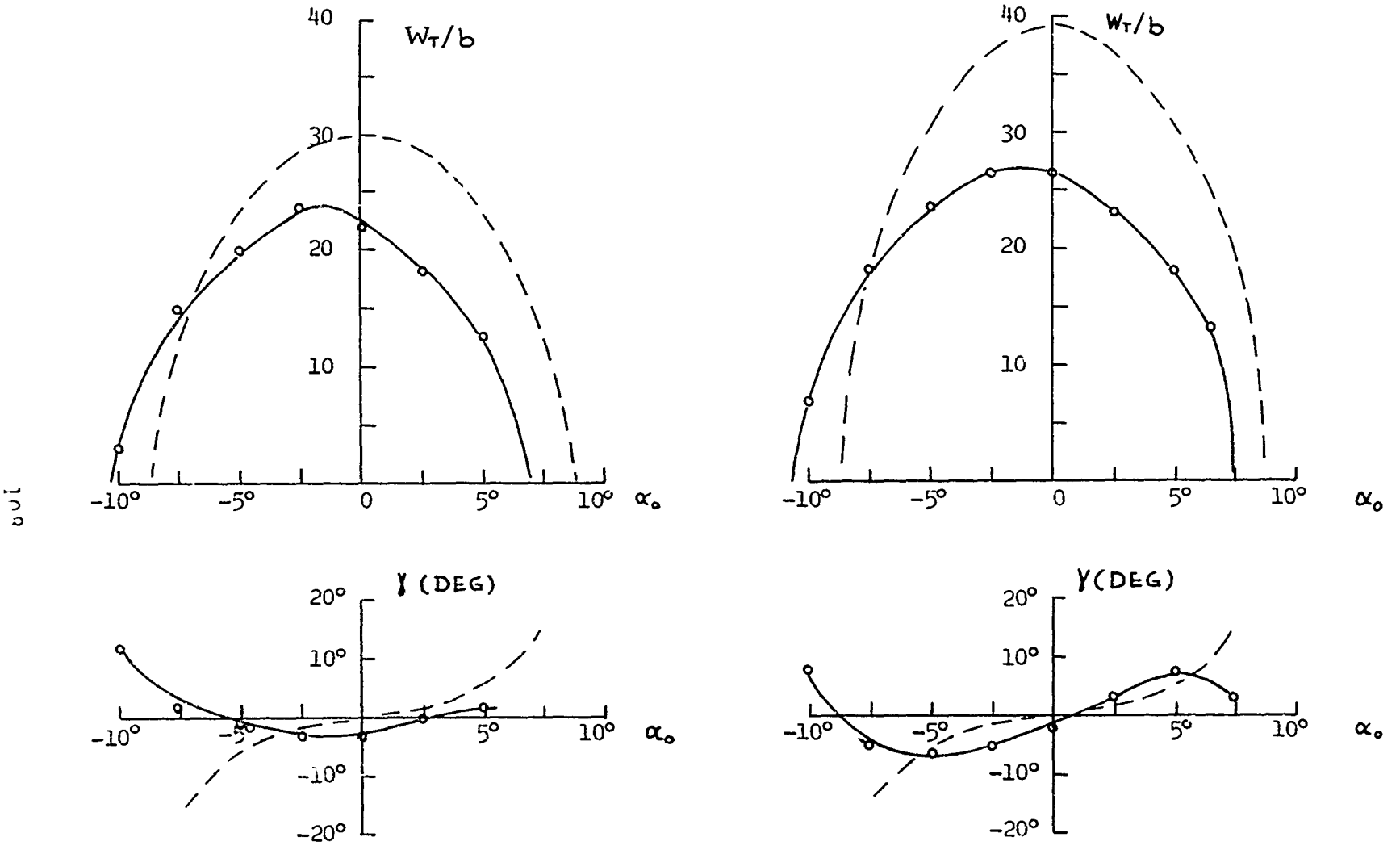

FIG. 12g,h STEADY STATE AMPLITUDE AND INCLINATION AT INITIAL ANGLE α_o (POSITION D)

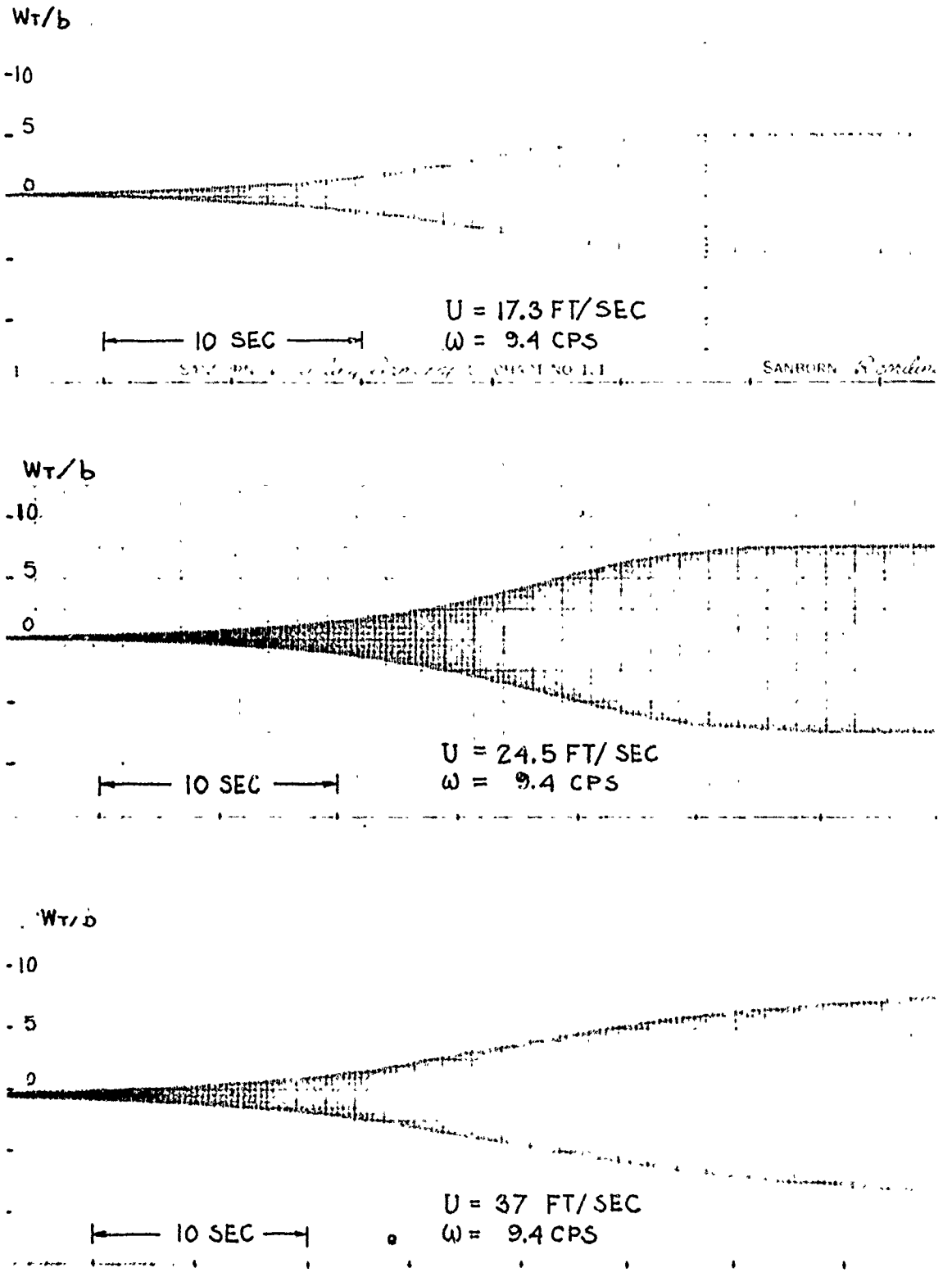

FIG. 13 SAMPLE TRANSIENT RECORDS (POSITION A, $\alpha_o = 0$)

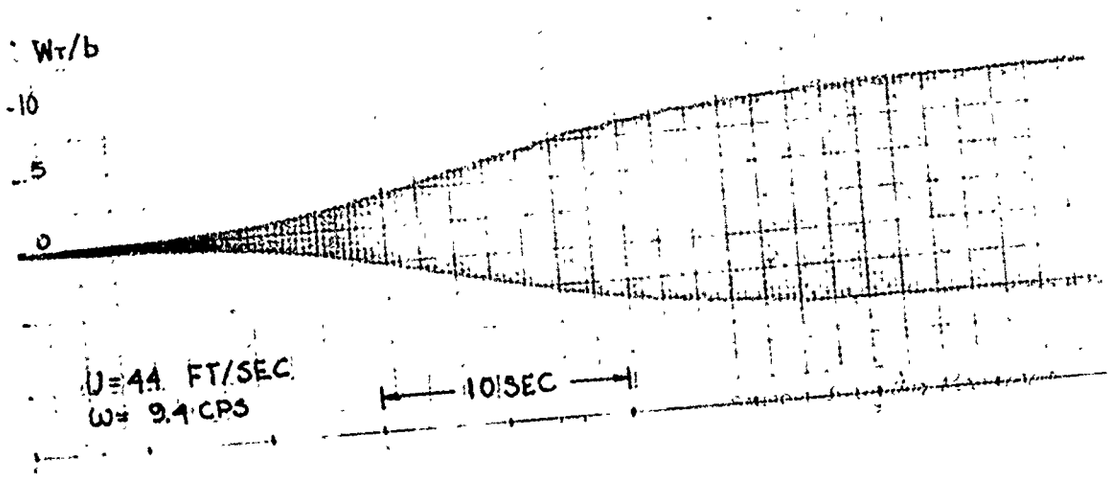

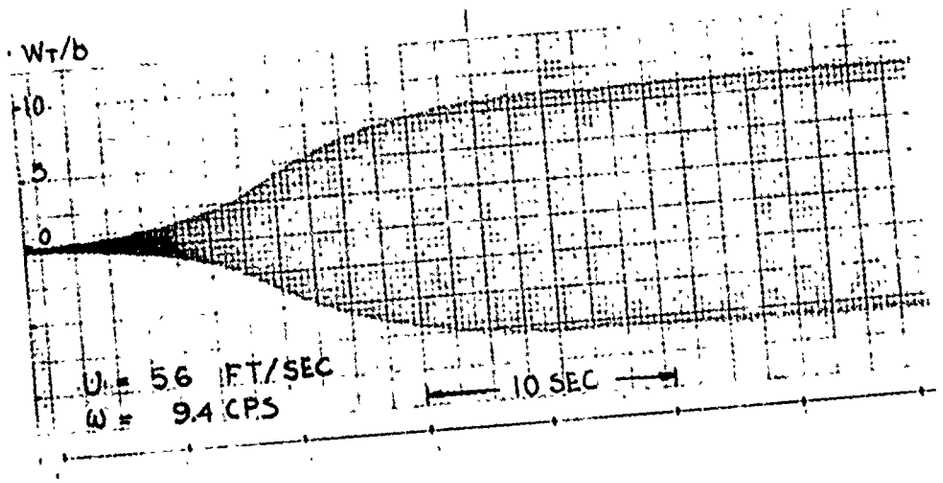

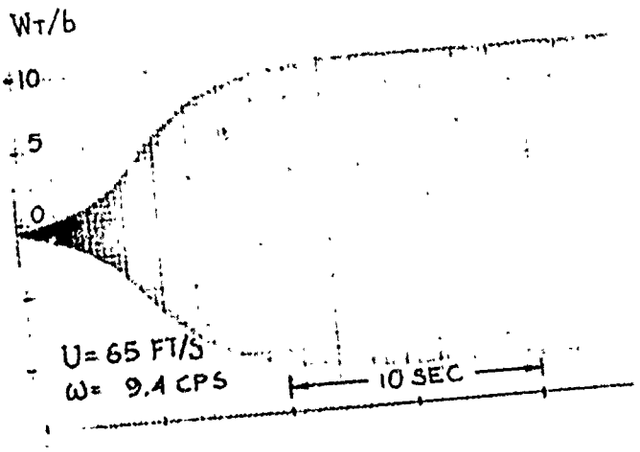

FIG. 13 (CONT'D) SAMPLE TRANSIENT RECORDS (POSITION A , $\alpha_o = 0$)

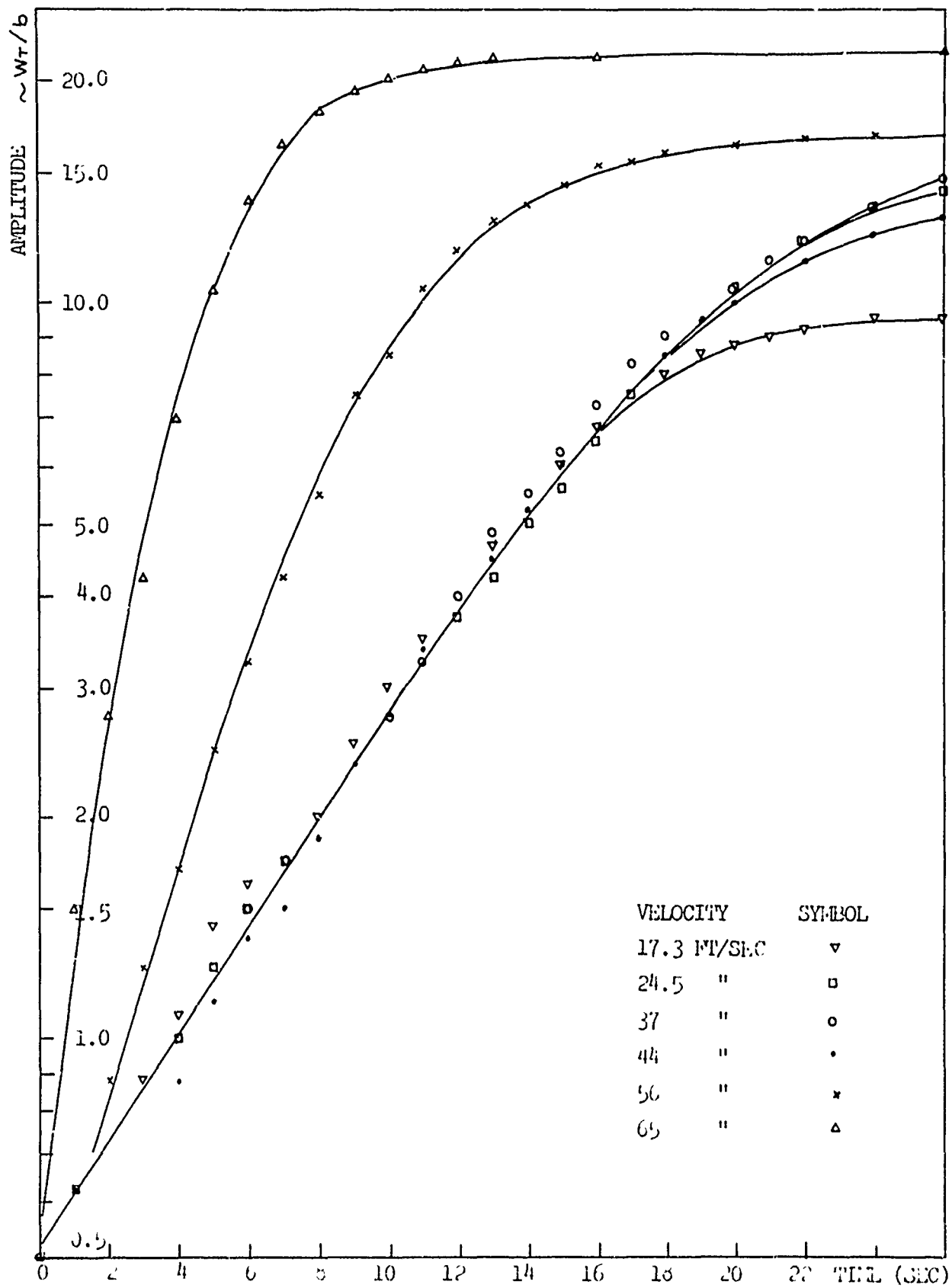

FIG. 14 TRANSIENT RESPONSE (POSITION A, α_o = 0)

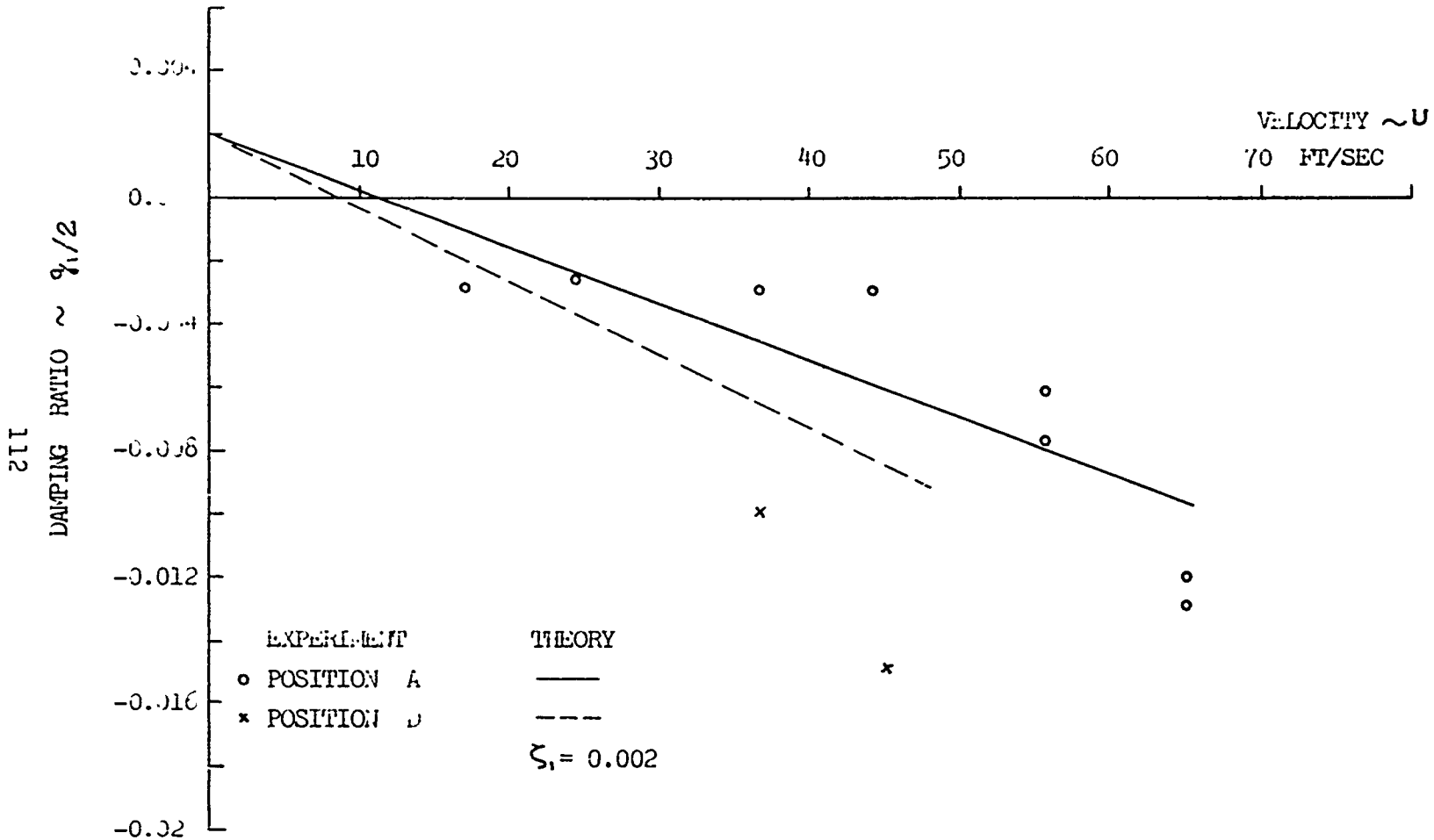

FIG. 15 LINEAR THEORY - EQUIVALENT - DAMPING RATIO ($\alpha_o = 0$)

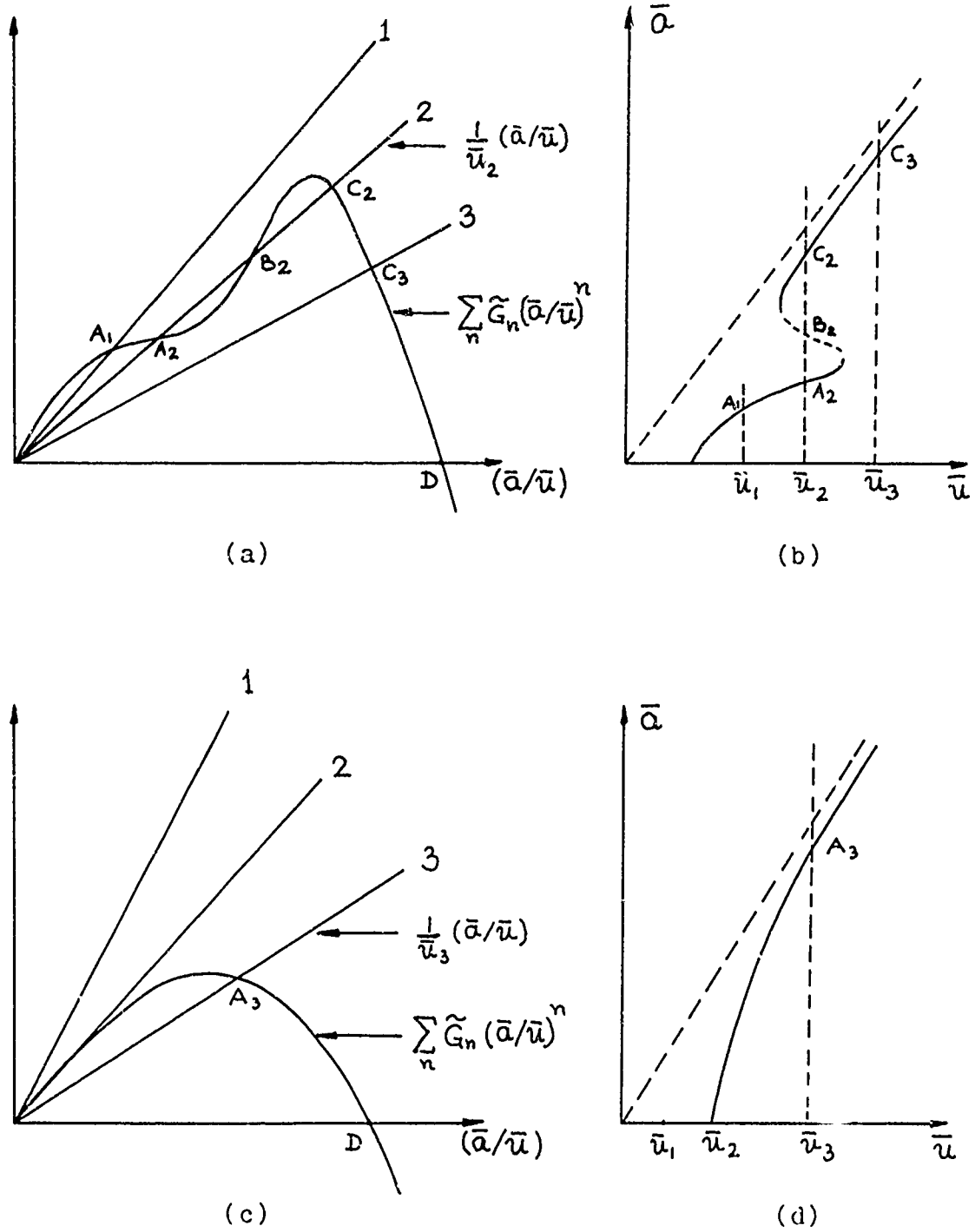

FIG. 16 GRAPHICAL REPRESENTATION OF STEADY STATE SOLUTION AND STABILITY FOR 1 D.O.F. MOTION

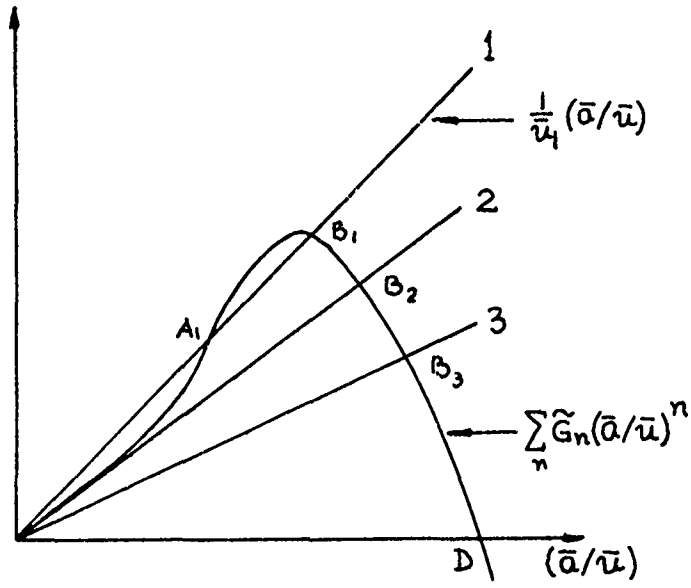

(e)

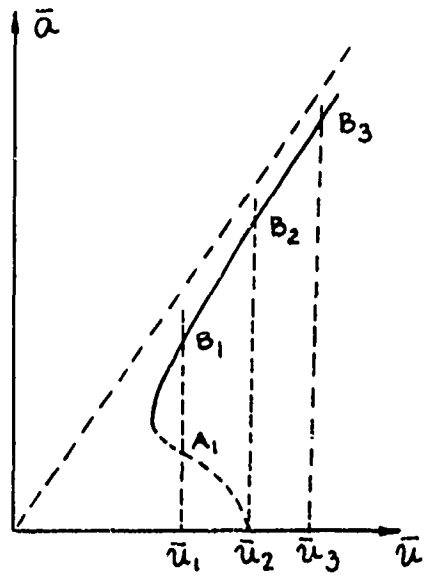

(f)

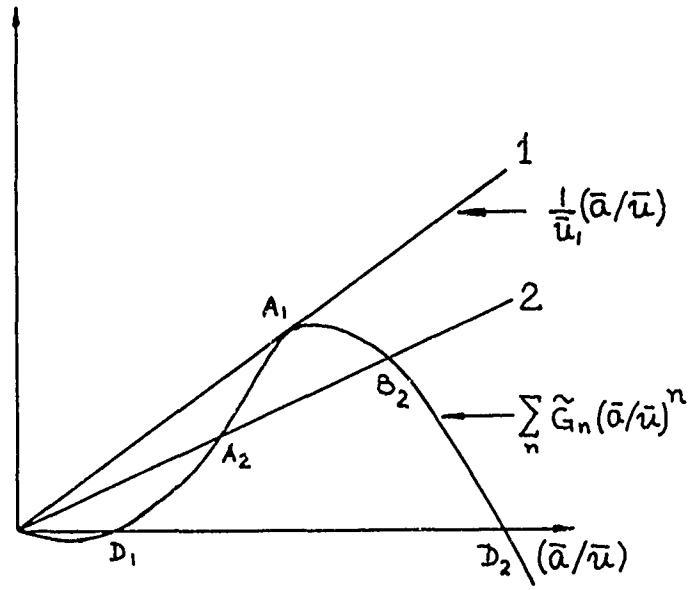

(g)

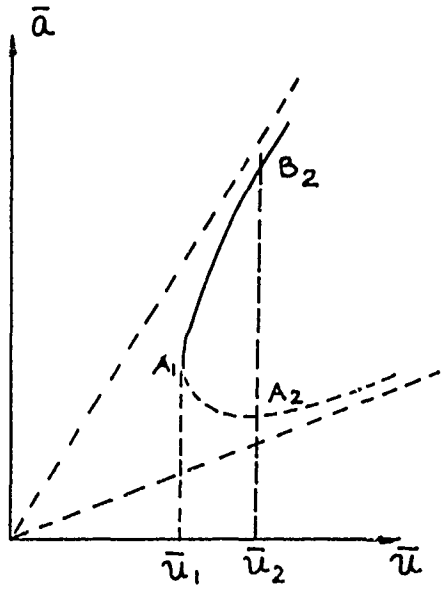

(h)

FIG. 16 (CONT'D) GRAPHICAL REPRESENTATION OF STEADY STATE SOLUTION AND STABILITY FOR 1 D.O.F. MOTION

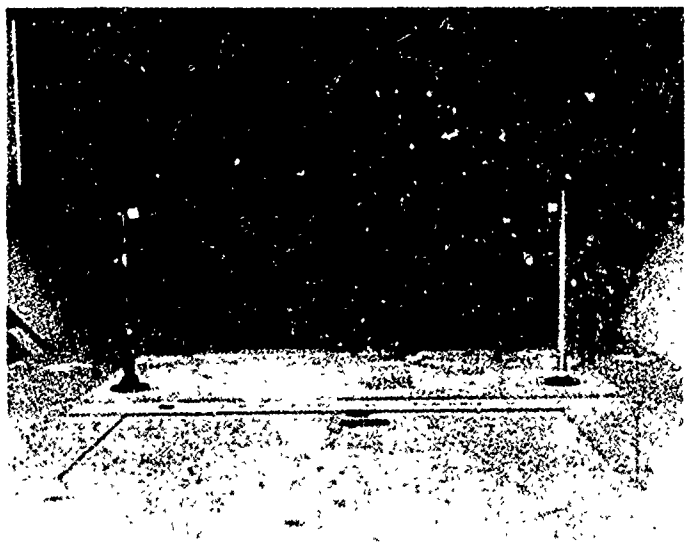

FIG. 17a SUSPENDED CABLE IN WIND TUNNEL
SPAN 3.02 FT d/ℓ = .059

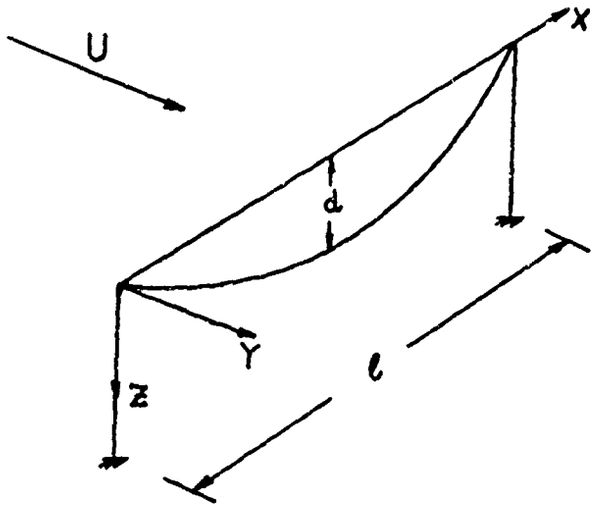

FIG. 17b SCHEMATIC DIAGRAM

SIDE VIEW

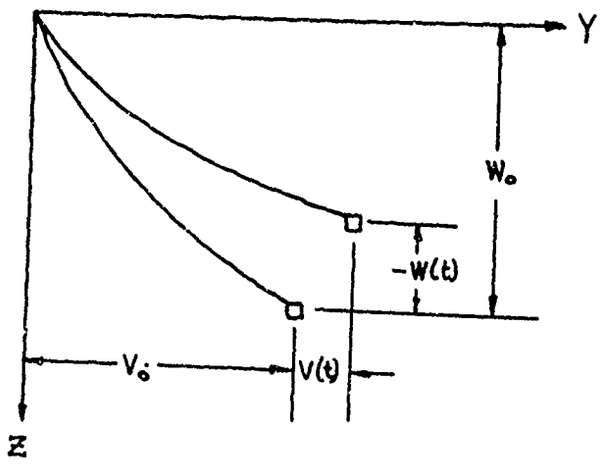

FIG. 17c COORDINATE SYSTEM

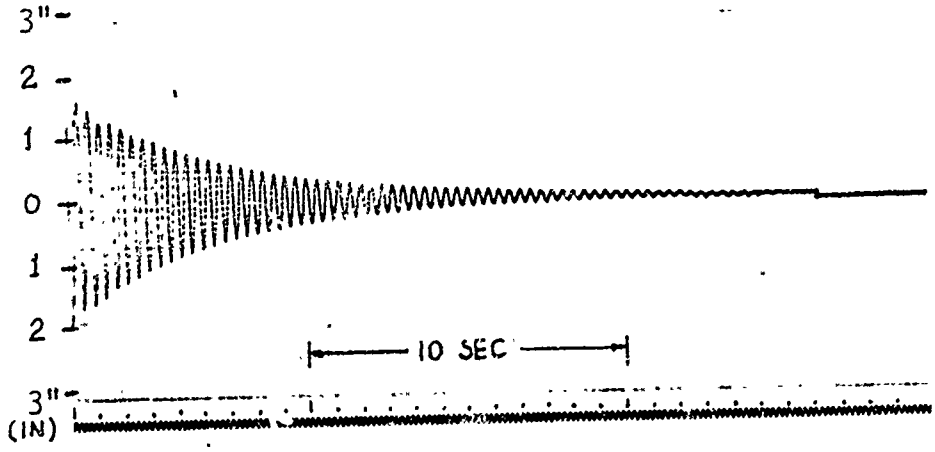

FIG. 18a TYPICAL DECAY RECORD FOR
$d/\ell = 0.055$

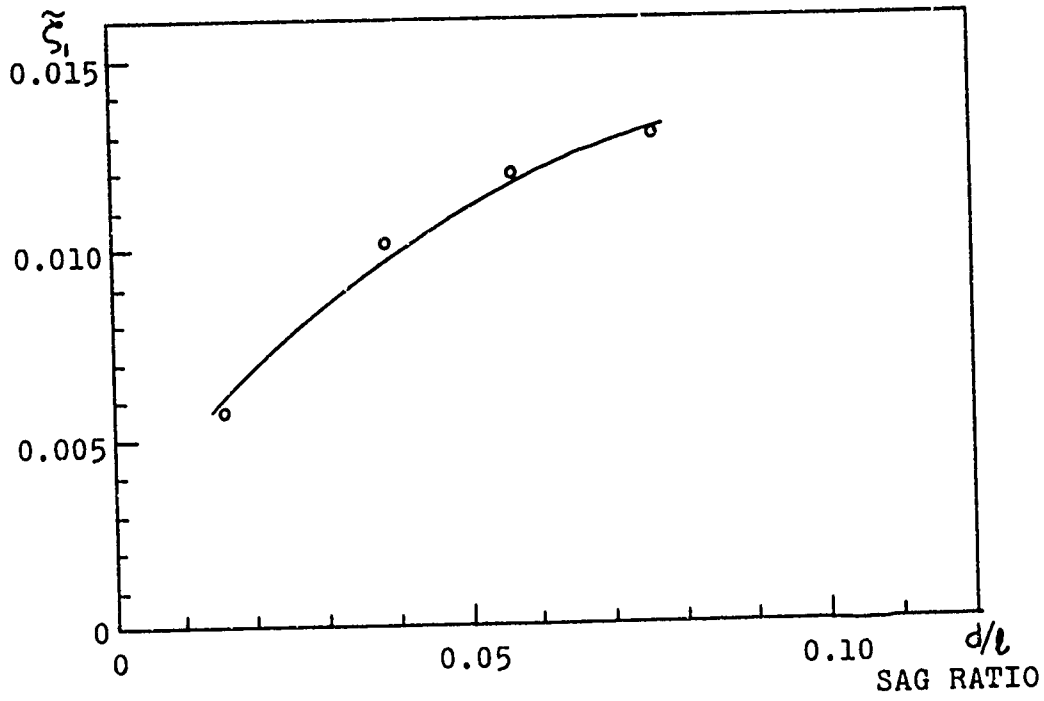

FIG. 18b FIRST MODE DAMPING RATIO FOR SMALL OSCILLATION FOR DIFFERENT SAG RATIOS

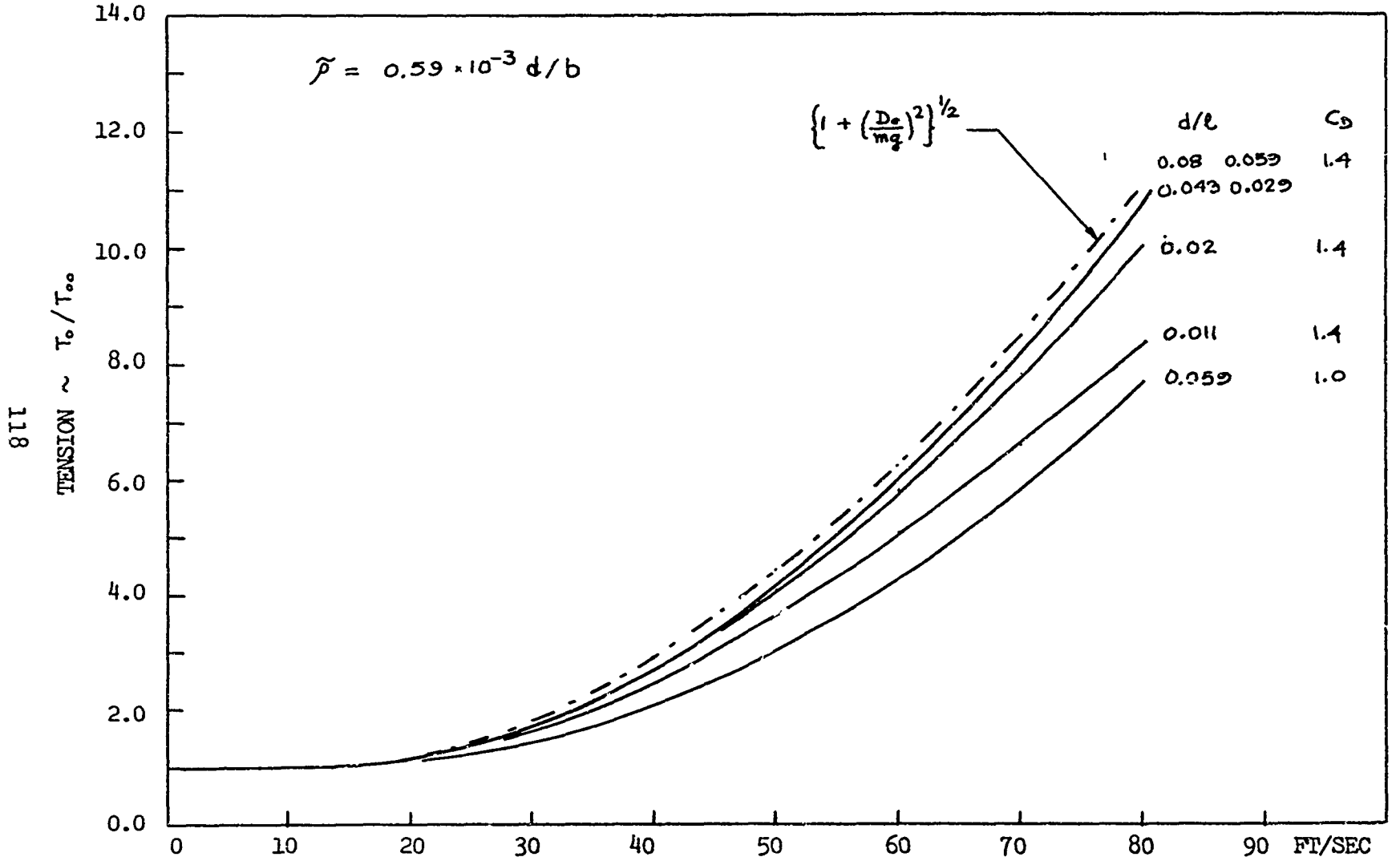

FIG. 19 CABLE TENSION VARIATION WITH WIND VELOCITY

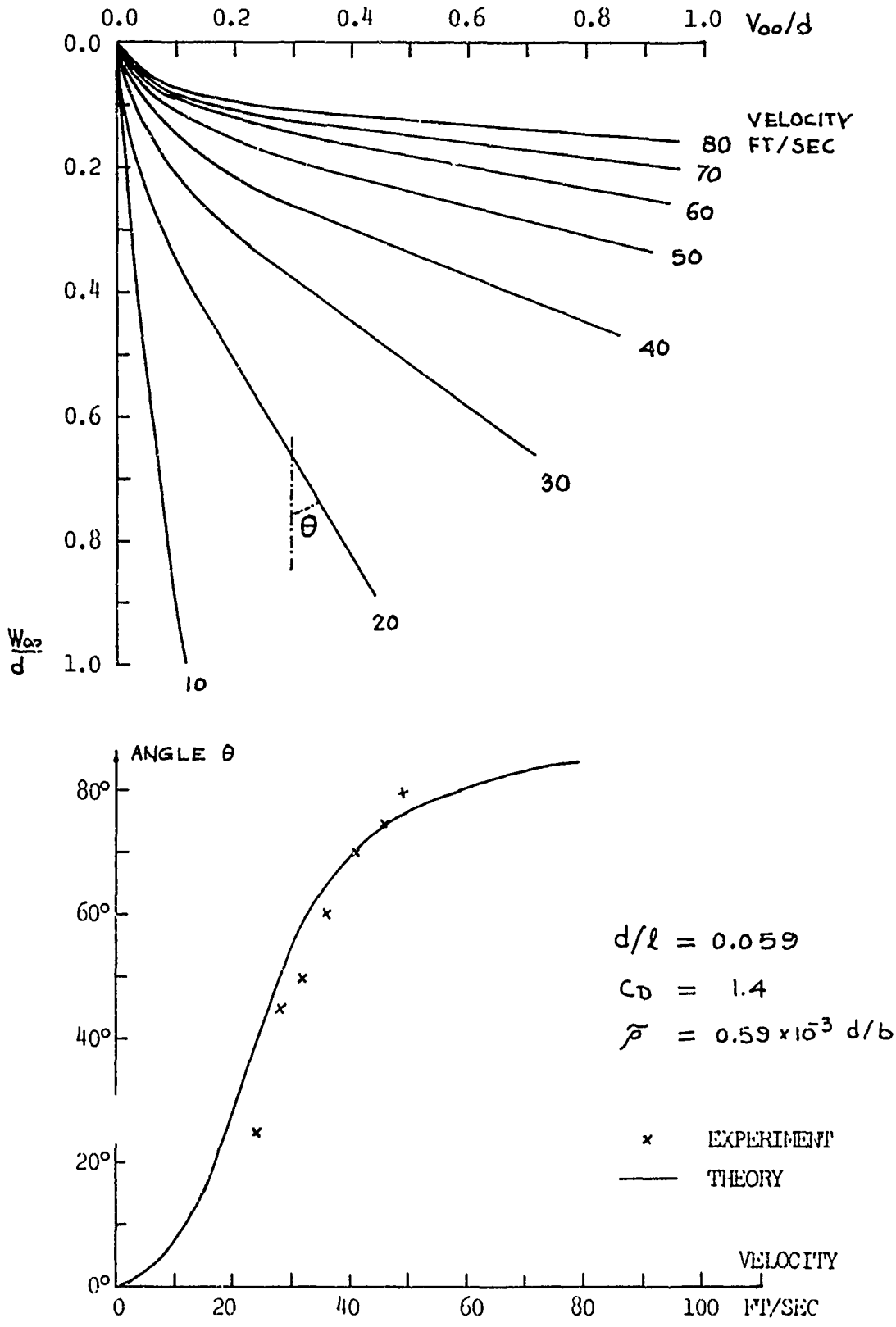

FIG. 20 STATIC POSITION VARIATION WITH WIND VELOCITY

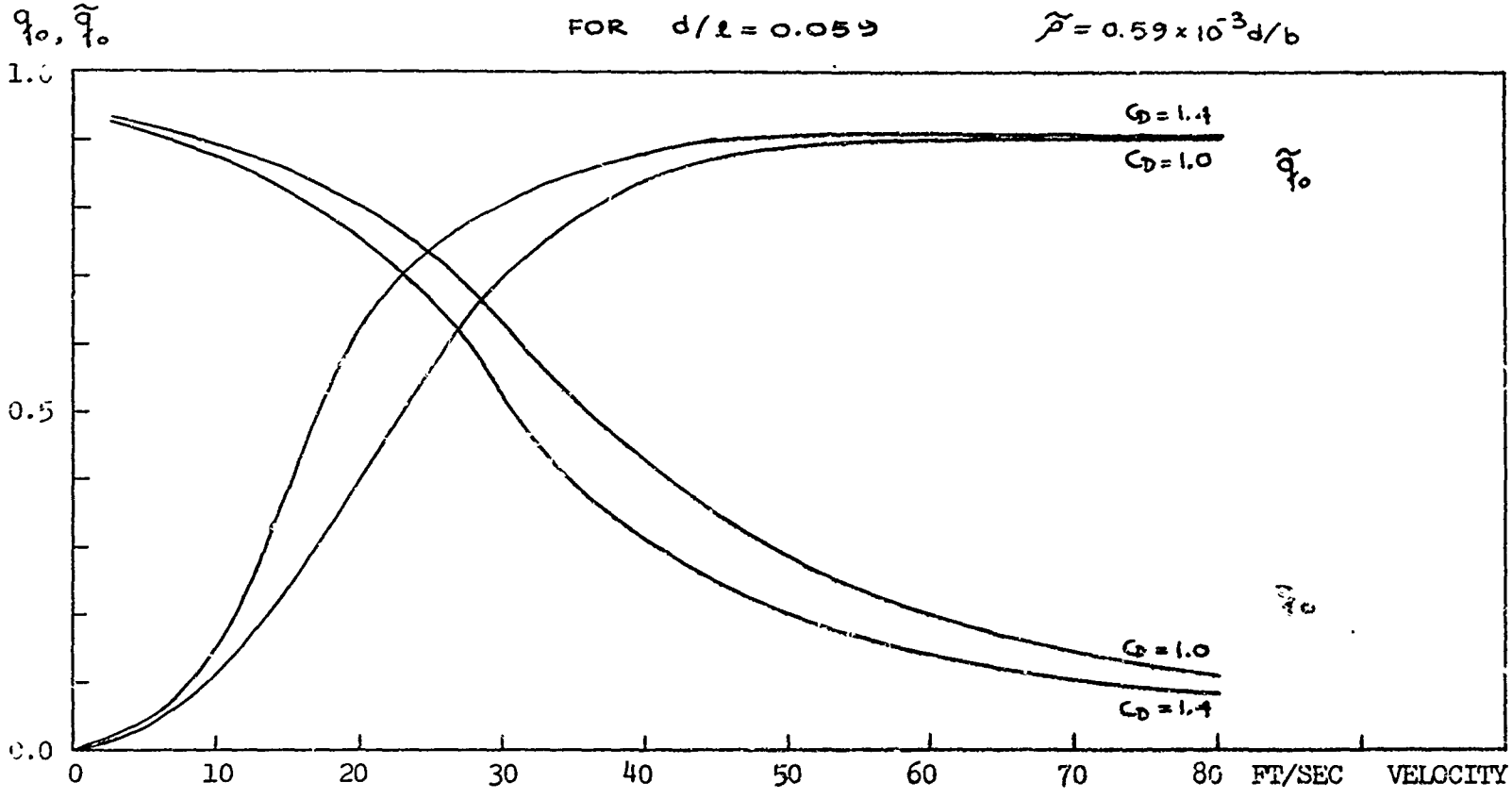

FIG. 21 q_{10} AND $\tilde{q}_{10}$ VARIATION WITH VELOCITY

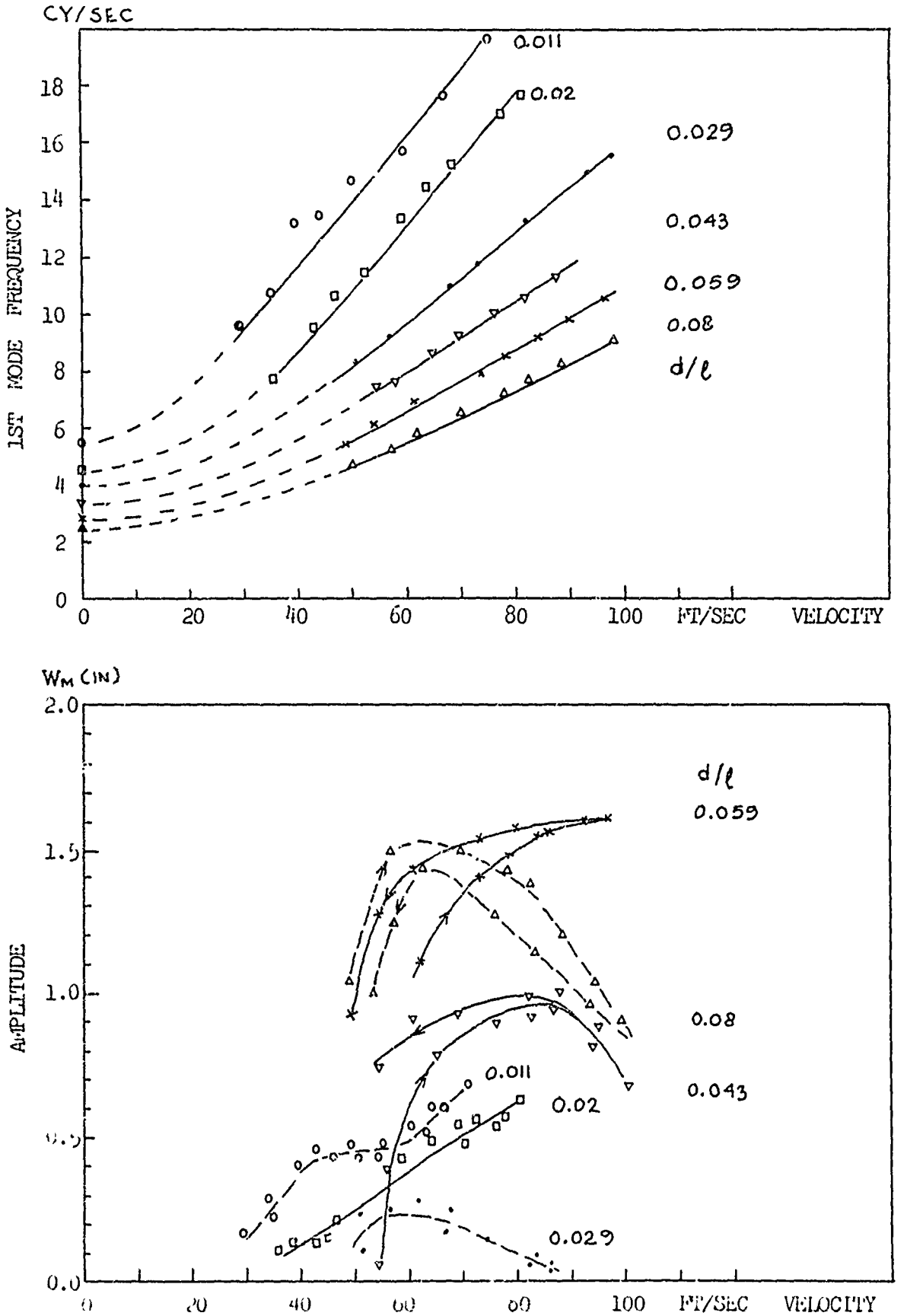

FIG. 22a STEADY STATE FREQUENCY AND AMPLITUDE RESPONSE

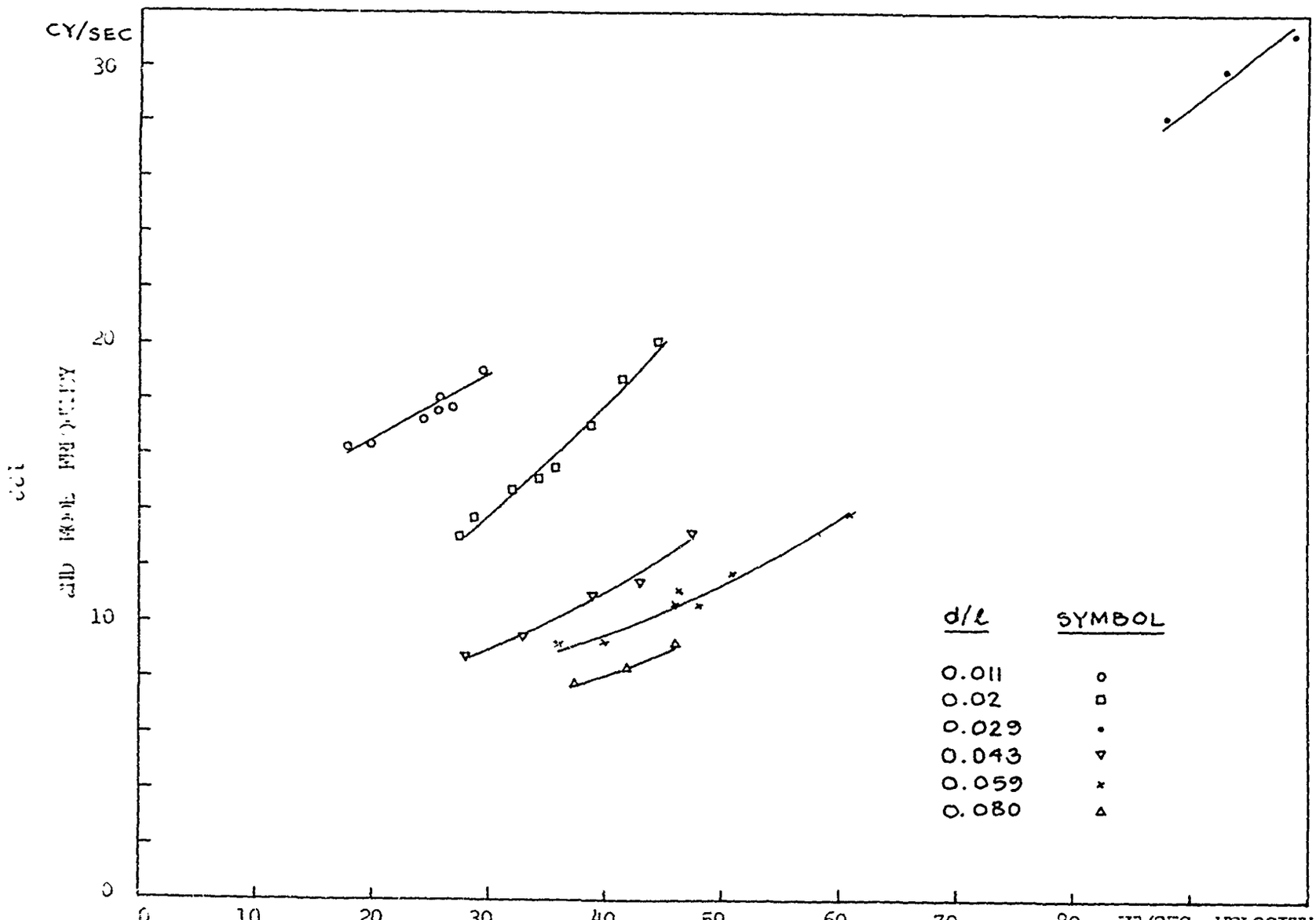

FIG. 22b THE SECOND MODE FREQUENCY RESPONSE

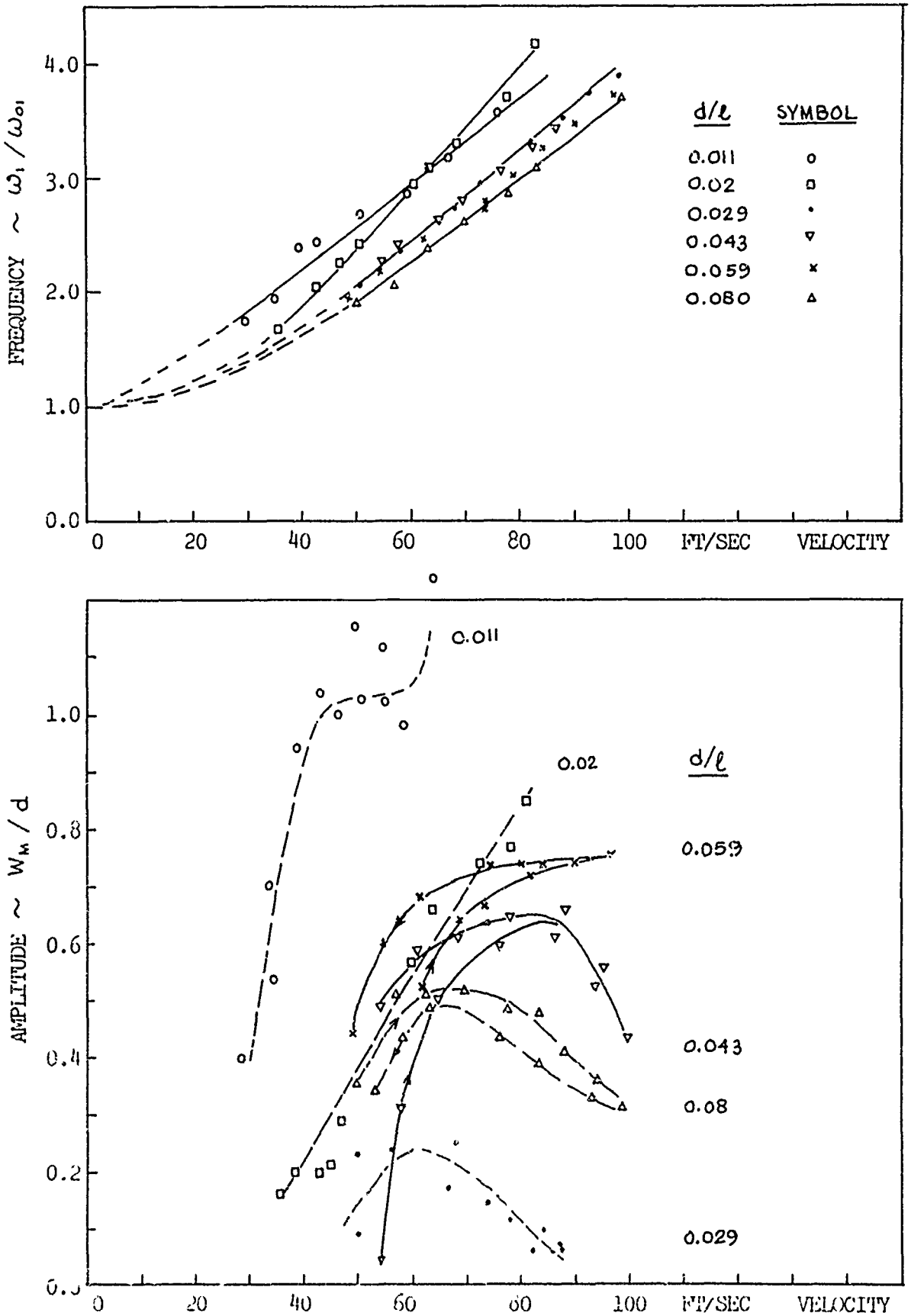

FIG. 23 STEADY STATE FREQUENCY AND AMPLITUDE RESPONSE

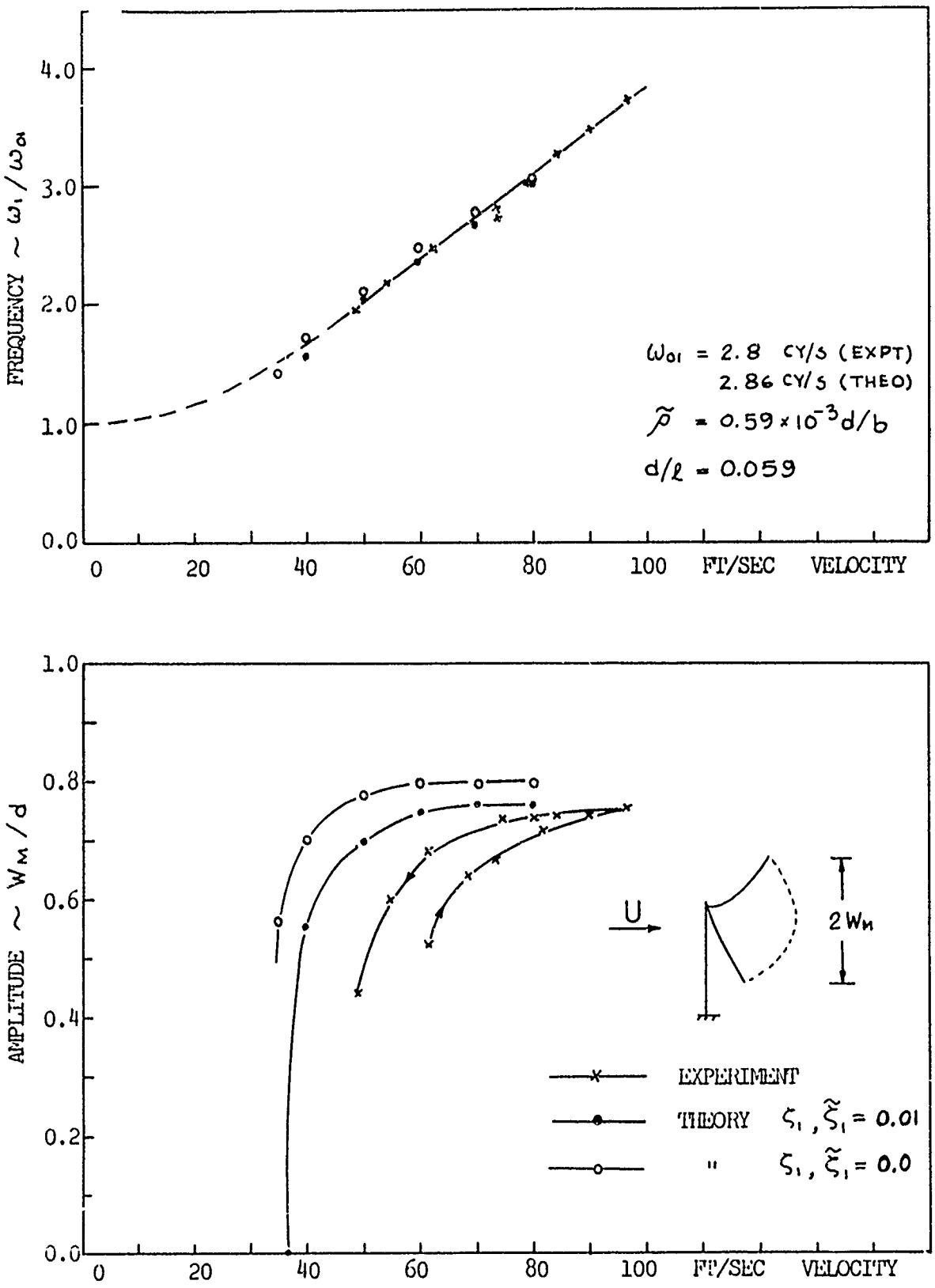

FIG. 24a STEADY STATE FREQUENCY AND AMPLITUDE RESPONSE
d/ℓ = 0.059

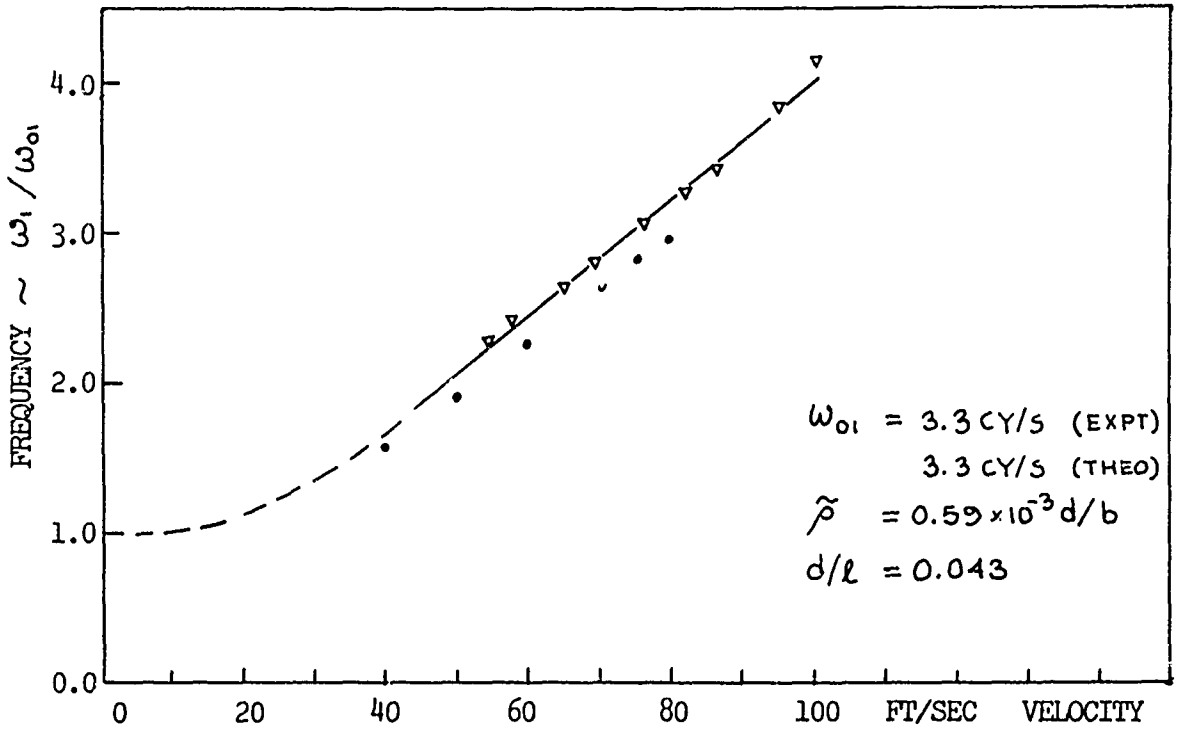

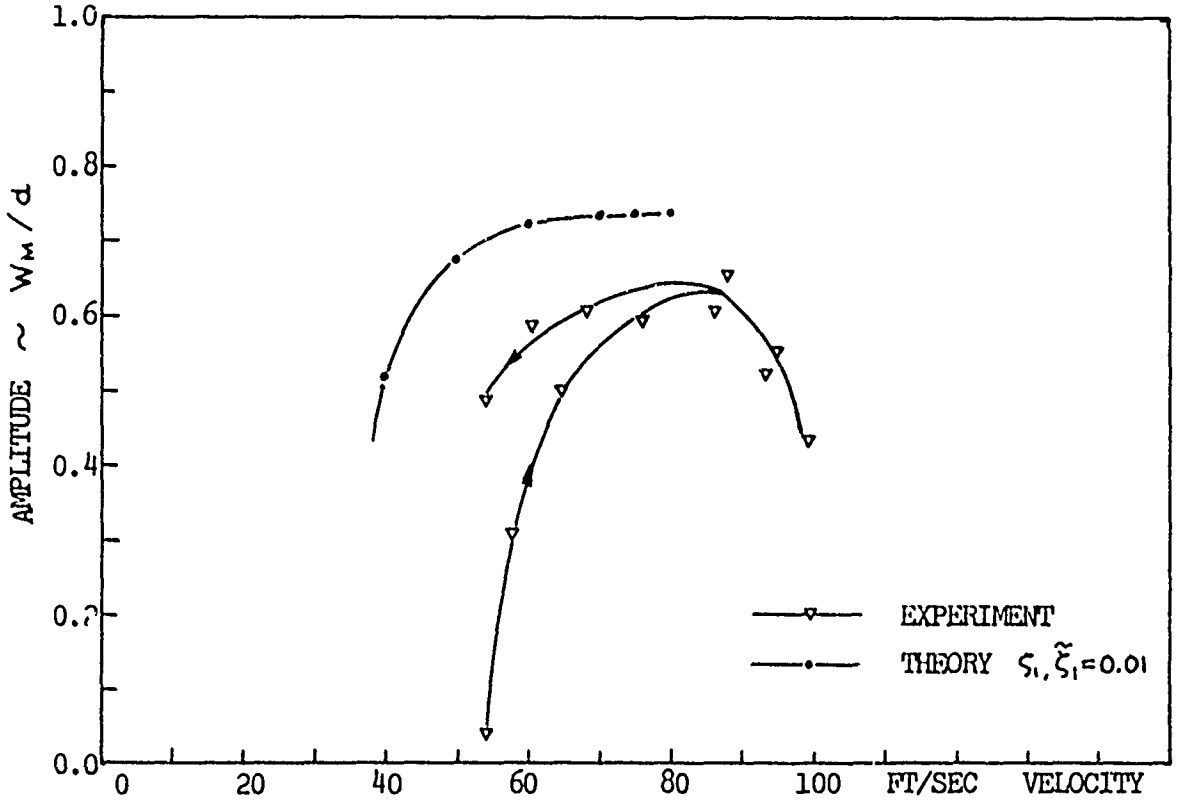

FIG. 24b STEADY STATE FREQUENCY AND AMPLITUDE RESPONSE
d/ℓ = 0.043

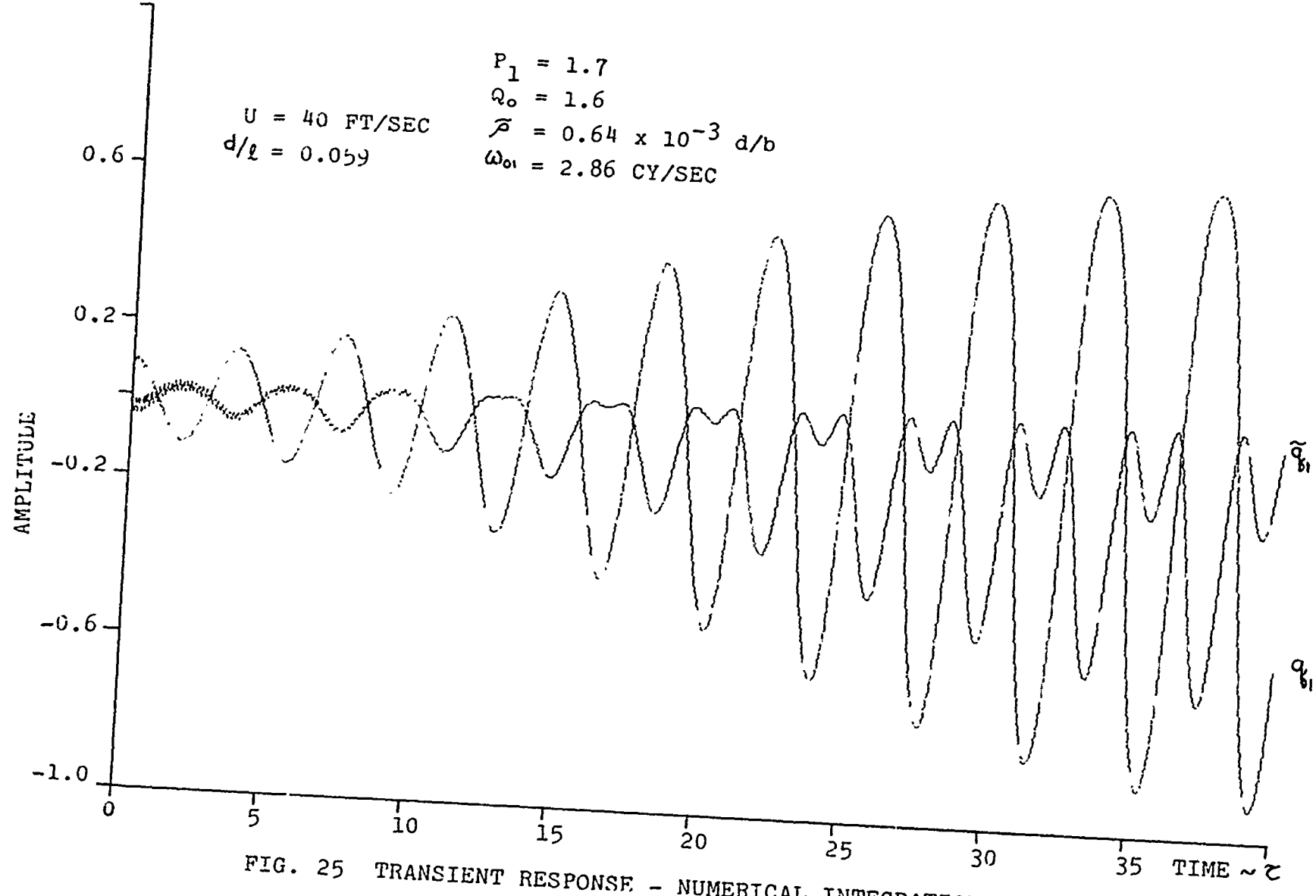

FIG. 25 TRANSIENT RESPONSE - NUMERICAL INTEGRATION

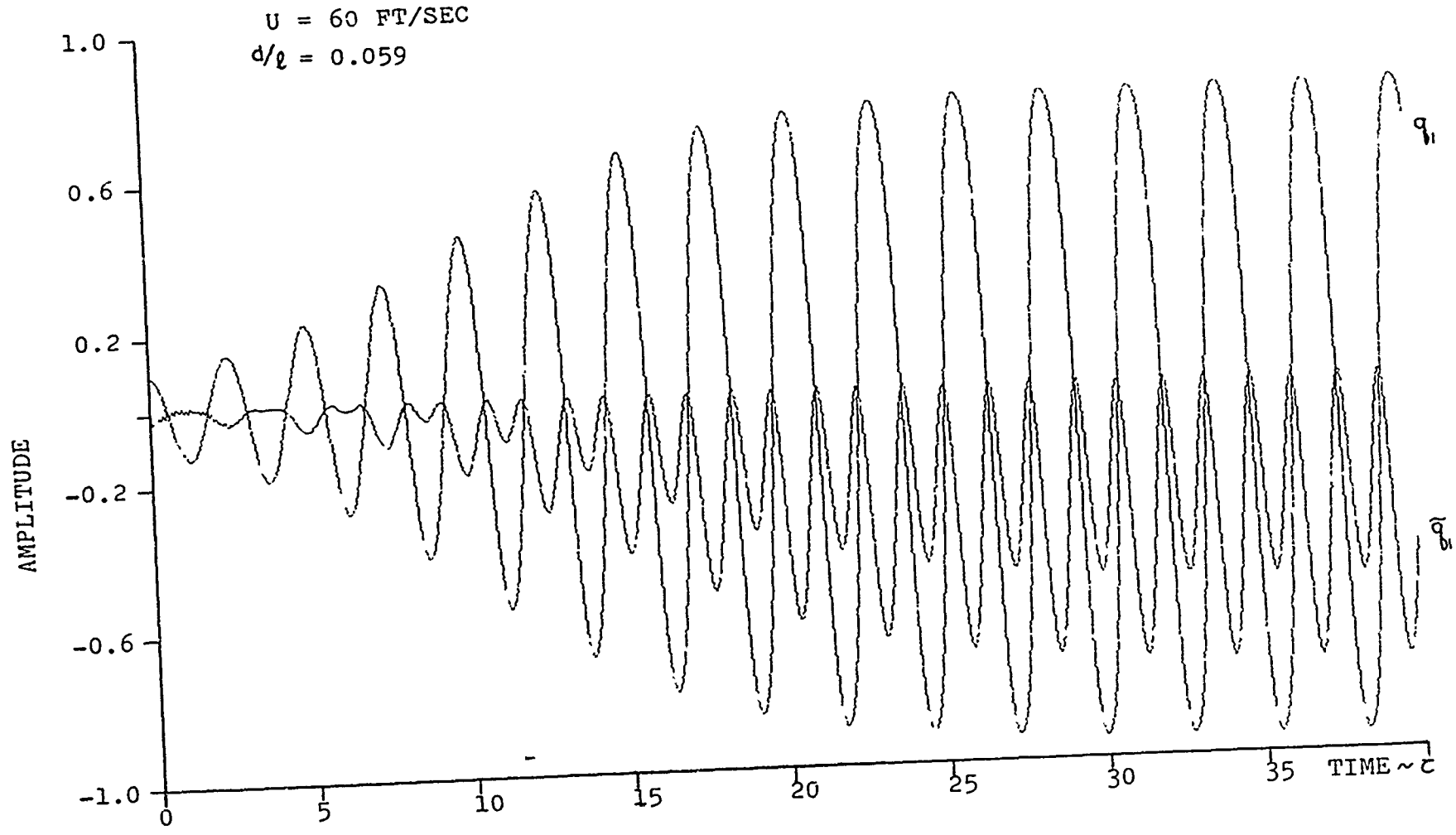

FIG. 25 (CONT'D) TRANSIENT RESPONSE - NUMERICAL INTEGRATION

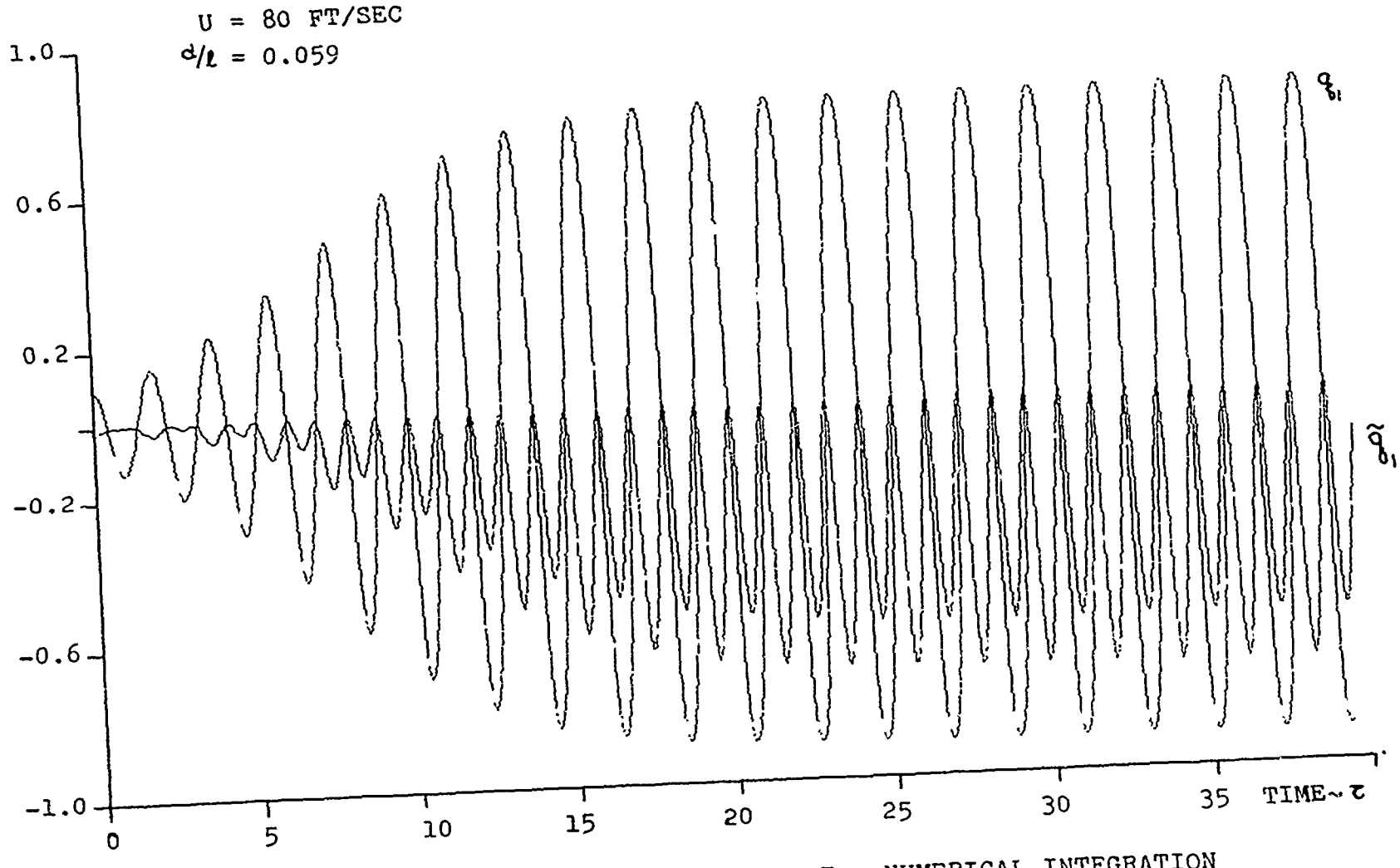

FIG. 25 (CONT'D) TRANSIENT RESPONSE - NUMERICAL INTEGRATION